Modelling and Quality Control Strategies for Batch Cooling Crystallizers

APPROVED BY
DISSERTATION COMMITTEE:

Supervisor: _____

_____

_____

_____

_____

This dissertation was prepared with the LaTeX document preparation system using additional macros written by John W. Eaton based on the thesis style written by Khe-Sing The for The University of Texas at Austin.

TeX is a trademark of the American Mathematical Society.

This dissertation was edited and composed on a SPARCstation 2 running the SunOS operating system.

SPARCstation 2 and SunOS are trademarks of Sun Microsystems, Inc.

Copyright © 1993 by Stephen Michael Miller.

All rights reserved. No part of this publication may be reproduced, stored in a retrieval system, or transmitted, in any form or by any means, electronic, mechanical, photocopying, recording or otherwise, without the prior written permission of the author.

Printed in the United States of America.

10 9 8 7 6 5 4 3 2 1

To Margaret for assuring me that I would finish, and to my parents

for *always* assuring me that such things are not conditions for their love.

Modelling and Quality Control Strategies for Batch Cooling Crystallizers

by

STEPHEN MICHAEL MILLER, B.S., M.S.

DISSERTATION
Presented to the Faculty of the Graduate School of
The University of Texas at Austin
in Partial Fulfillment
of the Requirements
for the Degree of

DOCTOR OF PHILOSOPHY

THE UNIVERSITY OF TEXAS AT AUSTIN
May 1993

Acknowledgments

The experience that I have had at the University of Texas has been one of considerable growth and learning, very little of which would have been possible without the technical and moral support provided by my committee, my advisor, my friends, and my family.

I would like to express my appreciation to Professors Thomas Edgar, David Himmelblau, William Koros and Raymond Davis for their feedback, guidance and gracious service on my dissertation committee.

Because of the limited experience and information to which an incoming graduate student has access, I have decided that there is an element of luck—either good or bad—in the advisor/student selection. I feel very fortunate about the outcome of this decision process for me. Graduate school represents a steep portion in my learning curve; the interaction that I have had with my advisor, Professor James Rawlings, has made the climb possible. He inspired me to attempt things that had previously intimidated me, he gave me room to think and grow, and he provided insightful guidance for my work and other facets of my life.

I am very grateful to the rest of Group-Rawlings: Walt Witkowski, Andy Fordyce, John Eaton, Scott Meadows, Tony Mullins, Ken Muske, Rock Matthews, John Campbell, and Missa Trueper. Technical collaboration with this group was very important to me. When learning to walk, crawling is comfortable, safe, and more efficient...but only at first. There have been many times that John Eaton encouraged me to give up my computer crawling for one of his consistently-helpful discoveries. From computing tips, to discussions of numerical algorithms and control schemes, to helping me take data, the technical support of the entire group was invaluable. Despite all of this, I am most thankful for the advice and irreplaceable heart-to-hearts with Walter, the weightlifting, the trips to The Crown, the Galveston Fluids Seminar Series...I am most thankful for the fellowship.

An acknowledgement of Group-Rawlings would not be complete without thanking Cheryl for her friendship and Melanie and Blake for many amusing moments.

From the beginning of my stay here, I was lucky enough to work with Glenn Wright, Cheng Ling, and Jim Bosley. I also, through a fortunate happen-

stance, met Ed Burger. I am very grateful for their help, support, and friendship throughout my graduate school experience.

There were many other graduate students from whom I gained a great deal. I would especially like to acknowledge Noel Bell, Ashu Patwardhan, Mike and Lou Ann Liebman, Jim Miller, Sulagna Chatterjee, Karen McBrayer, Kenny Teague, Scott Bushman, Tom Badgwell, Anthony Toprac, Dave Dixon, and Johann Le Roux for support that ranged from exposure to new research tools to memorable lunchroom conversation.

There are also many other friends whose love and support have meant a great deal. Mark and Kim Plemmons, Paige Cothran, Bipin Shah, Tom Marsh, Stattler Mood, Shari Holland, Bruce Dvořák, and Tish Critendon have been wonderful.

I feel quite fortunate that Margaret Callcott and I were able to share our graduate school experience. Through her very special love of people, of family, and of me, she has taught me much about life. While I still have some work to do, she has been a powerful force in my learning to make time for the things that are really important. I will always be thankful for the many gifts of her time and of herself.

My family has always been a source of support and happiness. The love and humor of my sister have provided buoyancy throughout my life. She has been typically important in this endeavor. Few people are so lucky as to ever have such a friend; fewer still have such a friend from day one. I should also note that the friendship with my brother-in-law would have been impossible without her.

My aunts and uncles have continually provided encouragement. The love and support of my grandmothers have been evident always; the nearly weekly calls and letters over the past six years have often gotten me back on track. My parents have moved me, visited me, flown me home, counseled me, soothed me, and have never missed an opportunity to express their unconditional love.

In *Cold Sassy Tree*, Rucker Blakeslee tells his grandson the following: "Livin' is like pourin' water out of a tumbler into a dang Coca-Cola bottle. If'n you skeered you cain't do it." I was lucky enough to have two grandfathers to steady my hand. Any accomplishment of my life requires their acknowledgement.

Stephen Michael Miller

The University of Texas at Austin
May 1993

Modelling and Quality Control Strategies for Batch Cooling Crystallizers

Publication No. _____

Stephen Michael Miller, Ph.D.
The University of Texas at Austin, 1993

Supervisor: James B. Rawlings

Common quality requirements for crystallization products (e.g., ability to flow, dissolution rate, and aesthetic appeal) depend on the crystal size distribution (CSD). In some cases, such as for products to be used in photographic materials, size uniformity is so critical that the CSD is the primary consideration of a customer. In addition to customer requirements, a concern of the manufacturer is the CSD-influenced efficiency of downstream processes such as thickening and filtration. Whether the output of a crystallizer is the final product, the quality of which will be scrutinized by the consumer, or an intermediate product in a large process, there is economic incentive for reproducible control of the CSD.

This study focuses on the CSD control of seeded, batch cooling crystallizers. An open-loop, model-based control strategy that handles input, output, and final-time constraints has been developed and experimentally tested with a KNO_3–H_2O system in a fully-instrumented, bench-scale crystallizer. Compared to natural cooling, increases in the weight mean size of up to 48% were achieved through implementation of optimal cooling policies on the KNO_3–H_2O system.

The control scheme is applicable to crystallization with size-dependent growth rate, growth dispersion, and fines dissolution. It also permits flexibility in objective function formulation, allowing consideration of objective functions that take into account solid-liquid separation in subsequent processing steps.

Model identification plays an important role in a model-based control algorithm and is an integral part of this research. Uncertainty bounds on model parameter estimates are not reported in most crystallization model identification studies. This obscures the fact that the resulting models are often based on experiments that do not provide sufficient information and are therefore unreliable. This study provides a method for assessing parameter uncertainty

and demonstrates the use of this assessment in experimental design. It is shown that measurements of solute concentration in the continuous phase and the transmittance of light through a slurry sample allow reliable parameter estimation. It is also shown that uncertainty in the parameter estimates is decreased by data from experiments that achieve a wide range of supersaturation. The model identification and control problems are connected through the issue of the sensitivity of the determined control policy to parameter uncertainty. A method to assess this sensitivity is presented.

For the KNO_3–H_2O system, it is shown that little benefit over that obtained from the open-loop optimal policy should be expected from using feedback in the control scheme. Nevertheless, a discussion is given of the potential need for feedback compensation in some systems, and suggestions are given for methods to incorporate feedback.

Table of Contents

Acknowledgments . . . . . **vii**

Abstract . . . . . **ix**

Table of Contents . . . . . **xi**

List of Tables . . . . . **xv**

List of Figures . . . . . **xvii**

Nomenclature . . . . . **xxi**

1. Introduction **1**

1.1 Project Motivation and Research Goals 1

1.2 Dissertation Overview 3

2. Experimental Apparatus and Measurement Techniques . . . **5**

2.1 Crystallizer 6

2.2 Operator Station 8

2.2.1 Data Acquisition and Communication with VAXStation 8

2.2.2 Signal Conditioning System 9

2.3 System for Manipulation of Crystallizer Temperature 9

2.4 Measurement Devices and Techniques for Crystallization Processes 11

2.4.1 Temperature Measurements 11

2.4.2 Concentration Measurement 11

2.4.3 Dynamic Crystal Size Distribution Measurement 13

2.4.4 Particle Sizing Using Light Scattering Theory 14

2.4.5 Malvern Particle Sizer 3600Ec 19

2.4.6 Transmittance Measurement 22

2.5 Product Sieve Analysis 27

2.6 Crystallizer Operation 29
2.7 Summary 30

3. Model Formulation and Solution 31
3.1 Model Development 31
3.1.1 Population Balance 31
3.1.2 Mass and Energy Balances 34
3.1.3 Constitutive Relations 35
3.1.4 Model Parameters 41
3.1.5 Model for Batch Cooling Crystallizer 41
3.2 Model Solution 42
3.2.1 Orthogonal Collocation 43
3.2.2 Method of Moments 49

4. Parameter Estimation and Model Validation 55
4.1 Parameter Estimation Methods 57
4.1.1 Parameter Estimation Posed as an Optimization Problem 59
4.2 Interpretation of Estimates 63
4.3 Experimental Design 65
4.3.1 Measured Variables 66
4.3.2 Operating Variables 69
4.3.3 Experimental Design Summary 73
4.4 Further Model Validation 77

5. Batch Crystallizer Control 81
5.1 Review of Previous Open-loop Optimal Control Studies 81
5.2 Statement of Control Problem as an NLP Problem 83
5.2.1 Final-Time Constraints 84
5.2.2 Input Constraints 84
5.2.3 State Constraints 85
5.3 Open-loop Optimal Control Examples 85
5.3.1 Maximizing Terminal Seed Size 85

5.3.2 Minimizing Nucleated Crystal Mass 86
5.4 Assessment of Effectiveness of Method 92
5.5 Sensitivity of Optimal Profile to Model Parameters 93
5.6 Experimental Implementation of Open-loop Control 97
5.7 Suggestions for Incorporating Feedback 104

6. Conclusions and Future Work 109

A. Model-Predictive Control of Crystallizer Temperature . . . 115

B. Mass and Energy Balances, and Population Balance Simplification 121
B.1 Mass Balance 121
B.2 Energy Balance 122
B.3 Simplification of Population Balance 124

C. Physical Properties for Potassium Nitrate–Water System . 125

Bibliography 127

Vita 143

List of Tables

3.1 Kinetic parameters for model. 47

4.1 Parameter estimates resulting from concentration measurements. 67

4.2 Parameter estimates resulting from concentration and transmittance measurements. 68

4.3 Parameter estimates resulting from concentration and transmittance measurements from two batch runs. 71

4.4 Comparison of linear statistics with Monte Carlo analysis of 500 replicate data sets. 75

4.5 Parameter estimates resulting from replicate runs of those used to obtain Table 4.3. 76

4.6 Parameter estimates resulting from concentration and transmittance measurements from four batch runs. Estimates taken as nominal parameters of KNO_3—H_2O system. 77

5.1 Summary of predicted effect of maximizing final seed size. . . . 86

5.2 Summary of predicted effects of minimizing $m_n(t_f)/m_s(t_f)$. . . 92

5.3 Summary of predicted effects of minimizing $m_n(t_f)/m_s(t_f)$ for hypothetical chemical system. 93

5.4 Effects of temperature profiles on weight mean size of crystallizer product. 103

5.5 Weight mean size and coefficient of variation of crystallizer product of several runs. 103

6.1 Results of parameter estimation based on concentration measurements. 110

6.2 Summary of parameter estimates and confidence intervals for KNO_3—H_2O system. Estimation based on concentration and transmittance measurements from experiments with various temperature profiles. 111

List of Figures

2.1 Schematic of the batch crystallization system. 6

2.2 Crystallization Vessel. 7

2.3 Cascade configuration for control of crystallizer temperature. . 11

2.4 Schematic of a particle sizer based on light scattering. 15

2.5 Depiction of array of photodiode detectors. 16

2.6 Recovery of the CSD from noise-free, simulated light scattering data using simple least squares. 19

2.7 Recovery of the CSD from light scattering data with 5% noise using penalized and constrained least squares with $\gamma = 10^{-4}$. . 20

2.8 Malvern results for monodispersion of cylinders with 45 μm diameter and 195 μm length. 21

2.9 Comparison between measured transmittance and that predicted by the Beer-Lambert law for low concentrations of 275-μm NaCl crystals. 25

2.10 Comparison between measured transmittance and that predicted by the Beer-Lambert law for NaCl crystals of size 275 μm. . . . 26

2.11 Comparison between measured transmittance and that predicted by the Beer-Lambert law for NaCl crystals of sizes 165 and 463 μm. 27

3.1 Crystal incorporation sites. Flat faces (A), step sites (B), and kink sites (C). 37

3.2 Nucleation Mechanisms 39

3.3 Depiction of the two subpopulations of the CSD—the nucleated crystals and the seed crystals. 44

3.4 Evolution of CSD for case with size-independent growth rate. . 48

3.5 Concentration and transmittance for case with size-independent growth rate. 48

3.6 Evolution of CSD for case with size-dependent growth rate (above), and corresponding seed distributions at t_0 and at t_f (below). 50

3.7 Concentration and transmittance for case with size-dependent growth rate. 51
3.8 Time profiles of first four moments of the crystal size distribution (converted to a per-mass-solvent basis). 52
3.9 Concentration and transmittance from the method of moments. 53

4.1 Abstraction of relationship between parameters and measurements. 55
4.2 Confidence region demonstrating significant correlation between parameters. Conservative confidence interval for θ_i is defined by $\delta\theta_i$. 65
4.3 Temperature profile for batch crystallization of KNO_3 from water. 67
4.4 Concentration measurements from experiment with temperature profile given in Figure 4.3. 68
4.5 Transmittance measurements from experiment with temperature profile given in Figure 4.3. 69
4.6 Fit to the data of the model with nominal parameters given in Table 4.1. 70
4.7 Transmittance data and prediction from model with nominal parameters given in Table 4.1. 71
4.8 Gradual-cooling temperature profile for batch crystallization of KNO_3 from water. 72
4.9 Fit to concentration data from two runs of model with nominal parameters given in Table 4.3. 73
4.10 Fit to transmittance data from two runs of model with nominal parameters given in Table 4.3. 74
4.11 Residuals between concentration data and model predictions for one of the runs illustrated in Figure 4.9. 75
4.12 Residuals between transmittance data and model predictions for one of the runs illustrated in Figure 4.10. 76
4.13 Comparison of sieve analysis results and the model prediction for a crystallizer product. 78
4.14 Sieve analysis results for two replicate experiments. 79

5.1 Temperature and supersaturation profiles for batch crystallizer. Cooling policies illustrated include natural cooling, constant-rate or linear cooling, and cooling controlled to maximize final-time seed size. 87

5.2 Temperature and supersaturation profiles for batch crystallizer. Cooling policies illustrated include natural cooling, constant-rate or linear cooling, and cooling controlled to minimize final-time value of m_n/m_s. 89

5.3 Demonstration of addition of cooling rate constraint of 0.1°C/min. Profiles are those for minimization of the final-time value of m_n/m_s. 90

5.4 Implementation of a constraint on the maximum allowable value of $\hat{C} - \hat{C}_{\text{sat}}$. Profiles are those for minimization of the final-time value of m_n/m_s. 91

5.5 Sensitivity of control profile to parameter uncertainty. Optimal control policy for nominal parameters and for parameter sets perturbed by $\pm 0.1(\boldsymbol{\delta\theta}_{\text{worst}})$. 96

5.6 Sensitivity of control profile to parameter uncertainty. Optimal control policy for nominal parameters and for parameter sets perturbed by $\pm 0.36(\boldsymbol{\delta\theta}_{\text{worst}})$. 97

5.7 Experimental temperature data for natural, linear, and optimal cooling. Set-point trajectory tracking is also shown. 98

5.8 Concentration and transmittance measurements and model predictions for natural cooling operation. 100

5.9 Concentration and transmittance measurements and model predictions for linear cooling operation. 101

5.10 Concentration and transmittance measurements and model predictions for optimal cooling policy implementation. 102

5.11 Experimental relative supersaturation data for natural, linear, and optimal cooling. 104

5.12 Optimal temperature profiles for high and low seeding. 105

5.13 Concentration and transmittance measurements and model predictions for optimal cooling policy implementation with high seed loading. 106

A.1 Response of system to a unit step change in the input variable at the k^{th} sampling instant. 116

A.2 Estimation of disturbance, d. k represents the present time. y_{meas} = measured value. 118

A.3 Response of crystallizer temperature to a -2° C step in the jacket temperature. The fit of a first order model with deadtime is also shown. 119

A.4 Performance of the cascade control system with QDMC primary controller and PID secondary controller. The crystallizer jacket temperature (output of QDMC controller) is also shown; $u_{\min} = 24.5°$, $u_{\max} = 30.5°$ 120

Nomenclature

Some of the following symbols are used for a number of different purposes in the text. The local meaning should be clear from the context.

lower case symbols

$\mathbf{b}_l$ — vector of lower bounds of linear constraints of NLP problem
$\mathbf{b}_u$ — vector of upper bounds of linear constraints of NLP problem
c_p — heat capacity
$c.v.$ — coefficient of variation of weight–size distribution
e_{ij} — difference between measurement and prediction, $y_{ij} - \tilde{y}_{ij}$
$e_t(s_i)$ — energy of scattered light measured by detector of inner radius s_i
f — crystal distribution function
f_{N} — nucleated crystal subpopulation CSD
f_{S} — seed crystal subpopulation CSD
g — crystal growth rate order
$\mathbf{g}$ — vector of inequality constraints
h — conversion factor, volume of slurry per mass of solvent
$\mathbf{h}$ — vector of equality constraints
j — slurry density power law coefficient for nucleation rate expression
k_a — crystal surface area shape factor
k_b — nucleation rate coefficient
k_{BCF} — Burton, Cabrera, and Frank growth rate parameter
k_g' — growth rate coefficient in the BCF model
k_v — crystal volume shape factor
l — light path length
l_j — Lagrange interpolation polynomial of degree j
$m(L)$ — particle, or crystal mass density distribution
$\mathbf{L}$ — linear matrix operator for sensitivity analysis
$\mathbf{m}$ — vector of mass density distribution values at quadrature locations
n — number of sieves, or number of photodiodes

s — radius of annular scattered energy detector
t — time
t_0 — initial time of batch run
t_f — final time of batch run
$\mathbf{u}$ — vector of system inputs (manipulated variables)
w_i — weight on i^{th} sieve, i^{th} residual weighting function, or the quadrature weight at the i^{th} quadrature point
$\mathbf{x}$ — vector of external coordinates, or vector of system states
$\mathbf{y}$ — vector of internal coordinates, or vector of system outputs
y_{ij} — i^{th} measurement taken at the j^{th} sampling instant
$\tilde{y}_{ij}$ — model prediction for the i^{th} measurement taken at the j^{th} sampling instant
$\mathbf{z}$ — vector of particle's coordinates

UPPER CASE SYMBOLS

A_{ij} — element of derivative weight matrix for collocation
A_c — heat transfer area for cooling crystallizer
B — rate of crystal formation mechanisms
$\mathbf{B}_j$ — matrix for linearized model at j^{th} sampling instant
B° — rate of crystal nucleation at size L_0
C — solute concentration (mass of solute/volume of slurry)
$\hat{C}$ — solute concentration (mass solute/mass of solvent)
C_{sat} — solute saturation concentration (mass of solute/volume of slurry)
$\hat{C}_{\text{sat}}$ — solute saturation concentration (mass of solute/mass of solvent)
D — rate of crystal removal mechanisms
E_b — nucleation rate activation energy
E_g — growth rate activation energy
F — focal length of lens in particle sizer
G — crystal growth rate
$\mathbf{H}$ — smoothing matrix
ΔH_c — heat of crystallization
H_{ext} — net external heat removal

I — intensity of scattered light
I_0 — intensity of incident light
J_0 — Bessel function of the zeroth kind
J_1 — Bessel function of the first kind
K — optical constant of particle sizer
L — characteristic particle or crystal size
L_0 — characteristic size of nuclei
L_{wm} — weight mean size
L_{N_u} — upper bound on nucleated crystal size
L_{S_l} — lower bound on seed crystal size
L_{S_u} — upper bound on seed crystal size
M_T — slurry density, $\rho_c k_v \mu_3$
N_d — number of measurement samples during an experiment
N_m — number of quantities measured
N_p — number of parameters estimated
P — pressure
Q — volumetric flow rate
S — supersaturation, $(C - C_{\mathrm{sat}})/C_{\mathrm{sat}}$
$\hat{S}$ — supersaturation, $(\hat{C} - \hat{C}_{\mathrm{sat}})/\hat{C}_{\mathrm{sat}}$
$R_{\max}$ — maximum allowable cooling rate
T — temperature
$\mathbf{T}$ — vector of temperature values at n points in time between $t = 0$ and $t = t_f$
T_c — coolant temperature
$T_{\min}$ — lower bound on crystallizer temperature
$T_{\max}$ — upper bound on crystallizer temperature
U — heat transfer coefficient
V — volume of the crystallizer's contents
$\mathbf{V}$ — measurement error covariance matrix
$\mathbf{V}_\theta$ — parameter covariance matrix for the linearized problem
W — weight of crystals introduced into batch view cell

Greek Symbols

α — joint confidence limit

$\chi^2_{N_p}$— Chi-square statistic with N_p degrees of freedom

δ — Dirac delta function

$\boldsymbol{\delta\theta}_{\max}$— maximum possible deviation from $\boldsymbol{\theta}^\star$ within confidence region— major axis endpoints

$\boldsymbol{\delta\theta}_{\text{worst}}$— parameter deviation direction that has largest effect on optimal control policy

γ — penalty weight in constrained linear inversion, or scaling factor

ε — volume fraction of continuous phase

$\boldsymbol{\theta}$ — vector of parameters

$\boldsymbol{\theta}^\star$ — nominal parameters set

λ — wavelength of light

λ_i — i^{th} eigenvalue

μ_k — k^{th} moment of the CSD = $\int_0^\infty f L^k dL$

$\hat{\mu}_3$ — 3^{rd} moment of the CSD with units cm^3/g solvent

ρ — density of the crystallizer contents

ρ_c — crystal density

σ_i^2 — variance of i^{th} measured variable

τ — turbidity, or crystallizer residence time

ω_i — weight for the ith measurement in the parameter estimation objective function

Φ — parameter estimation objective function

ζ_{N} — nucleated crystal size transformed to [0,1] domain

ζ_{S} — seed crystal size transformed to [0,1] domain

Subscripts

k — k^{th} flow stream

Chapter 1

Introduction

The beginning is the half of all.
— Greek Adage

1.1 Project Motivation and Research Goals

As suggested by the account in Genesis of the demise of Lot's wife, the observation of crystallization dates to antiquity. Crystallization has now become one of the most common separation techniques in the chemical industry. For example, Du Pont estimates that approximately 70% of their products pass through a crystallization or precipitation stage [64]. Despite its roots and its extensive use, modelling and control of crystallization processes continue to present many problems that require fundamental research.

One of the basic challenges in characterizing and controlling crystallizers is their distributed nature. Distributed parameter systems are processes with spatially varying states, controls, and parameters. The states, controls, and parameters of a crystallizer are spatially distributed, but they are also distributed over a population—the population of crystals. The development by Randolph and Larson [125] and Hulburt and Katz [78] of the population balance approach, a framework for modelling dispersed-phase systems such as crystallizers, enables representation of this distributed nature. Since the development of this approach, there have been lumped parameter modelling efforts, such as time-series models [80], but these ignore the basic nature of a crystallizer.

The quality of a crystalline product is usually specified in terms of the crystal size, shape, and purity. While the population balance approach allows consideration of the distribution of shape and purity of a population, this study deals with the modelling and control of crystal size and crystal size distribution (CSD). Customer quality requirements of a product are often stated in terms of ability to flow, dissolution rate, aesthetic appeal—all primarily functions of crystal size and CSD. For products to be used in photographic materials, size uniformity is so critical that the CSD is the principal consideration of a

customer. If acceptable CSD and purity standards are not met, the crystals must undergo further processing steps, such as milling or recrystallization. In addition to customer requirements, a concern of the manufacturer is the CSD-influenced efficiency of downstream processes such as thickening and filtration, often the time-limiting steps in crystallization operation.

The population balance provides a framework for modelling the CSD of a crystallizer, but finalizing the structure of the model requires an understanding of the underlying phenomena. While agglomeration and breakage of crystals can play important roles for some systems, the primary phenomena of crystallization processes are nucleation of new crystals and growth of existing crystals. As discussed in this dissertation, there has been significant effort in characterizing growth and nucleation rates and their dependence on process variables.

Both nucleation and growth are driven by supersaturation, the degree to which the solute concentration exceeds its saturation concentration. Supersaturation can be achieved by chemical reaction, temperature change, solvent evaporation, feed rate changes, and introduction of an additive. The size and CSD of a crystallizer product are governed by the rates of nucleation and growth; therefore, they can be influenced through the supersaturation. Because nucleation and growth compete for a resource (the solute) and are driven by the same variable (supersaturation), the control problem is challenging and requires a careful characterization of the kinetics of the two phenomena. The interdependence of nucleation and growth is also history dependent. A burst of nucleation will affect the surface area available for growth and the sites for secondary nucleation for the remainder of a batch crystallizer run or for several residence times of a continuous crystallizer.

In 1925, Griffiths [65] suggested simple strategies for influencing the product of a crystallizer. This was one of the first attempts to move crystallization design and operation from the realm of intuition to the realm of science; it predated the significant effort in crystallizer control that followed the development of population balance models.

With the aid of population balance models, some of the first researchers attempting to control continuous crystallizers suggested that manipulating variables such as feed rate and fines dissolution rate could stabilize a cycling crystallizer and minimize effects of disturbances [67, 68]. Beckman and Randolph [5] used simulations to demonstrate that proportional control of nuclei density using fines dissolution rate as the manipulated variable eliminates the commonly observed limit-cycle instability and minimizes transients; there has been experimental verification that this works [130, 128], but the nuclei density measurement is very difficult to obtain. As discussed by Rawlings et al. [132],

many attempts at continuous crystallizer control have followed.

Despite the activity in the area of continuous crystallizer control, Randolph pointed out in 1980 that the industrial practice of crystallization control could be summed up as "hold everything constant" [127]. Because of limitations of accurate process measurements and failures to properly identify models that characterize system behavior, this is still the common industrial approach.

Process measurement and model identification are particularly difficult for dispersed-phase systems such as crystallizers. The goals of this study included the review and analysis of measurement technology for crystallizers, and the analysis of the interplay between measurement, model identification, and model-based control. Although the measurement and model identification techniques developed and presented in this dissertation are generally applicable to a variety of crystallizer configurations, the focus of the development and the experimental verification was for batch crystallizers.

The simplicity and flexibility of batch equipment is ideal for plants with frequently changing recipes. Batch crystallization is used extensively in the chemical industry, often for small volume, high value-added specialty chemicals and pharmaceuticals. Nevertheless, there have been relatively few studies on the development of control algorithms for batch crystallizers.

As for any batch process, the hold-everything-constant policy used for continuous crystallizers is not a reasonable option for a batch crystallizer, and a dynamic operation policy must be determined. Therefore, the principal goal of this work was the determination of a model-based strategy for batch cooling crystallizers. Crystallization of potassium nitrate from water in a batch cooling crystallizer, the system used for verification of the model identification technique, was chosen for experimental testing of the control strategy.

1.2 Dissertation Overview

The following chapter provides a description of the construction and operation of the experimental system used in this study—a batch cooling crystallizer for potassium nitrate and water. One of the advantages of batch crystallization over continuous crystallization is the potential to obtain products with narrow CSDs. While seeded operation leads to CSDs with at least two modes and therefore widens the CSD, the batch crystallization runs in this study were seeded. As shown by Bohlin and Rasmuson [11] and Chianese et al. [27], seeding increases average crystal size and enables more reproducible operation than unseeded crystallization, and nucleated crystals often maintain the morphology of the seeds.

Chapter 2 also discusses methods for measuring the concentration of the

solute in the continuous phase and reviews techniques for measuring particle size. After summarizing the theory and shortcomings of a technique for measuring CSD using light scattering, this chapter demonstrates the use of a transmittance measurement to obtain particle size information.

Model identification is a twofold task that involves model formulation and parameter estimation. Chapter 3 presents the development of a general population balance model and the narrowing of this description to the more specific case of CSD modelling. The corresponding mass and energy balances are also given; additional details of the mass and energy balances are given in Appendix B. After reviewing the efforts in characterizing crystal nucleation and growth, constitutive relations for these phenomena are given. For a hypothetical physical/chemical system, two model solution techniques and their respective advantages and disadvantages are illustrated.

Chapter 4 discusses parameter estimation, the second stage of the model identification process. First, the crystallizer kinetic parameter estimation techniques that have been presented in the literature are reviewed. As discussed, there is considerable disagreement between published results for identical systems. This can be explained by the fact that most crystallization parameter estimation studies report no parameter uncertainty bounds, and the information content of the data of most of these studies is probably insufficient for reliable parameter estimation. Using experimental data, it is demonstrated that the maximum likelihood method, posed as a nonlinear optimization problem, leads to an efficient solution of the estimation problem; an assessment of the reliability of the estimates is included. It is then shown how the parameter uncertainty assessment can be used in experimental design.

Chapter 5 discusses an open-loop, model-based control strategy and demonstrates how it handles input, output, and final-time constraints. The results from experimental implementation on the KNO_3–H_2O system are also presented. This chapter includes an investigation of the issue that links the parameter estimation and model-based control problems—the sensitivity of control policies to parameter uncertainty.

The open-loop control policy is effective for the system of interest, but disturbances and plant/model mismatch may be significant for some systems. The use of feedback to mitigate the effects of disturbances and the inability to accurately predict system behavior is also discussed.

The final chapter summarizes the results of this study and suggests possible future directions in the field of crystallizer model identification and control.

The model-predictive controller used to control the crystallizer temperature is discussed in Appendix A. Some of the advantages and features of model-predictive controllers are illustrated in this appendix.

Chapter 2

Experimental Apparatus and Measurement Techniques

...there must be a certain conformity between nature and thought. Experience teaches us that...such a conformity does exist.

— Heinrich Hertz

This chapter describes the bench-scale, batch cooling crystallization system used to test the model identification and control strategies discussed in subsequent chapters. A discussion is also given of the measurements that are available for cooling crystallizer systems, including an analysis of the use of light transmittance to obtain information about the crystal size distribution.

Collection and processing of information are essential activities in experiments for model identification; reciprocal communication between the system and the user interface is required for control action implementation. A description is given of the equipment, the measurement techniques, and the hardware and software used for data acquisition and control signal transmission. A schematic of the crystallization system, including the control actuators and measurement devices is given in Figure 2.1.

The techniques presented in this study are sufficiently general to be applied to a wide variety of chemical systems, but a simple chemical system was desired for the verification of these methods. Because of the following attributes, a potassium nitrate and water system was selected:

- crystal shape is fairly constant over all sizes
- metastable zone is wide with respect to ability to control temperature
- growth rate is considered to be independent of size

The physical properties for the KNO_3–H_2O system are given in Appendix C.

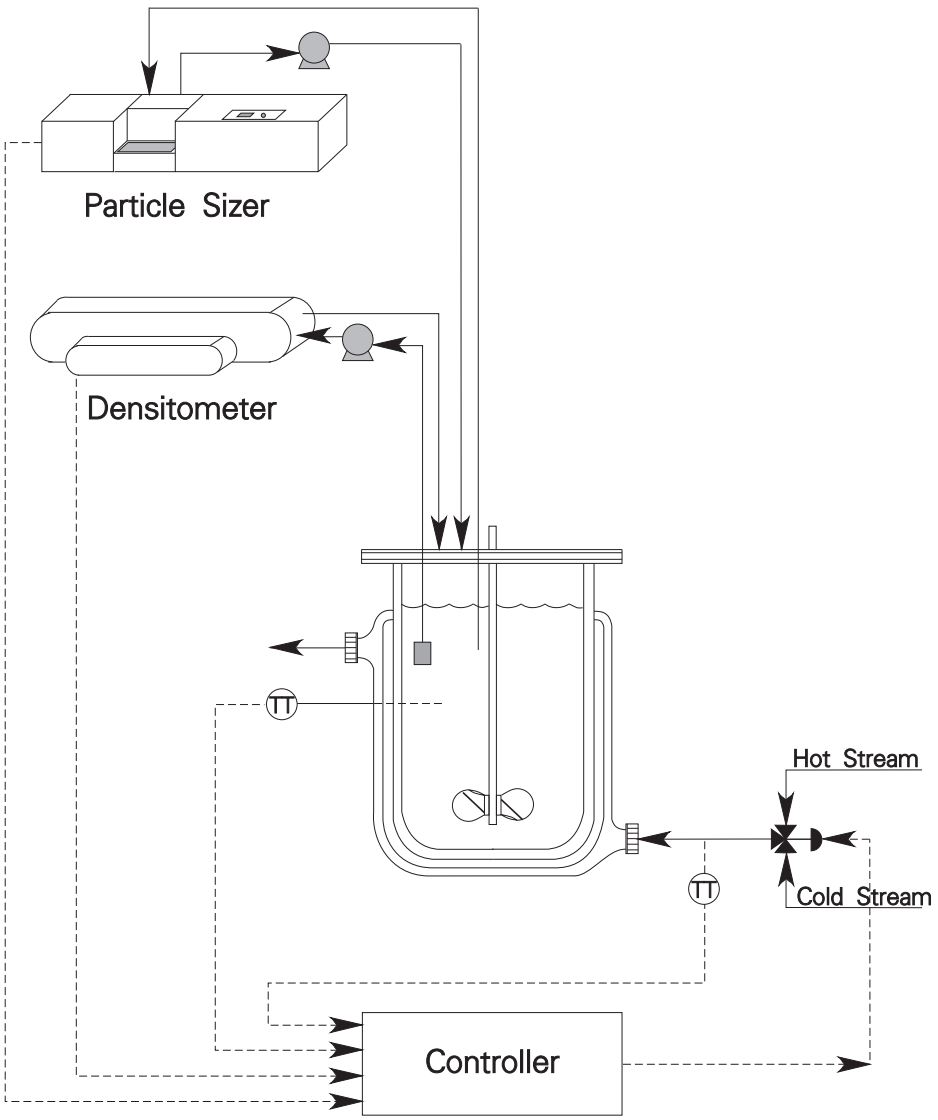

Figure 2.1: Schematic of the batch crystallization system.

2.1 Crystallizer

The phenomena involved in crystallization from solution are still poorly understood, and the measurement devices for a system are complex, but the crystallizer vessel—especially a batch cooling crystallizer—is relatively simple. Figure 2.2 is a schematic of the crystallizer used for the experimental portion

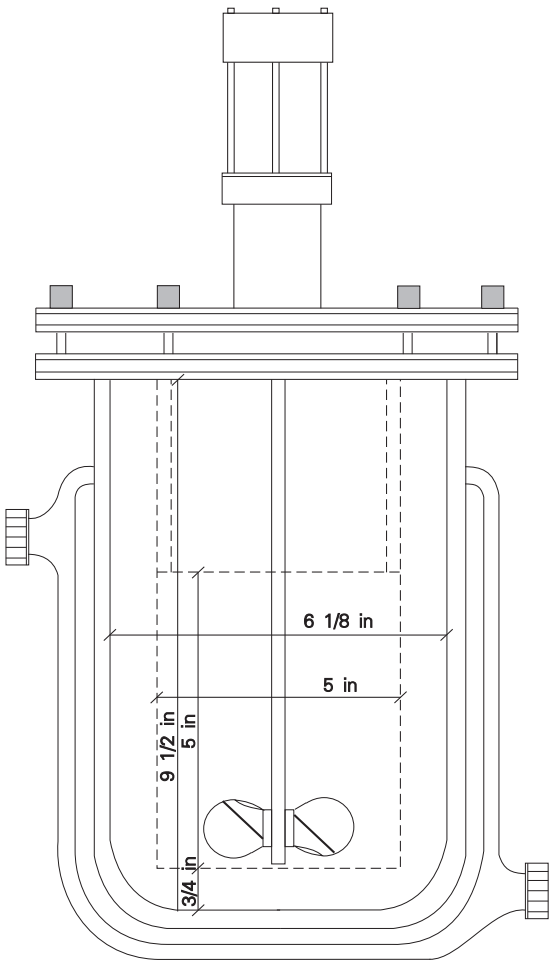

Figure 2.2: Crystallization Vessel.

of this study; the dimensions of the crystallizer are given in the schematic.

The glass, jacketed, flat-bottomed, 3-L vessel is produced by APPLIKON. It has a stainless-steel headplate with several sample ports and is fitted with a draft tube and a built-in impeller that is oriented to force the flow down through the tube. The removable DC stirrer motor has a range of 0 to 1250 rpm. After several test experiments, it was found that a stirrer speed of 475 is sufficient to create a well-mixed solution and to minimize settling of KNO_3 crystals.

2.2 Operator Station

The operator station provides the interface between the operator and the crystallization system. Its tasks include data acquisition, process monitoring, and control implementation. The operator station consists of a Digital Equipment Corporation (DEC) VAXStation II computer with boards for receiving and sending analog and digital signals, and an Analog Devices signal conditioning system that couples the computer and the process equipment.

2.2.1 Data Acquisition and Communication with VAXStation

A DEC VAXStation II with a VMS 5.0 operating system is the communication link between the operator and the crystallization system, performing the tasks of acquiring, displaying, and storing data, and computing and transmitting control signals. To enable transfer of analog and digital signals, the VAXStation was modified with the addition of three boards that are produced by DEC—the AXV11-C analog input/output board, the AAV11-C analog output board, and the DZQ11 asynchronous multiplexer board.

The DEC AXV11-C is capable of converting 16 single-ended, 0-10V analog signals to digital signals with 12-bit resolution. This card also has two 12-bit digital-to-analog converters that enable transmission of 0-10V signals. Transmission of analog output signals also can be performed with the AAV11-C board, which has two 12-bit digital-to-analog converters with 0-10V outputs.

Communication with and control of the AXV11-C and AAV11-C boards is facilitated by the device drivers available in MicroVMSLIB, the Data Translation subroutine library. As the name implies, MicroVMSLIB is written for computers running the MicroVMS operating system; however, with the aid of DEC's *VMS Programming Support Manual (Volume 8: Device Support Manual)*, the two necessary drivers were modified to work with a full VMS system. Subroutines are included in the library for communication between FORTRAN routines and the interface boards.

The DEC DZQ11 board has four ports for serial communication with instruments that have RS-232C interfaces. The VMS command "set term" can be used to configure each port to be consistent with the transmission rates and format of an instrument interface. The VMS utility routines for assigning channels to ports (SYS$ASSIGN) and for queued input/output (e.g., SYS$QIOW) can be used in FORTRAN code to communicate with instruments through the serial ports.

2.2.2 Signal Conditioning System

For analog signals, the 3B Series Signal Conditioning I/O Subsystem produced by Analog Devices, Inc. provides the link between the VAXStation II and the process equipment. It consists of a mounting backplane and a family of plug-in input and output signal conditioning modules. For example, input modules are available for exciting and monitoring resistance temperature detectors (RTDs) and converting the signal to a 0-10V signal (like that required by the AXV11-C board); output modules are available for conversion of a 0-10V signal (like that from the AAV11-C board) to a 4-20mA signal.

2.3 System for Manipulation of Crystallizer Temperature

The glass crystallizer/jacket wall is a poor thermal conductor and does not provide a large heat-transfer surface area. To effectively manipulate the crystallizer temperature, it must be possible to change the jacket temperature rapidly over a large temperature range. To achieve this requirement, the stream of water to the jacket is split into one stream that is cooled and one stream that is heated, and the streams are remixed by a 3-way control valve in proper proportion to attain the desired temperature. The water for the jacket is maintained at a constant flow rate by a positive displacement pump.

The pump is a Micropump Model 220/56C gear pump, which is a suction-shoe style that requires higher outlet pressure than inlet pressure. The inlet is pressurized, but the pressure drop through heat exchangers, valves, and the jacket is such that the pressure difference necessary to keep the suction shoe in place is available at full flow. To avoid a problem at startup, an external bypass loop was installed to allow the following procedure: fully open the bypass-loop valve before opening the supply-water valve, gradually open the supply-water valve to pressurize the system, start the pump, close the bypass-loop valve.

Copper tubing in an ice bath provides the heat sink for one stream, while the hot stream is the product of a double-pipe heat exchanger constructed of 7-feet lengths of 1/4-inch copper and 3/4-inch stainless steel tubing. The heat source for the annular region of the heat exchanger is a Sentra Temperature Controller with a 9-kilowatt heater and 0.75-horsepower pump (model S-915) manufactured by Advantage Engineering, Inc.

The valve used to manipulate the mixture of the two streams, and thus the jacket inlet temperature, is a 1/2-inch, 3-way research control valve with a 115 VAC EVA-1 actuator produced by Badger Meter, Inc. The valve trim size is G (valve flow coefficient =0.2). The actuator positions the stem in

proportion to its 4-20mA input signal.

The input signal for the valve actuator is the output signal of an Omega Engineering, Inc. CN-2002 PID temperature controller, which uses the signal from an RTD in the crystallizer jacket to move the jacket temperature to its set point. Because of the length of tubing in the ice bath and heat exchanger and the dependence of the heat transfer in the tubing on the flow rate, the gain of the system to be controlled by the Omega controller is variable. Nevertheless, the controller was tuned for a given operating region using the procedure recommended by Omega (basically, Ziegler-Nichols tuning). For the temperature range 20°C–32°C, the expected operating region, the following tuning parameters were found: 22% proportional band, 6.4 resets/minute, and a derivative time constant of 0.01 minutes. The performance with these tuning parameters proved to be adequate for operation well outside of the 20°C–32°C temperature range.

The response of the jacket temperature to changes in the valve stem position is much faster (time constant of less than 30 seconds) than the response of the crystallizer temperature (time constant of approximately 15 minutes). The most likely sources for a disturbance of the crystallizer temperature are changes in the supply water temperature, the ambient temperature, and the heat transfer effectiveness of the ice bath and heat exchanger. All of these potential disturbances of crystallizer temperature are first manifested as disturbances of the jacket temperature.

The jacket temperature responds quickly to manipulated variable changes, and disturbances are detected by the jacket temperature measurement; therefore, a cascade control configuration as illustrated in Figure 2.3 can reduce the effect of disturbances on the crystallizer temperature. The primary controller is the crystallizer temperature controller; it uses the crystallizer temperature measurement and set-point trajectory to compute a set point for the jacket temperature controller. This secondary-loop controller is the Omega controller, which measures the jacket temperature and adjusts the valve to set the flow ratio of the hot and cold streams.

The primary controller uses the model-predictive control scheme discussed in Appendix A. The computation is performed by the VAXStation II, and the set point for the secondary control loop is sent through the DZQ11 serial port to the RS-232C interface of the Omega controller.

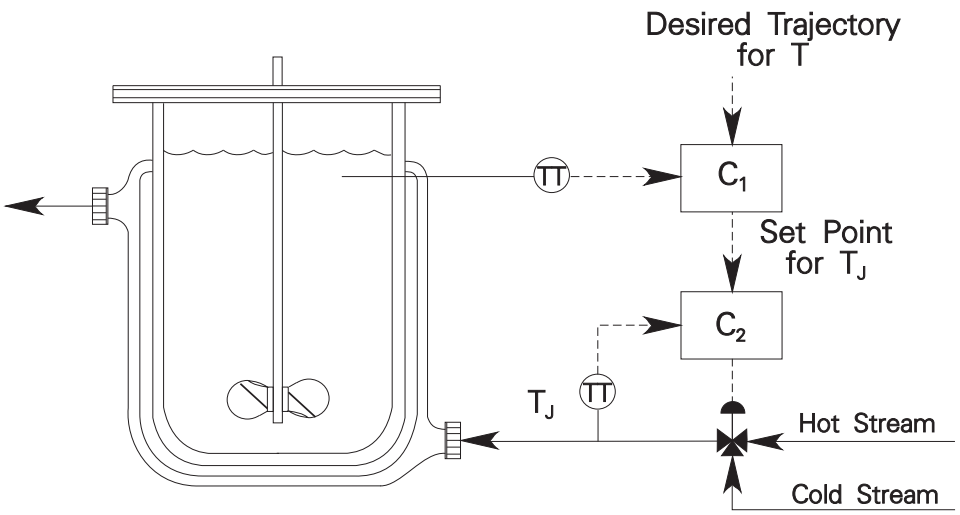

Figure 2.3: Cascade configuration for control of crystallizer temperature.

2.4 Measurement Devices and Techniques for Crystallization Processes

The discussion of this section focuses on the measured variables available in crystallization processes and is important background for understanding the parameter estimation and control problems discussed in subsequent chapters.

2.4.1 Temperature Measurements

Process temperature is measured using Omega 3-wire, 100Ω, platinum resistance temperature detectors (RTDs) (model PR-13-2-100-1/8). The RTD excitation is provided by a Model 3B34 Analog Devices module, which also provides a 0-10V output signal. The voltage signals from the RTD signal conditioners are digitized by the DEC AXV11-C board in the VAXStation II.

2.4.2 Concentration Measurement

A measurement of the concentration of the solute in the continuous phase is needed to characterize the state of a crystallizer. There are several methods for the rapid measurement of solids-free concentration. It has been shown that quick and accurate determination of concentration from the measurement of refractive index is possible [71, 105, 150]. Garside and Mullin [56] suggest the use of an on-line densitometer to determine solution concentration. Qiu

and Rasmuson [120] report successful use of density measurements in assessing concentration of samples extracted from a crystallizer, and Witkowski [173], and Riebel et al. [137] have demonstrated the use of densitometry for accurate, on-line concentration measurements.

An Anton Paar densitometer (model DPR 412 YE) with a 2-millimeter, flow-through stainless steel measuring cell is used in this study for determination of the solute concentration of the solids-free phase. A solids-free stream is obtained by filtering through a 15-micron screen in the crystallizer. The stream is pumped at a rate of 100 milliliters/minute. The measuring cell is equipped with a Pt100 RTD temperature sensor.

The typical use of this instrument is to measure the density of a fluid after correlating the period of the oscillation of the measuring cell to the known densities of calibration fluids. In this study, a measurement of concentration of the solute (KNO_3), which has a one-to-one relationship with the solution density at a given temperature, is desired.

A series of calibration runs was performed with the KNO_3–H_2O system to obtain oscillation period measurements for solutions of known concentrations and temperatures. As demonstrated by Witkowski [173] for a Paar DPR 4112 XE measuring cell and confirmed in this study for the DPR 412 YE, the relationship between temperature and oscillation period of the cell for a given concentration is linear over a wide temperature range. Data from the calibration runs also demonstrated that, for a given temperature, the relationship between concentration and oscillation period is linear.

To obtain a concentration measurement from the measurement of the densitometer oscillation period and temperature, a four-point linear interpolation is used on the calibration data to obtain oscillation period versus concentration at the measured temperature. Linear regression is then used to obtain a relationship between period and concentration that, with the measured period, yields the concentration measurement.

Data taken by Witkowski [173] demonstrate that the oscillation of the measuring cell is very sensitive to temperature and must be in thermal steady state to enable accurate measurements. In this study, the temperature of the crystallizer is a manipulated variable, so the dynamics of the temperature could pose a problem. To keep the temperature of the fluid to the densitometer constant (or at least slowly changing), a Haake F 4-C water bath and circulator is used to trace the densitometer inlet line and provide a heat source for a heat exchanger on the inlet line and the jacket of the DPR 412 YE. The heat exchanger is a double-pipe exchanger of length 40 inches; the outer pipe is constructed from 3/8-inch stainless tubing, while the inner pipe (process-stream) is 1/8-inch aluminum tubing.

The bath temperature is kept at 34.7°C, which is several degrees higher than the highest crystallizer operating temperature. This maintains the densitometer temperature at a fairly constant value, even when the crystallizer temperature changes significantly (e.g., a change in the crystallizer temperature from 32°C to 28°C leads to a decrease in the densitometer temperature of less than 0.3°C). Several verification runs were performed with solutions of known concentrations to demonstrate that the concentration measurements are reproducible and accurate to within $\pm 1 \times 10^{-4}$ g KNO_3/g H_2O.

Another 40-inch, double-pipe heat exchanger is used to reduce the temperature of the return stream to a temperature near that of the crystallizer. The heat sink for this exchanger is the stream used to trace the line to the particle sizer (see Section 2.4.5).

When a measurement is performed by the densitometer (on intervals of approximately 10 seconds), a Paar DPR-S RS-232C serial interface sends the data (strings containing the temperature and period of the oscillation of the measuring cell) to the VAXStation II DZQ11 serial port. The VMS system services routine SYS$QIOW is used to wait for and read the data strings, which are subsequently parsed into the temperature and period values. Taking into account the flow to the densitometer and the time required by the Paar instrumentation, the dead time for this measurement is approximately 25 seconds.

2.4.3 Dynamic Crystal Size Distribution Measurement

Obtaining on-line information about the CSD is necessary for the development and implementation of crystallizer control algorithms, and as demonstrated in Chapter 4, accurate measurement of solid-phase properties is required for uniquely determining the model's nucleation and growth parameters. This section provides an overview of the available methods for particle sizing with emphasis on a laser light scattering method. The instrument used in this study—one based on light scattering—is then discussed.

Bunville [20] and Lieberman [99] point out that there are now several commercially available instruments, based on a wide variety of physical phenomena, that provide on-line particle size information. Coulter counters are based on electrical resistance differences between the particle and solution. Sedimentation and hydrodynamic chromatography are based on transport properties. Optical properties give rise to techniques based on diffraction, light blockage, and direct imaging. Rohani and Paine [140] suggest a device for measuring suspension density based on the temperature change required to dissolve crystals in a sample cell. Unfortunately, no method developed to date is with-

out restrictions and problems. Coulter counters suffer from orifice blocking problems that prohibit industrial application, or at least restrict their application to streams that have been classified by size. Coulter counters and optical-property techniques are sensitive to the presence of foreign particles and entrained bubbles. The temperature-difference technique of Rohani and Paine is not affected by foreign particles and bubbles, but requires substantial calibration to allow absolute suspension density measurement and is better suited for detecting changes in suspension density.

Particle sizing with light scattering is an attractive candidate in crystallization applications because it generally avoids the pore plugging problems of Coulter counters, requires little calibration, and is easily automated for possible use as a feedback signal for a controller. Randolph et al. [131] use an on-line laser particle sizer to monitor the nucleation and growth rate of a continuous KCl crystallizer. Brown et al. [16] and Felton and Brown [50] use light scattering to monitor sugar and KI crystal growth rates, respectively.

2.4.4 Particle Sizing Using Light Scattering Theory

Particle sizing with laser light scattering is based on the interactions between an incident light source and solid particles. The amounts of reflection, refraction, and absorption of the incident wave depend on the refractive index of the particle, its geometry, and the wavelength of the incident light. The full Maxwell equations for the electromagnetic field at all spatial points due to interaction with an optically smooth sphere can be solved analytically [103]. This solution, known as Mie scattering, allows one to predict the intensity of the scattered light as a function of scattering angle; it involves complex, oscillation functions that can be evaluated efficiently using numerical methods given by Dave [33] and Wiscombe [172].

In most crystallization applications, the crystals of interest are large compared to the wavelength of the incident light (typically a He-Ne laser, $\lambda = 0.632$ μm). For these large particles, the phenomenon primarily responsible for scattering light in the "near-forward direction" (small scattering angles) is Fraunhofer diffraction. In studies by Jones [91], Fymat and Mease [52], and de Boer et al. [34], the full Mie scattering solution is compared with Fraunhofer diffraction results, and it is shown that, for many cases of interest, a valid assumption is that the near-forward scattering pattern is due solely to Fraunhofer diffraction. An advantage to the Fraunhofer approximation is that the scattering depends on the projected area of the particle and is independent of refractive index.

Figure 2.4 is a schematic of a particle sizing instrument developed by Swith-

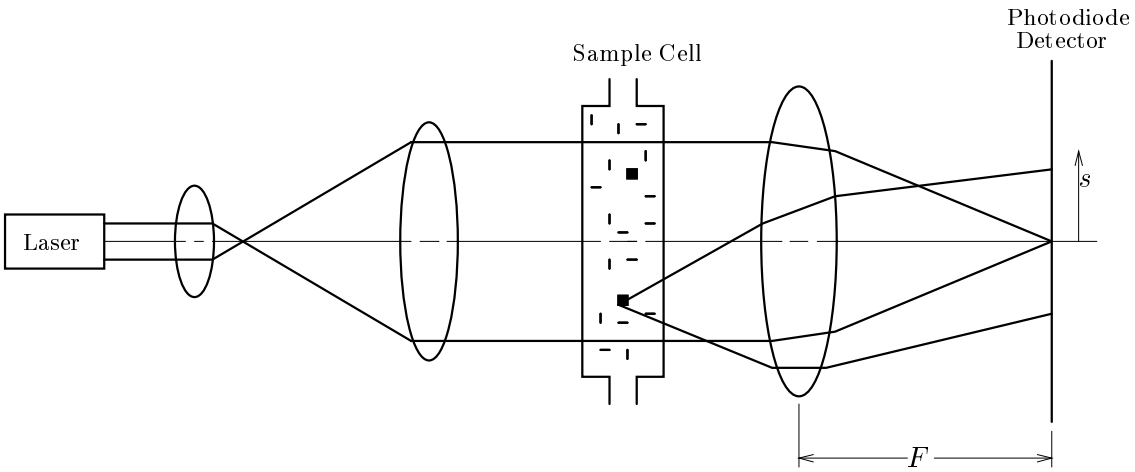

Figure 2.4: Schematic of a particle sizer based on light scattering.

enbank et al. [153]. The scattered intensity pattern is difficult to measure, so the instrument measures the scattered energy pattern. An array of photodiodes like the concentric annular photodiodes shown in Figure 2.5 can be used to measure the energy pattern. A detector can be placed at the center of the array to allow alignment and measurement of the transmission of unscattered light.

The advantage of measuring the energy pattern is that although the scattering intensity decreases markedly with increasing scattering angle (increasing s), the areas of the photodiodes can be made to compensate and reduce problems related to the limited dynamic range of the photodiodes. For example, the Malvern 3600Ec used in this study and discussed in Section 2.4.5 has 31 annular photodiodes that increase in area by about three orders of magnitude from center to periphery. (The dimensions of the detectors of the Malvern instrument are given by Hirleman [42].)

For the instrument configured as shown in Figure 2.4 with annular photodiode detectors, the Fraunhofer approximation allows the derivation of the following simple expression for the energy that is scattered by a particle of

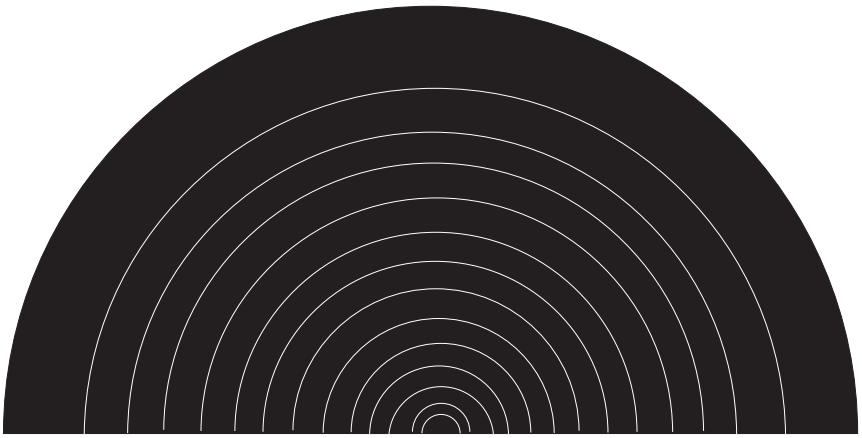

Figure 2.5: Depiction of array of photodiode detectors.

radius L to the i^{th} detector of inner and outer radii s_1 and s_1', respectively:

$$e(L, s_i) = K\pi L^2 \left\{ \left[J_0^2 \left(\frac{2\pi L s_i}{\lambda F} \right) + J_1^2 \left(\frac{2\pi L s_i}{\lambda F} \right) \right] - \left[J_0^2 \left(\frac{2\pi L s_i'}{\lambda F} \right) + J_1^2 \left(\frac{2\pi L s_i'}{\lambda F} \right) \right] \right\} \tag{2.1}$$

where F is the focal length of the lens, and K is an optical constant that depends on the power of the laser and the detector sensitivity.

If the suspension of particles passing through the sample cell is dilute enough that multiple scattering can be ignored, the energy of scattered light at the detector is a simple integration of the energies scattered by the individual particles times the number density distribution,

$$e_t(s_i) = \int_0^\infty e(L, s_i) f(L) dL \tag{2.2}$$

Because it has been assumed that the particles are spherical, an expression for e_t in terms of a mass density distribution instead of number density distribution is

$$e_t(s_i) = \int_0^\infty e'(L, s_i) m(L) dL \tag{2.3}$$

where $\int_{L_1}^{L_2} m(L) dL$ is the mass of particles of density ρ_c with $L_1 \leq L \leq L_2$, and $e'(L, s_i)$ is given by

$$e'(L, s_i) = \frac{3}{4\pi\rho_c L^3} e(L, s_i)$$

The conversion from number to mass distribution is made because mass distribution and, more commonly, the weight fraction distribution are usually desired.

Eq. 2.3 provides a means by which to predict the scattering pattern for a given CSD. However, particle sizing requires the solution of the inverse problem—determining the CSD based on a finite number of measurements of the scattering pattern.

One approach to the inverse problem is to employ a quadrature rule to evaluate the integral in Eq. 2.3, giving a matrix equation for the values of m at the p quadrature points,

$$e_t(s_i) = \sum_{j=1}^{p} w_j e'(L_j, s_i) m(L_j) \qquad i = 1, \ldots, n \tag{2.4}$$

in which n is the number of photodiodes, L_j are the quadrature points, and w_j are the quadrature weights.

If the weight fraction distribution is desired, $\mathbf{m}$ (the vector of $m(L_j)$) is normalized; therefore, the magnitudes of the constants ρ_c and K are not relevant and can be set to unity.

As is the case for many inverse problems, the inverse operator for the integral equation and, thus, Eq. 2.4 is ill-conditioned. This ill-conditioning is due to the fact that significantly different CSDs can give very similar scattering patterns; therefore, small errors in the measurement of e_t can lead to large errors in the CSD inference. Wing [170] reviews this class of problems and discusses the methods that have been developed to handle the ill-conditioning.

Since the matrix equation is in general overdetermined ($n > p$), one can solve the least squares problem for the $m(L_j)$. This fails in practice, because of the ill-conditioning of the $\mathbf{E}$ matrix ($E_{ij} = w_j e'(L_j, s_i)$); CSDs with wild variations, including negative components, are common. To illustrate, a scattered light pattern for a known particle size distribution was predicted from theory; Figure 2.6 gives the results of the least squares solution for this noise-free scattering pattern. This demonstrates the instability due to ill-conditioning, because the substantial error in the recovered distribution is for a case in which the only error in the scattered light pattern is on the order of the machine precision of the computer. To avoid these instabilities, statisticians often use a biased estimator called ridge regression [75], which simply uses a least squares objective function that is modified to include a penalty function on the variations in the solution. This is also sometimes referred to as constrained linear inversion (an unfortunate choice since constraints are not actually imposed). Phillips [117] and Twomey [160] suggest using a penalty on the sum of the squares of the second differences of the recovered distribution. The modified or penalized least squares solution is given by

$$\mathbf{m} = (\mathbf{E}^T\mathbf{E} + \gamma\mathbf{H})^{-1}\mathbf{E}^T\mathbf{e_t} \tag{2.5}$$

in which $\mathbf{H}$ is a smoothing matrix, an example of which is for the elements of $\mathbf{H}$ to be coefficients for the finite difference approximation to the second derivative.

A further modification to ensure a physically meaningful solution is to incorporate the constraint that the solution must be everywhere positive; the result is the following quadratic programming problem

$$\begin{aligned} \min_{\mathbf{m}} \quad & \mathbf{c}^T\mathbf{m} + \tfrac{1}{2}\mathbf{m}^T(\mathbf{B}^T + \mathbf{B})\mathbf{m} \\ \text{subject to:} \quad & m_j \geq 0, \quad j = 1, 2, ..., p \end{aligned} \tag{QP1}$$

where $\mathbf{B} = \mathbf{E}^T\mathbf{E} + \gamma\mathbf{H}$, and $\mathbf{c} = -2\mathbf{E}^T\mathbf{e}_t$. Note that the objective function is such that the Hessian of the QP problem is symmetric whether or not $\mathbf{H}$ is symmetric.

A comparison of Figures 2.6 and 2.7 demonstrates the benefit derived from the constrained, penalized inversion algorithm given by QP1. The distribution is inferred with greater success using this inversion algorithm than when using simple least squares, even though the data contain 5% random noise while the data used in the least squares inversion contain no added noise. While Figure 2.7 illustrates that the constrained, penalized least squares approach can be effective, careful choice of γ is necessary. The tradeoff is that γ must be large enough to avoid instabilities, but not so large that the solution is strongly biased. The approach used by many researchers is a trial-and-error procedure for determining γ [28], but other methods are available. Crump and Seinfeld [31] suggest a cross validation method for determining an appropriate value for γ. Shaw [148] demonstrates that γ can be treated as a parameter of a low-pass filter that removes the oscillatory modes of the solution; the eigenvalues of $\mathbf{E}^T\mathbf{E}$ can then be used as a guide for the selection of γ.

Boxman [13] suggests a method for solving the inverse problem by casting it as a weighted least squares problem. The weighting matrix is the inverse of the covariance matrix of the energy data; the covariance matrix is determined from the sweep-to-sweep variation for each detector. Boxman's algorithm includes a nonnegativity constraint on the solution.

A further complication of inferring the CSD from scattered light intensity measurements is due to the assumption that the particles are spherical. Brown and Felton [15] suggest making particle shape corrections using a theorem proved by van de Hulst [163] that states that the average geometrical cross section of a convex particle with random orientation is one-fourth its surface area. The light scattering results are taken to be for equivalent spheres, and the theorem is used to shift the equivalent-sphere diameter to a characteristic length of the actual particle. Jones et al. [88] demonstrate that agreement

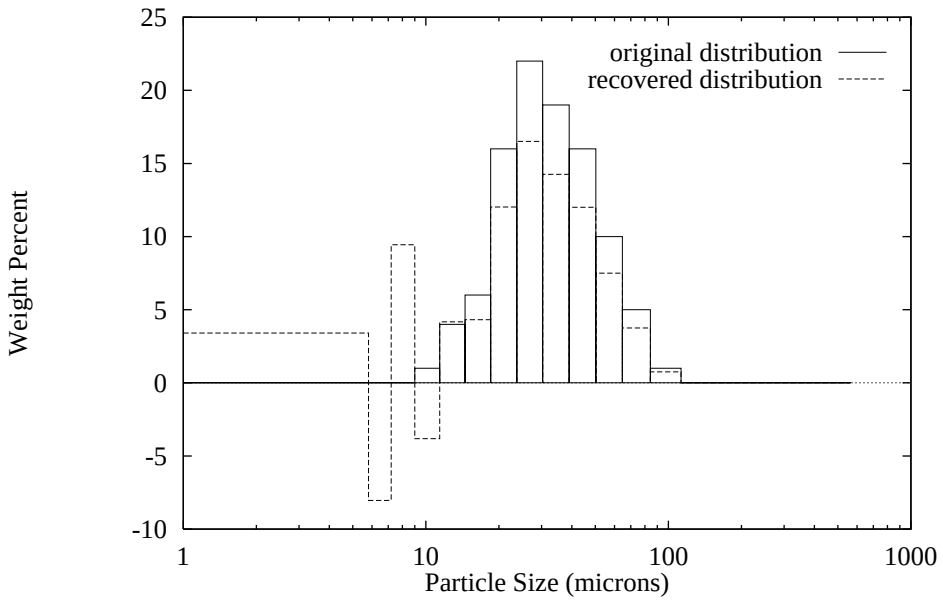

Figure 2.6: Recovery of the CSD from noise-free, simulated light scattering data using simple least squares.

with sieve analysis is obtained when this method is used to correct particle size to correspond to the characteristic length of potassium sulfate crystals.

Many crystals have needle or platelet morphological structures. Methods based on a shift of equivalent-sphere diameters could lead to large errors for such large aspect ratio particles. To illustrate, Figure 2.8 presents the results of a Malvern particle sizer (described in Section 2.4.5) for a monodispersion of cellulose acetate cylinders of diameter 45μm and length 195μm. (The cylinder samples were made available by Chester W. Sink of Eastman Chemical Company.) Note that instead of the description of a monodispersion, the distribution is bimodal with modes located near the primary dimensions of the cylinders. Obviously, no method that simply shifts the CSD would be adequate for crystals of large aspect ratios.

2.4.5 Malvern Particle Sizer 3600Ec

The instrument developed by Swithenbank et al. [153] and depicted in Figures 2.4 and 2.5 is produced commercially by Malvern Instruments. The in-

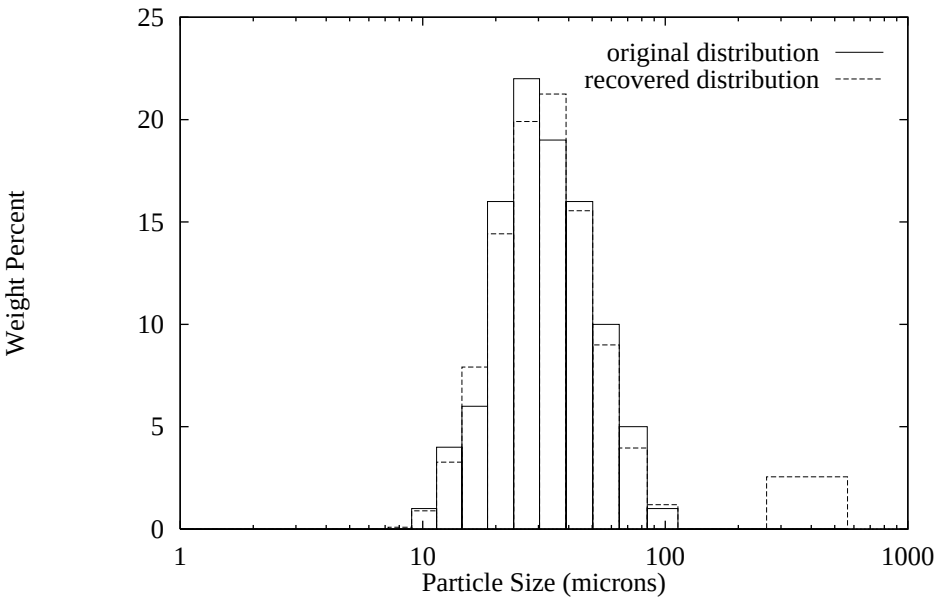

Figure 2.7: Recovery of the CSD from light scattering data with 5% noise using penalized and constrained least squares with $\gamma = 10^{-4}$.

strument has a flow-through view cell with a 2.0-millimeter light path length. In this study, the sample is obtained by continuously drawing a stream through a small tube (4 millimeters I.D.) in the crystallizer at a rate of 300 milliliters/minute using a Masterflex peristaltic pump. The flow rate is sufficiently high to obtain a representative sample, and the use of a peristaltic pump minimizes damage to the crystals.

The standard output of the system is the relative volume (or weight) CSD. The CSD can be determined by computing the parameters of a two-parameter distribution model (e.g., Rosin-Rammler, Log-Normal, or Normal distributions) by fitting the light scattering predictions to the measurements; this method is not suitable for cases of bimodal distributions. The alternative approach is the so-called "model independent" option in which a discretized CSD is determined as described in Section 2.4.4. Regardless of the method selected, the solution of the inverse problem suffers from the problems discussed in Section 2.4.4. A measurement of the transmittance (discussed in Section 2.4.6) is also made by the Malvern.

After measuring the scattering pattern and performing the computations,

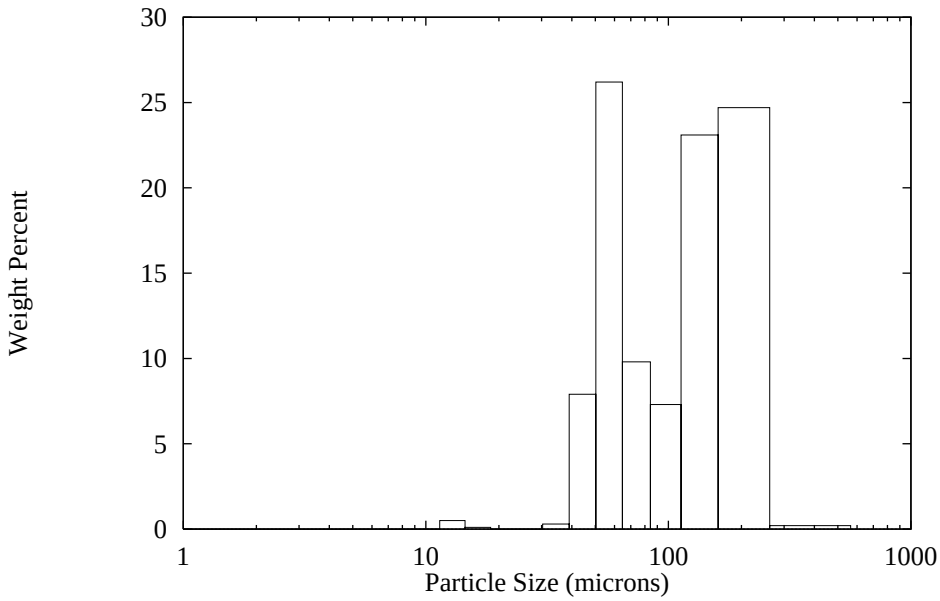

Figure 2.8: Malvern results for monodispersion of cylinders with 45 μm diameter and 195 μm length.

strings containing the data (transmittance and scattering pattern measurements, discretized CSD, etc.) are transmitted by the Malvern to a VAXStation DZQ11 RS-232C serial port. The VMS "set term" command is used to configured the serial port to conform to the Malvern transmission format. The VMS system services routine SYS$QIOW is used to wait for and read the data strings, which can be subsequently parsed to obtain the desired information. The Malvern interface is write only, but special strings are sent to mark the start and end of transmission and can be used to help detect transmission/reading errors.

To maintain the temperature of the streams to and from the Malvern particle sizer at a temperature equal to that of the crystallizer, a Haake F 4-C water bath and circulator is used to trace the lines. As mentioned in Section 2.4.2, after tracing the lines to and from the Malvern, this stream is used as a heat sink in a heat exchanger for the densitometer return stream. While two baths could have been used for the two tasks of tracing the Malvern sample stream and treating the densitometer return stream, tests demonstrated that, due to heat loss to the surroundings, maintaining the water bath at a temperature

of 1°C above the crystallizer temperature allows the following objectives to be met approximately: keep the temperature of the streams to and from the Malvern equal to the crystallizer temperature, bring the densitometer return stream to a temperature approximately equal to that of the crystallizer.

The crystallizer temperature is, of course, variable, but the Haake bath can receive remote set point changes. The set point of the bath temperature is set to track a trajectory that is always 1°C higher than that of the crystallizer. The protocol for set point changes is as follows:

$$\begin{aligned} 0\text{V} &\Leftrightarrow 0^\circ\text{C} \\ 1\text{mV} &= 0.01\text{V}/^\circ\text{C} \implies 1\text{V} \Leftrightarrow 100^\circ\text{C} \end{aligned}$$

The desired set point changes are effected by using a Data Translation device driver routine in a FORTRAN program to control transmission of 0-10V signals from the AAV11-C board. To improve resolution, a voltage divider is used to scale the 0-10V signal to a 0-1V signal.

Taking into account the flow to the Malvern and the time required for the Malvern to complete its computations, the dead time for this measurement is approximately 25 seconds.

2.4.6 Transmittance Measurement

As discussed by Witkowski et al. [174], information about the CSD can be obtained from a measurement of the transmittance, the fraction of light that is transmitted by the crystal slurry:

$$\text{transmittance} = \frac{I}{I_0}$$

where I is the intensity of scattered light that passes through the suspension of crystals and I_0 is the intensity of the incident light. The Malvern particle sizer allows measurement of transmittance, but it could be obtained with a spectrophotometer, a relatively inexpensive instrument.

The Beer-Lambert law provides a simple model that relates the transmittance to the CSD:

$$\frac{I}{I_0} = \exp(-\tau l) \tag{2.6a}$$

$$\tau = \int_0^\infty f(L) A_p(L) Q(L) dL \tag{2.6b}$$

where τ is the slurry turbidity, l is the flow cell width, $A_p(L)$ is the projected area for a crystal of characteristic size L, and $Q(L)$ is the extinction

efficiency factor. Assuming Fraunhofer diffraction is the dominant scattering phenomena, $Q = 2$ for all L (see van de Hulst [163]).

An extension to cases of nonspherical particles can be made by applying the theorem discussed in Section 2.4.4 relating geometrical cross section to surface area; the result is a transformation of Eq. 2.6b to the following

$$\tau = Q \int_0^\infty f(L) \left(\frac{1}{4}\right) (k_a L^2) dL = \frac{k_a}{2} \int_0^\infty f(L) L^2 dL \tag{2.7}$$

where k_a is the surface area shape factor (surface area of a crystal equals $k_a L^2$). Therefore, there is a one-to-one relationship between transmittance and the 2^{nd} moment of the CSD.

Validation of Transmittance Model. An assumption made in developing expressions for describing light scattering is that there is no multiple scattering. Hirleman [74] discusses multiple scattering and the effect it can have on measurements based on light scattering. Hirleman proposes a model for predicting the scattering pattern for a multiple scattering media of known size distribution. He suggests that this could be incorporated into an inversion algorithm, but a method for correcting the transmittance measurement is not given. Other studies have been made of the effect of multiple scattering and on methods to extend the light scattering theory to account for this effect on the mean size of the CSD [39, 161], but these methods are empirical and require calibration.

The following are rules-of-thumb given by van de Hulst [163] for multiple scattering effects: single scattering prevails for $\tau l < 0.1$; double scattering may occur for $0.1 < \tau l < 0.3$; multiple scattering can be significant for $0.3 < \tau l$. In other words, multiple scattering can be significant for transmittance values less than approximately 75%, in which case the validity of the Beer-Lambert law would be questionable. Meyer and Chigier [102] refer to some studies that suggest that the effects of multiple scattering are insignificant for levels of transmittance as low as 50%. Data from a study by Boxman [13] suggest that operation in the range $0.75 \leq \frac{I}{I_0} \leq 0.90$ provides a reasonable trade-off between effects of multiple scattering and large noise-to-signal ratio.

The light traveling parallel to the incident beam is focused by the instrument lens on the central detector. Therefore, disregarding phase-related interference, the only way that multiple scattering can affect the transmittance measurement is for light scattered by one particle to be scattered by another particle in a direction parallel with the incident beam. This would lead to a higher level of transmittance than would be predicted when assuming no multiple scattering.

The probability for light to be scattered more than once is significantly greater than the probability that this multiple scattering will result in light exiting the view cell parallel to the incident beam. Therefore, intuition would suggest that the overall scattering pattern should be more sensitive to multiple scattering than the transmittance measurement.

Experiments with dense sprays of fuel droplets are described by Dodge [39]. The scattering pattern data indicate that the measured mean droplet size decreases strongly with increasing droplet concentration; however, the relationship between the concentration of droplets and the logarithm of the transmittance is linear, as predicted by the Beer-Lambert law. While the relationship is linear, there is no independent measurement of droplet concentration allowing comparison with the Beer-Lambert prediction. Also, it is not clear that the slope of the curve remains constant over all concentrations (required by the Beer-Lambert law), because the experiments were for dense sprays only. Therefore, the study cannot be taken as a verification of the Beer-Lambert law.

To test the validity of the Beer-Lambert law and the method used to extend it to apply to nonspherical particles, experiments were performed with monodispersions of crystals of known size, number, and shape. Crystallization often involves slurries so dense that the assumption of negligible multiple scattering could break down; an additional goal of the experiments was to determine the range of transmittance over which the Beer-Lambert law is applicable.

The Malvern particle sizer was used to make transmittance measurements for sodium chloride crystals taken from a narrow size class of a sieve stack. The size and shape of the crystals were verified with microscopic observation before adding known weights of the crystals to a saturated NaCl solution in a magnetically-stirred, batch view cell with a 14.3-millimeter path length. NaCl crystals were chosen for two reasons: first, their shape is easily characterized (cubic) and is not a function of size; secondly, the solubility of NaCl is a very weak function of temperature, making it easy to avoid growth and dissolution.

With cubic crystals of known shape and size, the number of crystals, N, can be determined from the weight, W:

$$N = \frac{W}{\rho_c L^3} \tag{2.8}$$

From Eqs. 2.8, 2.6a, and 2.7, the Beer-Lambert law with shape correction gives

$$-\log\left(\frac{I}{I_0}\right) = \frac{3Wl}{\rho_c LV} \tag{2.9}$$

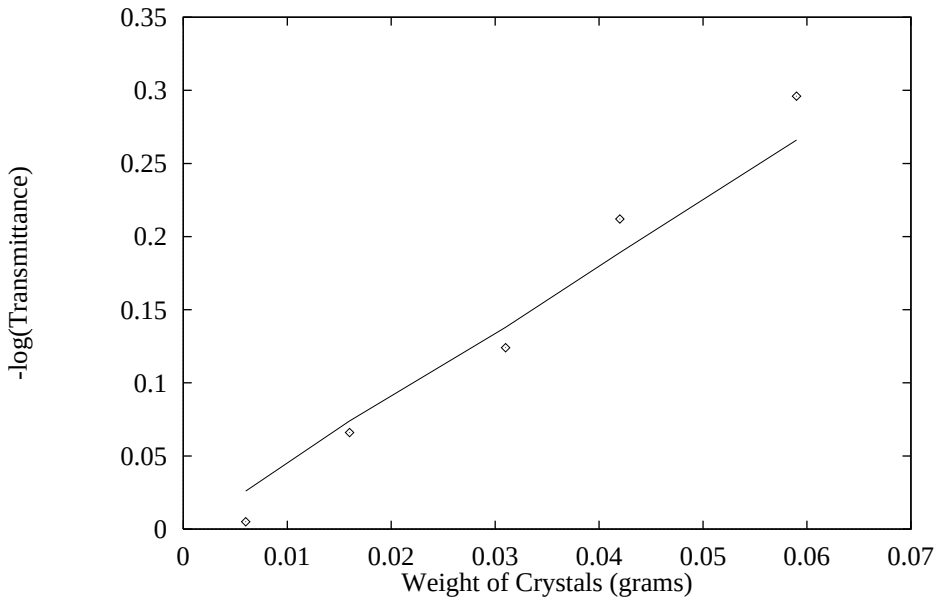

Figure 2.9: Comparison between measured transmittance and that predicted by the Beer-Lambert law for low concentrations of 275-μm NaCl crystals.

for a monodispersion of cubic crystals in a view cell of volume V and path length l.

The results for low concentrations of 275-μm crystals are given in Figure 2.9 ($\frac{I}{I_0} \geq 0.74$). There is reasonable agreement between the measured transmittance and that predicted by Eq. 2.9.

To check the crystal concentration ranges over which the Beer-Lambert law is valid, transmittance measurements were made over a wide range of NaCl crystal concentrations. As can be seen from Figures 2.10 and 2.11, validity of the Beer-Lambert law is a weak function of crystal size, but in general, the agreement between prediction and measurement is good down to $\frac{I}{I_0} \sim 0.7$.

The mechanism that has been suggested for the effect of multiple scattering and some computations of the study by Ou and Seader [112] would lead to the expectation that any divergence from the Beer-Lambert law would be such that more centrally transmitted light is measured than predicted. Nevertheless, this is not the effect demonstrated in Figures 2.10 and 2.11. To explain the discrepancy, interference effects must be considered.

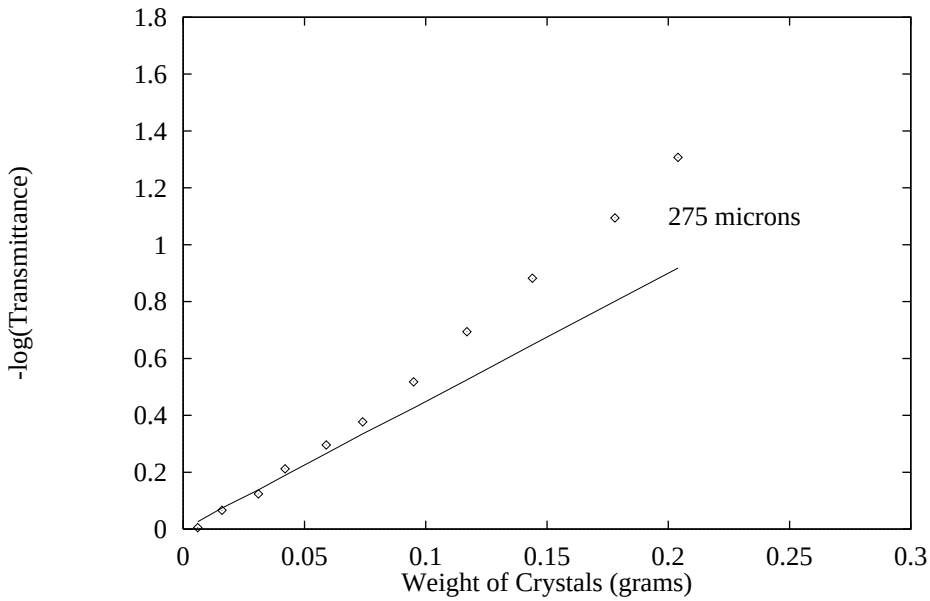

Figure 2.10: Comparison between measured transmittance and that predicted by the Beer-Lambert law for NaCl crystals of size 275 μm.

The angles of diffraction are small for light diffracted by crystals that are large in comparison with the wavelength of the light, but the scattering does lead to phase differences between a scattered wave and the incident beam and between waves scattered by different particles. Because phase differences between waves scattered by different particles are dependent on the positions of the particles, it is usually assumed that the net effect is such that phase need not be considered. Nevertheless, with an increasing number of scattering crystals, more and more light is scattered; therefore, an increased extinction efficiency due to increasingly strong interference effects between centrally transmitted and diffracted light would be expected. The divergence of the transmittance from that predicted by the Beer-Lambert law shown in Figures 2.10 and 2.11 is probably due to this interference effect.

The experiments outlined above verify the validity of the Beer-Lambert law for predicting transmittance, but they also confirm the rule-of-thumb given by van de Hulst—the use of the Beer-Lambert law for slurries with transmittance levels below $\sim$70% can lead to significant error. Fortunately, transmittance measurements for the experiments discussed in subsequent chapters are usually

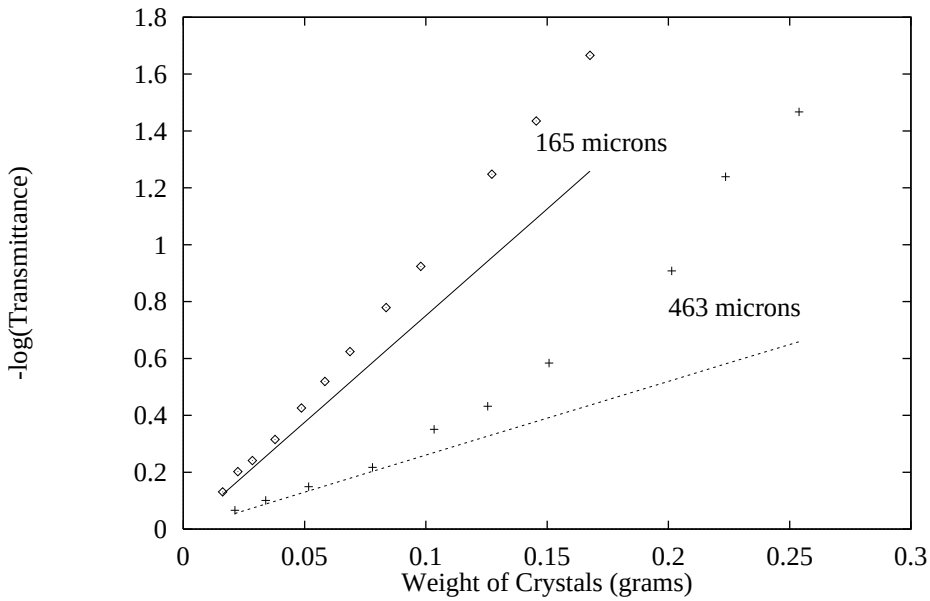

Figure 2.11: Comparison between measured transmittance and that predicted by the Beer-Lambert law for NaCl crystals of sizes 165 and 463 μm.

greater than 70%.

For cases in which on-line measurements from light scattering instruments are required and the slurry density is very high, Jager et al. [79] discuss the application of an automatic dilution unit. The challenge of this approach is maintaining a diluent of proper quality to assure crystal stability and a representative sample.

2.5 Product Sieve Analysis

Sieve analysis is the oldest particle sizing technique. It is time consuming and not suitable for control purposes. Nevertheless, sieve analysis does provide a method for comparing the CSD of the product of a crystallizer—at least qualitatively. In this study, a vacuum pump is used at the end of a batch run to rapidly transfer the product from the crystallizer to a jacketed flask maintained at a temperature equal to that of the crystallizer. The vacuum pump allows rapid transfer with no crystal damage. Most of the clear liquor of the sample

is quickly decanted and the remaining contents are immediately filtered under vacuum in a jacketed 9-centimeter Büchner funnel. The KNO_3 crystals are washed with acetone, dried for 10 minutes under vacuum, atmospherically for at least 2 hours, and in a desiccator for at least 24 hours.

After being dried, the crystals are segregated by size using a stack of 8-inch standard testing sieves that is shaken by a sieve shaker produced by CSC Scientific Company.

The discretized weight-size distribution obtained from the sieve analysis can be used to estimate statistical properties of the actual weight-size distribution. For example, if $f(L)$ is the population-size distribution function, the weight mean size is defined as:

$$L_{wm} = \frac{\int_0^\infty L^4 f(L) dL}{\int_0^\infty L^3 f(L) dL} = \frac{\mu_4}{\mu_3}$$

This can be approximated from the sieve data as follows:

$$L_{wm} \approx \frac{\sum_{i=1}^n L_i w_i}{\sum_{i=1}^n w_i}$$

where w_i is the weight of crystals on the i^{th} sieve and L_i is the average size of the i^{th} sieve size class.

The coefficient of variation ($c.v.$) of the distribution is defined as σ / L_{wm}, where $\sigma = \sqrt{\sigma^2}$, and σ^2, the variance of the distribution, is defined as:

$$\sigma^2 = \frac{\int_0^\infty (L - L_{wm})^2 L^3 f(L) dL}{\mu_3}$$

It can be shown that

$$c.v. = \sqrt{\frac{\mu_3 \mu_5}{\mu_4^2} - 1} \approx \sqrt{\frac{[\sum_{i=1}^n w_i][\sum_{i=1}^n (L_i^2 w_i)]}{[\sum_{i=1}^n (L_i w_i)]^2} - 1}$$

Therefore, the sieve data can be used to obtain an approximation for the coefficient of variation.

If performed in a consistent manner, sieve analysis is a reliable technique to check the quality of a sample of crystals. However, it should be noted that the measures of L_{wm} and $c.v.$ are subject to several sources of error; examples of sources of error are given below:

- The sieve analysis is a discretization of a continuous distribution.
- The nominal sieve screen sizes are based on the square openings, possibly skewing the results for crystals with high aspect ratios.
- The sampling procedure can lead to crystal damage.
- Agglomeration can take place during the drying process.

2.6 Crystallizer Operation

The operation of the crystallizer is outlined below:

- The lines to the measurement devices are cleaned by filling the system with water and circulating. The system is purged and the procedure is repeated several times.
- Because Swagelok Quick-Connect fittings are used to connect the instrument lines to the crystallizer, the vessel can be easily removed and thoroughly cleaned. After being disconnected, the lines are completely purged with compressed air.
- The crystallizer is charged with an initial load to give the desired concentration and then connected to the instrument lines. Typical load size is approximately 1650 grams of H_2O.
- The ice bath is filled and the Advantage water bath (the heat source for the jacket fluid) is set at 49°C. Using the interface to the Omega controller, the jacket temperature is manipulated to increase the crystallizer temperature to approximately 5°C above the saturation temperature. The stirrer is set to 475 rpm, and the potassium nitrate is completely dissolved. The elevated temperature is then maintained for 1 hour.
- The water bath for the densitometer jacket and inlet heat exchanger is set to be several degrees higher than the saturation temperature (bath set at 34.5°C for most runs). The water bath for tracing the Malvern lines is set to be approximately 1°C higher than the starting temperature. After starting flow to the instruments and the measurements reach steady state, the concentration is verified using the densitometer.
- The jacket temperature is manually manipulated to slowly decrease the crystallizer temperature to the desired starting point. The starting temperature is maintained for approximately 10 minutes.
- The water bath for the Malvern lines is switched to accept remote set points, and the start command is entered at the operator station to start the data acquisition and control routines.
- The transition from manual to automatic control is usually very smooth, but the temperature set-point trajectory is constant for at least the first 5 minutes to allow any transients to die out before seeding. It should be noted that "natural cooling" is effected by disabling the primary controller and entering a step change in the set point to the Omega

jacket-temperature controller; cooling then occurs according to Newton's law of cooling.

- After a carefully-weighed seed load is introduced, the operation requires no further supervision, with the exception of sample collection for sieve analysis. With the exception of a few specifically noted runs, the seed crystals are taken from the 180-212 μm sieve class, and the seed loading is low—approximately 0.05 grams. While it has been demonstrated that seeding can take place at significantly higher supersaturation levels without affecting product quality [93], seeding is performed at or near the saturation temperature.

2.7 Summary

A fully-instrumented, bench-scale batch cooling crystallizer was constructed for verification of model identification techniques and implementation of control schemes. The chemical system selected for experimental studies was potassium nitrate and water.

A Paar densitometer is used for on-line concentration measurement, and the light transmittance through a slurry sample is monitored by a Malvern 3600Ec particle sizer. The Beer-Lambert law provides a means by which to relate the transmittance to the second moment of the crystal size distribution.

The concentration and transmittance measurements, along with temperature measurements, are collected and processed by a DEC VAXStation II. The VAXStation II also computes the outputs of the primary controller of a cascade control scheme that tracks a desired crystallizer temperature trajectory.

Chapter 3

Model Formulation and Solution

If you don't like it, lump it.
— Thomas F. Edgar

A mathematical model of a process is a system of equations that enables prediction of the process behavior and its response to a set of inputs. The model can then be used for equipment design, to determine safe operating conditions, to estimate states of the system that cannot be measured, and to improve the control of the process. Modelling of chemical processes involves application of fundamental conservation principles, such as conservation of momentum, mass, and energy. This chapter discusses the population, mass, and energy balances for a crystallizer; the resulting equations, along with constitutive relations of material behavior, comprise the model of a crystallizer. These equations are then simplified to obtain a model for the batch crystallizer described in the previous chapter and used in the experiments discussed in subsequent chapters. This chapter also presents techniques for the solution of the crystallizer model.

3.1 Model Development

3.1.1 Population Balance

The objective of crystallization modelling is to provide a description of the population of the crystals dispersed in the continuous phase. The mathematical framework that has been developed to describe general dispersed phase systems is known as population balance modelling. The concept of a population balance arose as a generalization of the residence time distribution. In 1962, Rudd [143] demonstrated that one cannot always formulate a model based on particle age, and it is necessary to consider a generalized describing variable (catalyst particle activity in his example). Other early contributions were made by Randolph [125], Curl [32], and Behnken et al. [6]. These early efforts were followed by the classic paper by Hulburt and Katz [78] and book

by Randolph and Larson [129]. These authors extended the concept of particle size distribution to include an arbitrary number of "internal" coordinates to fully describe the state of a particle.

Tsuchiya et al. [159], Eakman et al. [43], and Ramkrishna [121, 122, 123, 124] apply this methodology to microbial populations. Hidy and Brock [73], Friedlander [51], and Hidy [72] review population balance methods in aerosol science applications. Rawlings and Ray [136, 133, 134, 135] review the use of population balance models in emulsion polymerization, and describe the advantages of this description over other models. Ramkrishna's [124] review article provides an extensive discussion of population balance modelling, applications, and solution methods.

While the studies cited above concern deterministic population balances, a stochastic framework can be used if fluctuations are large and need to be modelled for accurate predictions of observables of interest. Ramkrishna [123] and Fan and coworkers [76, 48, 77] present stochastic population balances. Ramkrishna points out that for cases of small populations of cells (e.g., sterilization processes), the fluctuations about the mean number of cells become of the same order of magnitude as the mean itself, necessitating the more complex stochastic machinery. Fan and coworkers, however, recommend using the stochastic approach even for large populations of crystals. They attempt to model CSD data displaying deviations from the decaying exponential size distribution expected of well-mixed crystallizers. It is not clear why a stochastic approach is required because the data can be fit by other deterministic models that include size-dependent growth or growth rate dispersion. It also seems plausible that, given the difficulty of solid-phase measurements, true crystal population fluctuations are likely not discernible in the presence of the inevitable measurement noise. In this case it would be reasonable to model the crystallizer with a deterministic population balance and simply append additive stochastic variables to account for the measurement noise. Deterministic population balances are used exclusively in this study.

The key property of the particulate system is some general number distribution function. Let $f(\mathbf{z}, t)$ denote the crystal distribution function, which depends on the time, t, and other suitably chosen coordinates, $\mathbf{z}$. The $\mathbf{z}$ coordinates include the usual three spatial (external) coordinates as well as the additional internal coordinates which are required to completely specify the state of the crystal. Let dV_z denote an infinitesimal volume in the crystal phase space. The total number of crystals per volume of crystallizer in some subregion of crystal phase space, Ω, is

$$\int_\Omega f(\mathbf{z}, t) dV_z$$

A population balance is derived by accounting for changes in the crystal number distribution due to changes in the coordinates $\mathbf{z}$ and any crystal formation and removal mechanisms. The mathematical arguments are analogous to those used in the development of conservation equations in transport phenomena [97]. The resulting population balance is

$$\frac{\partial f}{\partial t} + \nabla \cdot \left(\frac{\partial \mathbf{z}}{\partial t} f \right) = B - D \tag{3.1}$$

where B and D are the density functions of formation of new crystals and removal of existing crystals, respectively.

If one considers the well-mixed reactor, which has no spatial dependence, it is convenient to split the $\mathbf{z}$ coordinates into the external, $\mathbf{x}$, and internal, $\mathbf{y}$, parts,

$$\mathbf{z} = \begin{bmatrix} \mathbf{x} \\ \mathbf{y} \end{bmatrix} \tag{3.2}$$

Since neither f, B, nor D have any $\mathbf{x}$ dependence, the microscopic population balance can be integrated over $\mathbf{x}$ to give,

$$\frac{\partial (fV)}{\partial t} + V \nabla \cdot \left(\frac{\partial \mathbf{y}}{\partial t} f \right) = (B - D)V - \sum_k Q_k f_k \tag{3.3}$$

where $f_k(\mathbf{y})$ is the crystal distribution function of the k^{th} stream, Q_k is the volumetric flow rate of the k^{th} stream (positive sign denotes flow out), and V is the crystallizer slurry volume. With suitable choices of the Q_k, Eq. 3.3 describes batch, semi-batch, and continuous crystallizer operation. The crystallizer is clearly a distributed parameter system regardless of whether it is spatially distributed. To complete the description, one has to choose the internal coordinates, $\mathbf{y}$, specify the functional forms of $\frac{\partial \mathbf{y}}{\partial t}$, f_k, B, and D, and supply the necessary initial and boundary conditions. Specifying these functions and conditions requires a detailed understanding of the transport and kinetic events taking place, and is the major hurdle to overcome in modelling any particulate system.

Crystal Quality: Size, Shape and Purity. Eq. 3.3 is a general starting point, and has been used to address issues such as growth rate dispersion, coalescence and breakage of particles, and a variety of other mechanisms. The choice of internal coordinates in vector $\mathbf{y}$ is dictated by the intended use of the model. In industrial manufacture of crystals, the crystal quality is usually determined by the crystal size, shape, and purity. The vast majority of the engineering research literature is concerned with modelling the crystal size and size distribution.

The importance of crystal size and CSD is obvious: crystals that are too small are not easily separated from the mother liquor and may cause handling and environmental problems due to dust formation, and a poorly shaped CSD may lead to caking and promote agglomeration. However, it should be pointed out that crystal morphology and purity can play important roles in many applications. For example, precise control of the twinning grain morphology and size distribution in high speed films is vital for achieving their superior photographic properties. The aspect ratio of the particles in powdered reinforcement influences the strength and toughness of composite materials [138]. If the final product is a suspension of crystals in a liquid, the fluid rheology is strongly affected by the particle morphology [101]. As discussed by Rawlings et al. [132], recent progress may make habit and purity control a realistic goal in the near future.

CSD Modelling. Although states of a crystal such as purity and shape can be included as elements of $\mathbf{y}$, modelling the crystal size distribution (CSD) is considered in this study; in this case, the vector of internal coordinates is simply L, a characteristic crystal length, and f is a function of L and t. Assuming that there is no crystal breakage or coalescence and that crystals are nucleated at negligibly small size, L_0, then Eq. 3.3 reduces to

$$\frac{\partial(fV)}{\partial t} + V\frac{\partial(Gf)}{\partial L} = VB^\circ\delta(L - L_0) - \sum_k Q_k f_k \tag{3.4}$$

in which G is the crystal growth rate, B° is the nucleation rate density, and $\delta(L - L_0)$ is the Dirac delta function acting at $L = L_0$. The functions $f_k(L)$ can be defined to include washout from a CSTR (mixed product removal) and size-dependent removal (classified product removal and fines destruction). As shown in Appendix B, Eq. 3.4 is equivalent to

$$\frac{\partial(fV)}{\partial t} + V\frac{\partial(Gf)}{\partial L} = -\sum_k Q_k f_k \tag{3.5}$$

with the boundary condition

$$f(L_0, t) = \frac{B^\circ}{G|_{L=L_0}} \tag{3.6}$$

3.1.2 Mass and Energy Balances

As illustrated by the constitutive relations given for G and B° in Section 3.1.3, growth and nucleation rates are functions of temperature and supersaturation

(a measure of the difference between concentration and saturation concentration). Therefore, mass and energy balances are required to complete the description of the crystallization process.

The solute mass balance in the continuous phase must account for flow of solute into and out of the system and mass transfer to the solid phase via formation and growth of crystals. As shown in Appendix B, if $L_0 = 0$, the mass balance can be written as,

$$\frac{d(\varepsilon CV)}{dt} = -\sum_k \varepsilon_k Q_k C_k - 3\rho_c k_v V \int_0^\infty f L^2 G dL \tag{3.7}$$

where C is the solute concentration in the continuous phase, and ρ_c and k_v are the crystal density and volumetric shape factor, respectively. The fraction of V that is solids-free (continuous phase) is represented by ε, which is equal to $1 - k_v\mu_3$; μ_3 is the 3^{rd} moment of the CSD.

In reactive crystallization, the supersaturation is generated by chemical reactions. To model such cases, the chemical reaction rates multiplied by appropriate stoichiometric coefficients are appended to the right hand sides of the species' mass balances. Expressions for the reaction rates in terms of species concentrations are also necessary. A vector of mass (or mole) balances are then used to describe the system. In order to simplify the discussion, the case of reactive crystallization is not presented explicitly here. However, the modifications required to handle this case are, in principle, straightforward. The major difficulty is coming up with appropriate reaction rate expressions.

The energy balance given below is derived as shown in Appendix B:

$$\rho V c_p \frac{dT}{dt} = \frac{d(PV)}{dt} - \sum_k Q_k H_k - \Delta H_c 3\rho_c k_v V \int_0^\infty f L^2 G dL - H_{\text{ext}} \tag{3.8}$$

T is the crystallizer temperature, c_p is the specific heat of the slurry, ρ is the slurry density, P is the system pressure (pressure effect term is usually neglected for cooling crystallization), ΔH_c is the heat of crystallization, H_k is the enthalpy of the k^{th} stream relative to T_0, and H_{ext} is the net external heat removal, incorporating effects of the cooling system, evaporation, physical mixing, and loss to surroundings.

Eqs. 3.5–3.8 can be used to describe evaporative or cooling crystallizers in a variety of configurations, including batch and continuous modes with size-dependent removal.

3.1.3 Constitutive Relations

The term "constitutive relation" refers to relations or equations that depend on the *constitution* of the chemical/physical system under consideration. In order

to complete the modelling of the crystallization process, constitutive relations are required for growth and nucleation, the two competing phenomena in the phase change from solution to solid phase. Growth and nucleation can occur only if the solute concentration exceeds its saturation value (i.e., the solution is supersaturated). However, there are many factors that affect formation and growth of crystals, including crystallizer hydrodynamics, temperature, and presence of suspended or dissolved impurities. A brief discussion is given below of some of the theories and models used to describe growth and nucleation. It should be noted that for use in model-based control systems, the validity of the chosen models should be examined over a range of operating conditions to ensure predictive capability.

Growth. At the microscopic level, solute molecules moving from the bulk solution adsorb on the crystal solid surface and are incorporated into the crystal lattice. A well-defined, smooth crystal face is planar and new solute molecules must migrate across the surface to find energetically favorable incorporation sites. Three such potential sites are shown in Figure 3.1. At site A, the molecule can make a bond with only one surface of the crystal; sites B, a step site, and C, a kink site, are more favorable sites for incorporation because they provide two and three surfaces, respectively, for bonding with the molecule. Surface adsorption, surface diffusion, and availability of thermodynamically favorable sites determine whether a solute molecule is incorporated into the crystal or returns to the bulk phase. The resulting mechanism of crystal growth is the flow of steps across the surface.

The origin of the steps on the surface was originally postulated as the result of collisions between solute molecules that had adsorbed onto the surface. These collisions allow the formation of a critical-sized two-dimensional nucleus on the surface. However, the predicted rate of step formation with this mechanism is smaller than the experimentally observed growth rates, especially at low supersaturation. Burton, Cabrera, and Frank (BCF) [21] overcame this deficiency by considering the step to be formed by a screw dislocation, a commonly observed crystal imperfection. The crystal continues to grow without the formation of new steps as solute is fed to the steps by surface diffusion flux governed by Fick's Law and is incorporated along the spiral. The simplest form of the BCF model predicts the macroscopic growth rate to have the form

$$G = k'_g \frac{S^2}{k_{\mathrm{BCF}}} \tanh\left(\frac{k_{\mathrm{BCF}}}{S}\right) \tag{3.9}$$

$$S = \frac{C - C_{\mathrm{sat}}}{C_{\mathrm{sat}}}$$

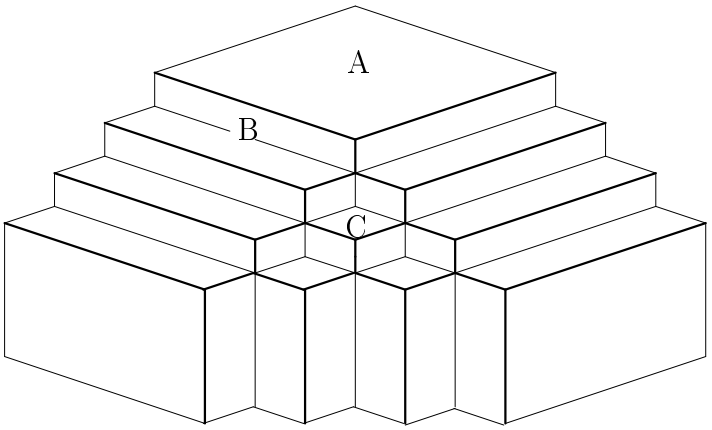

Figure 3.1: Crystal incorporation sites. Flat faces (A), step sites (B), and kink sites (C).

in which S is the relative supersaturation. If the surface diffusion and incorporation rates are fast enough, the mass transfer of solute molecules from the bulk to the surface also affects the macroscopic growth rate [94, 166]. Most of the chemical engineering literature treats this problem with an empirical mass transfer coefficient that must be correlated with the fluid dynamics and fluid properties. Other approaches include treating the diffusion through a stagnant film, or applying some form of boundary layer theory [54]. Garside [58] and Myerson and Ginde [108] provide thorough surveys and discussions of growth rate theories.

For engineering purposes, the empirical power law has become the standard representation of the growth rate,

$$G = k_g \exp(-E_g/T) S^g \tag{3.10}$$

Note that $g = 1$ and $g = 2$ are the high and low supersaturation asymptotes of the BCF model, respectively. Also notice that the temperature dependence has been incorporated using an Arrhenius-type expression.

Neither of the growth rate models given above indicate dependence of G on L. This size-independent growth rate assumption is usually referred to as McCabe's ΔL law. There are several examples of systems that violate McCabe's ΔL law; Canning and Randolph [22] give a discussion of such systems, and Budz et al. [18] give an expression for the size-dependent growth rate of potassium sulfate. Size-dependent growth rate is usually attributed to either bulk diffusion effects or the Gibbs-Thomson effect, which suggests an increasing growth rate with increasing size because of an inverse relationship between

solubility and size. Garside et al. [60] present a theory of size-dependent surface integration kinetics.

Modelling the growth rate is further complicated by a phenomenon known as growth rate dispersion. Growth rate dispersion describes the situation in which not all of the crystals grow at identical or constant rates even though the crystallizer conditions remain constant. As Girolami and Rousseau [63] demonstrate, many cases that have been thought to be occurrences of size-dependent growth are actually manifestations of growth rate dispersion. Recently, considerable attention has been focused on growth rate dispersion, and Zumstein and Rousseau [175] provide a review of these results. Two mechanisms have been put forward to explain deviations in the CSD due to growth rate dispersion. Randolph and White [126] assume that the crystals have the same time-averaged growth rate, but individual crystals experience stochastic fluctuations in the growth rate that cause the growth rate dispersion. Janse and deJong [83] and Berglund and Larson [7] postulate that each crystal has a constant, deterministic growth rate but that these growth rates differ from crystal to crystal; there has been some work that supports this hypothesis by relating mechanical stresses and strains of a crystal to its growth rate [57, 8]. Modifications to the population balance are available for either approach. As demonstrated by White and Wright [169], the spread of the seed population CSD during batch experiments is a good experimental test to determine whether growth rate dispersion is an important factor.

Nucleation. The nucleation of crystals from solution has been reviewed extensively [129, 152, 98, 55]. The complexity of mathematically modelling the formation of new crystals is largely due to the variety of mechanisms that are collectively termed "nucleation". Nucleation mechanisms are commonly lumped into one of two categories—primary or secondary nucleation—and can be further classified as shown in Figure 3.2.

Mechanisms of formation of crystals that are independent of the presence of other suspended crystals are classified as primary or spontaneous nucleation. Primary nucleation is associated with high levels of supersaturation and is usually partitioned as homogeneous nucleation, which occurs in the pure bulk solution, and heterogeneous nucleation, which is induced by foreign surfaces such as impurities.

Classical thermodynamic free energy minimization is used to derive the rate of homogeneous nucleation [167]. This theory postulates the production of embryos from the combination of solute molecules in a series of bimolecular reactions. The free energy of the embryos achieves a maximum at a critical size particular to the chemical system. Once an embryo exceeds this critical

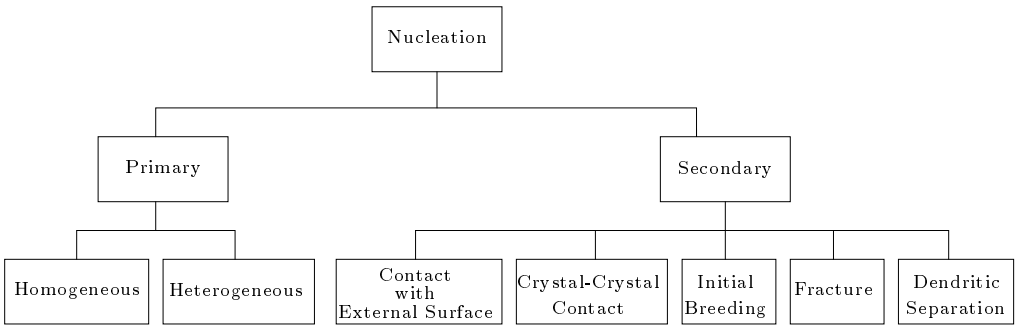

Figure 3.2: Nucleation Mechanisms

size, the free energy decreases with further growth, leading to spontaneous nucleation. The nucleation rate is then determined by the rate at which embryos cross the free energy maximum. Except in the case of precipitation crystallization, the very high supersaturation required to overcome interfacial tension between embryo and solution makes homogeneous nucleation an unlikely mechanism for crystal formation for most chemical systems under industrial conditions [167, 29].

Foreign surfaces and particles promote nucleation as a result of an ordering process caused by interactions across the interface [167]. The result of this catalysis is that primary, heterogeneous nucleation can occur at supersaturation levels significantly lower than required for homogeneous nucleation and is, therefore, the dominant mechanism of primary nucleation when impurities are present. Nevertheless, the supersaturation levels of heterogeneous nucleation are often still too high for good crystal growth and production of crystals of desirable morphology [29]. Also, classical theory suggests that primary, heterogeneous nucleation is characterized by a process that is either starved for nuclei or overwhelmed by a burst of new crystals [29], making CSD control difficult.

In addition to the issues of poor crystal quality and control difficulties associated with primary nucleation, attempts to predict and scale-up the primary nucleation rate have been largely unsuccessful. This is a result of the difficulty of accurately characterizing the low levels and types of impurities, and describing all the locations of high local supersaturation (i.e. near cooling coils or boiling surfaces).

Fortunately, secondary nucleation, which is more easily controlled than primary nucleation and occurs at supersaturation levels conducive to good crystal quality, always accompanies primary nucleation and is the dominant

mechanism in most industrial crystallizations [12, 66, 125]. Secondary nucleation describes the nucleation that takes place due to the presence of other solute crystals. There are a variety of proposed mechanisms whereby the crystals promote formation of new crystals. Botsaris [12] organizes this promotion around two questions: what are the sources of the potential nuclei, and how are the potential nuclei extracted from the source and displaced into the bulk solution to initiate new crystals. Proposed sources of potential nuclei include protrusions from growing crystal surfaces, solute clusters on or near the crystal surface, and embryos in the supersaturated solution. Several mechanisms for the conversion of "potential nuclei" into nuclei have been proposed; these include spontaneous removal of dendrites due to free energy driving force, fluid shear, and contact nucleation (contact of crystals with an external surface or other crystals) [12, 29, 85, 152].

The variety and complexity of the mechanisms of secondary nucleation have frustrated attempts to use theory for quantitative prediction. Therefore the modelling of nucleation is usually simplified by assuming an empirical functional form. The following expression is commonly used to described secondary nucleation

$$B^\circ = k_b \exp(-E_b/T) S^b \mu_k^j \tag{3.11}$$

in which k_b, b, E_b, and j are considered to be empirical constants, μ_k is the k^{th} moment of the CSD, and S is the relative supersaturation. The mechanistic effect of temperature on B° is complicated and, as Garside and Shah [61] show with a summary of several kinetic studies, nucleation can actually decrease with temperature, which corresponds to a negative activation energy, E_g. A common hypothesis is that higher temperatures lead to increased growth rates, involving greater efficiency of molecular diffusion on and integration into crystal surfaces; thus, fewer potential nuclei are available for secondary nucleation [71]. Nevertheless, evidence suggests that b is independent of temperature [61] and an Arrhenius-type expression is probably adequate for characterizing temperature dependence.

While secondary nucleation rate is usually correlated with μ_3, the nature of the phenomenon suggests that the surface area, $k_a\ \mu_2$, would be a reasonable choice and has been used by some researchers [166]. In many cases, contact of crystals with external surfaces is the predominant initiator of secondary nucleation and a first-order dependence on μ_3 is expected; several studies validate this assumption [61]. On the other hand, Sherwin et al. [149] claim that in the presence of a large amount of crystals, the dependence of nucleation rate on supersaturation is very strong, while the dependence on crystal surface (or mass) is a small effect and can be ignored ($j = 0$). As shown in the summary of kinetic studies by Garside and Shah [61], $j = 0$ is commonly

used. Some researchers have even found the correlation between B° and μ_3 to be such that j is negative; Winter [171] surmises that this corresponds to occurrence of substantial agglomeration.

For scale-up purposes either the stirrer speed, power input, or tip speed are also included as factors in Eq. 3.11 [61, 146].

3.1.4 Model Parameters

As discussed above, k and j are often chosen using mechanistic considerations. Parameters such as the crystal's density and area and volume shape factors are considered known or available from independent experiments. The other parameters of power law or BCF constitutive relations for the nucleation and growth rates—b, g, k_b, k_g (or k_g' and k_{BCF} for the BCF relation), E_b, and E_g—need to be estimated using experimental data. Because the relations are basically empirical, the parameters should be estimated for the system of interest.

As discussed further in Chapter 4, a goal of experimental model validation is to assess the limitations of the nucleation and growth constitutive relations and determine their predictive capability outside of the narrow operating region in which they are identified.

3.1.5 Model for Batch Cooling Crystallizer

The methods for model identification and control discussed in subsequent chapters are easily extended to apply to evaporative crystallization, but the work is illustrated in terms of cooling crystallization. The population, mass, and energy balance equations for a jacketed batch cooling crystallizer without fines dissolution are:

$$\frac{\partial f}{\partial t} = -\frac{\partial (Gf)}{\partial L} \tag{3.12}$$

$$\frac{d\hat{C}}{dt} = -3\rho_c k_v h \int_0^\infty f L^2 G dL \tag{3.13}$$

$$\rho V c_p \frac{dT}{dt} = -3\Delta H_c \rho_c k_v V \int_0^\infty f L^2 G dL - U A_c (T - T_c) \tag{3.14}$$

where U is the jacket heat transfer coefficient, A_c is the heat transfer area, T_c is the cooling fluid temperature, $\hat{C}$ is the solute concentration on a per-mass-solvent basis, and h is a conversion factor equal to the volume of slurry per mass of solvent. These equations can be derived from Eqs. 3.5, 3.7, and 3.8 by assuming that P, V and ρ are constant and the cooling system is the only

mechanism for external heat loss/gain. The conversion of the basis for solute concentration is done to be consistent with convention for batch crystallizers.

In addition to concentration and temperature measurements, it is shown in Section 2.4.6 that a transmittance measurement can be made and can be modelled as

$$\text{transmittance} = \exp\left(-\frac{k_a}{2} l \int_0^\infty f L^2 dL\right) \tag{3.15}$$

where l is the path length of the instrument light through the sample.
The boundary condition and initial conditions are as follows,

$$f(L,t) = \frac{B^\circ}{G}, \qquad L = 0 \tag{3.16a}$$

$$f(L,t) = f_0(L), \qquad t = 0 \tag{3.16b}$$

$$\hat{C}(t) = \hat{C}_0, \qquad t = 0 \tag{3.16c}$$

$$T(t) = T_0, \qquad t = 0 \tag{3.16d}$$

Notice that L_0 is taken to be equal to zero (nucleation at negligible size).

The crystallizer temperature variations in the experiments to be discussed in subsequent chapters are small; from Section 3.1.3, reasonable choices for constitutive relations for this type of operation of a seeded crystallizer are

$$G = k_g \hat{S}^g \qquad B^\circ = k_b \hat{S}^b \hat{\mu}_3 \tag{3.17}$$

where $\hat{\mu}_3$ is the third moment of the distribution in units of cm^3/g solvent. As illustrated in the following section, the solution of this model is not restricted to cases of size-independent growth rate.

In this study, it is assumed that the seed distribution can be characterized by a second-order polynomial that is zero at the minimum and maximum seed sizes. With this assumption, the seed distribution is fully specified by the weight of the seeds and the endpoints of the seed distribution.

3.2 Model Solution

A crystallizer model consists of a coupled set of nonlinear integro-differential equations. The population balance itself is a partial differential equation (PDE). Terms involving integrals over the distribution appear in the mass and energy balances because the transfer of mass from the solution to the solid phase must be represented as a sum over the rates for each individual crystal.

Analytical solutions of these equations do not exist and the numerical methods to treat this class of equations are much less developed than the methods available for the algebraic and ordinary differential equations (ODEs) of more standard engineering problems. Nevertheless, a variety of numerical methods have been employed to solve specific models on a case-by-case basis, and these methods are review by Rawlings et al. [132].

In this study, the PDE of the population balance is reduced to a set of coupled ODEs. The resulting set of equations that can be solved using the differential-algebraic system solver DASSL [116]. Orthogonal collocation and the method of moments are the PDE reduction schemes used; these are discussed in this section. As indicated, none of the presently available methods produce an efficient and accurate solution for a broad class of models; therefore, the methods discussed subsequently are tailored to and illustrated for the model for the batch cooling crystallizer given in Section 3.1.5.

3.2.1 Orthogonal Collocation

Collocation is a method for solving differential equations and for reducing PDEs to ODEs. The procedure involves approximating the solution as a linear combination of basis functions and requiring that the approximation satisfies the differential equation at certain points—the collocation points. As shown by Villadsen and Michelsen [164], the method is very efficient if the basis functions are orthogonal polynomials and if the collocation points are the zeros of the polynomials.

Witkowski [173] discusses the use of orthogonal collocation to reduce the population balance equation to a set of ODEs for the case of size-independent growth rate. An extension of this method to the more general case of size-dependent growth rate is described below.

A given function, say $u(L,t)$, can be approximated in a particular dimension by a linear combination of Lagrange interpolation polynomials. For example,

$$u(L,t) \approx \sum_{j=1}^{n} u(L_j,t) l_j(L) \tag{3.18}$$

where $l_j(L)$ is the Lagrange interpolation polynomial of degree j, and $u(L_j,t)$ is the function evaluated at the point L_j. The approximation of the derivative with respect to L is then

$$\frac{\partial u}{\partial L} \approx \sum_{j=1}^{n} u(L_j,t) \frac{dl_j(L)}{dL} \tag{3.19}$$

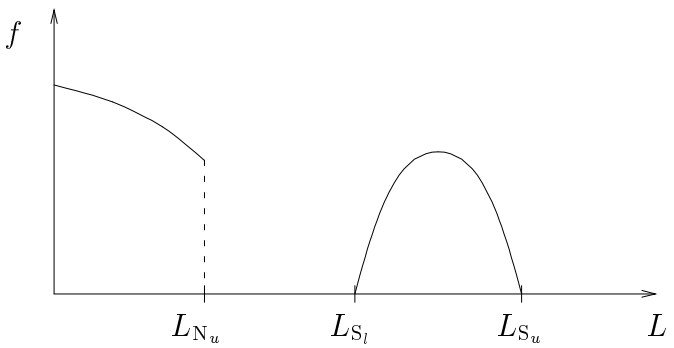

Figure 3.3: Depiction of the two subpopulations of the CSD—the nucleated crystals and the seed crystals.

Therefore

$$\left.\frac{\partial u}{\partial L}\right|_{L=L_i} \approx \sum_{j=1}^{n} A_{ij} u(L_j, t) \tag{3.20}$$

where A_{ij} is an element of the derivative weight matrix—A_{ij} equals $(dl_j/dL)|_{L_i}$. Orthogonal collocation with Lagrange interpolation polynomials is based on Eqs. 3.18–3.20; these will be referred to subsequently as the collocation equations.

If the integral of u over Ω_L is desired, its approximate value can be efficiently computed from quadrature:

$$\int_{\Omega_L} u \, dL \approx \sum_{j=1}^{n} w_i u(L_j, t) \tag{3.21}$$

where w_i is the i^{th} quadrature weight.

Because Villadsen and Michelson provide routines for computing the collocation points, quadrature points, and the weights for the domain [0,1], it is convenient to transform the domain of a problem to [0,1].

The CSD of a seeded crystallizer is bimodal by nature—one mode corresponding to the nucleated crystals and one corresponding to the seed crystals. As pointed out by Witkowski [173], when breakage and agglomeration are neglected it is advantageous to partition the crystal size domain into two finite elements—one for the CSD for nucleated crystals, $f_{\text{N}}(t, L)$, and one for the CSD for seed crystals, $f_{\text{S}}(t, L)$. The two subpopulations are depicted in Figure 3.3.

Nucleated Crystals. The domain of the nucleated crystals is bounded below by $L = 0$ (assuming nuclei have negligible size) and above by $L = L_{\mathrm{N}_u}$. The nucleated crystal element is stretched as the upper bound moves out at a rate equal to the growth rate:

$$\frac{dL_{\mathrm{N}_u}}{dt} = G(L_{\mathrm{N}_u}, t) \tag{3.22a}$$

$$L_{\mathrm{N}_u}(t) = 0, \qquad t = 0 \tag{3.22b}$$

The transformation to map the domain of the nucleated crystals to [0,1] is

$$\zeta_{\mathrm{N}} = \frac{L}{L_{\mathrm{N}_u}} \tag{3.23}$$

Note that

$$\left.\frac{\partial \zeta_{\mathrm{N}}}{\partial t}\right|_L = -\frac{L}{L_{\mathrm{N}_u}^2}\frac{\partial L_{\mathrm{N}_u}}{\partial t} = -\frac{\zeta_{\mathrm{N}}}{L_{\mathrm{N}_u}} G(L_{\mathrm{N}_u}, t) \tag{3.24}$$

Letting $\bar{G}$ represent the transformed growth rate,

$$\left.\frac{\partial \zeta_{\mathrm{N}}}{\partial t}\right|_L = -\frac{\zeta_{\mathrm{N}} \bar{G}(1,t)}{L_{\mathrm{N}_u}} \tag{3.25}$$

It is then straightforward to show that

$$\left.\frac{\partial f_{\mathrm{N}}}{\partial t}\right|_L = -\left(\frac{\zeta_{\mathrm{N}} \bar{G}(1,t)}{L_{\mathrm{N}_u}}\right)\frac{\partial \bar{f}_{\mathrm{N}}}{\partial \zeta_{\mathrm{N}}} + \frac{\partial \bar{f}_{\mathrm{N}}}{\partial t} \tag{3.26}$$

$$\left.\frac{\partial (G f_{\mathrm{N}})}{\partial L}\right|_t = \left(\frac{\bar{f}_{\mathrm{N}}}{L_{\mathrm{N}_u}}\right)\frac{\partial \bar{G}}{\partial \zeta_{\mathrm{N}}} + \left(\frac{\bar{G}}{L_{\mathrm{N}_u}}\right)\frac{\partial \bar{f}_{\mathrm{N}}}{\partial \zeta_{\mathrm{N}}} \tag{3.27}$$

where $\bar{f}_{\mathrm{N}}$ represents the transformed CSD. Note that since the functional dependence of G on L is presumably known, $\partial \bar{G}/\partial \zeta_{\mathrm{N}}$ can be evaluated.

Substituting Eqs. 3.26 and 3.27 into Eq. 3.12, the transformed population balance for the nucleated crystals is

$$\frac{\partial \bar{f}_{\mathrm{N}}}{\partial t} + \left(\frac{\bar{G} - \zeta_{\mathrm{N}} \bar{G}(1,t)}{L_{\mathrm{N}_u}}\right)\frac{\partial \bar{f}_{\mathrm{N}}}{\partial \zeta_{\mathrm{N}}} + \left(\frac{\bar{f}_{\mathrm{N}}}{L_{\mathrm{N}_u}}\right)\frac{\partial \bar{G}}{\partial \zeta_{\mathrm{N}}} = 0 \tag{3.28}$$

Applying the collocation equations to Eq. 3.28,

$$\frac{d\bar{f}_{\mathrm{N}_i}}{dt} = -\left(\frac{\bar{G}_i - \zeta_{\mathrm{N}_i}\bar{G}_{n_N}}{L_{\mathrm{N}_u}}\right)\sum_{j=1}^{n_{\mathrm{N}}} A_{ij}\bar{f}_{\mathrm{N}_j} - \left(\frac{\bar{f}_{\mathrm{N}_i}}{L_{\mathrm{N}_u}}\right)\left.\frac{\partial \bar{G}}{\partial \zeta_{\mathrm{N}}}\right|_{\zeta_{\mathrm{N}_i}} \qquad i = 2, 3, ..., n_{\mathrm{N}} \tag{3.29}$$

where $\bar{f}_{\mathrm{N}_i} \equiv \bar{f}_{\mathrm{N}}(\zeta_{\mathrm{N}_i}, t)$, $\bar{G}_i \equiv \bar{G}(\zeta_{\mathrm{N}_i}, t)$, n_{N} is the number of collocation points for the nucleated crystal element, and $\zeta_{\mathrm{N}_{n_N}} = 1$. The initial conditions are

$$\bar{f}_{N_i}\big|_{t=0} = \frac{B^\circ(0)}{\bar{G}(0,0)} \qquad i = 1, 2, ..., n_{\mathrm{N}} \tag{3.30}$$

The boundary condition is imposed via the algebraic relation

$$\bar{f}_{N_1} = \frac{B^\circ(t)}{\bar{G}(0,t)} \tag{3.31}$$

Seed Crystals. As illustrated in Figure 3.3, the domain of the seed subpopulation is $[L_{\mathrm{S}_l}, L_{\mathrm{S}_u}]$. The transformation variable for mapping this to [0,1] is

$$\zeta_{\mathrm{S}} = \frac{L - L_{\mathrm{S}_l}}{L_{\mathrm{S}_u} - L_{\mathrm{S}_l}} \tag{3.32}$$

The initial values of L_{S_l} and L_{S_u} are presumably known, and they move according to

$$\frac{dL_{\mathrm{S}_l}}{dt} = G(L_{\mathrm{S}_l}, t) \qquad \frac{dL_{\mathrm{S}_u}}{dt} = G(L_{\mathrm{S}_u}, t) \tag{3.33}$$

It can be shown that

$$\left.\frac{\partial \zeta_{\mathrm{S}}}{\partial t}\right|_L = -\frac{\zeta_{\mathrm{N}} \Delta G - G_l}{\Delta L} \tag{3.34}$$

where

$$\begin{aligned} \Delta L &= L_{\mathrm{S}_u} - L_{\mathrm{S}_l} \qquad & \Delta G &= G_u - G_l \\ G_l &\equiv G(L_{\mathrm{S}_l}, t) \qquad & G_u &\equiv G(L_{\mathrm{S}_u}, t) \end{aligned}$$

Proceeding as for the nucleated crystal subpopulation, the transformed population balance for the seed crystals is

$$\frac{\partial f_{\mathrm{S}}}{\partial t} + \left(\frac{-\zeta_{\mathrm{S}} \Delta \bar{G} - \bar{G}_l + \bar{G}}{\Delta L}\right) \frac{\partial \bar{f}_{\mathrm{S}}}{\partial \zeta_{\mathrm{S}}} + \left(\frac{\bar{f}_{\mathrm{S}}}{\Delta L}\right) \frac{\partial \bar{G}}{\partial \zeta_{\mathrm{S}}} = 0 \tag{3.35}$$

Collocation then gives

$$\frac{d\bar{f}_{\mathrm{S}_i}}{dt} = \left(\frac{\zeta_{\mathrm{S}} \Delta \bar{G} + \bar{G}_l - \bar{G}_i}{\Delta L}\right) \sum_{j=1}^{n_{\mathrm{S}}} A_{ij} \bar{f}_{S_j} - \left(\frac{\bar{f}_{\mathrm{S}_i}}{\Delta L}\right) \left.\frac{\partial \bar{G}}{\partial \zeta_{\mathrm{S}}}\right|_{\zeta_{\mathrm{S}_i}} \qquad i = 1, 2, ..., n_{\mathrm{S}} \tag{3.36}$$

where $\bar{f}_{\mathrm{S}}$ is the transformed seed CSD, $\bar{f}_{\mathrm{S}_i} \equiv \bar{f}_{\mathrm{S}}(\zeta_{\mathrm{S}_i}, t)$, $\bar{G}_i \equiv \bar{G}(\zeta_{\mathrm{S}_i}, t)$, and n_{S} is the number of collocation points for the seed crystal element. The initial conditions are obtained from the original seed distribution, f_{S_0}, as shown below:

$$\bar{f}_{\mathrm{S}_i}\big|_{t=0} = f_{\mathrm{S}_0}(L_{\mathrm{S}_l} + \Delta L \zeta_{\mathrm{S}_i}) \tag{3.37}$$

parameter	value	units
k_g	1.5×10^3	μm/min
g	1.5	dimensionless
k_b	2.11×10^6	g solvent/(cm^3 min)
b	2.25	dimensionless
C_0	0.5733	g solute/g solvent

Table 3.1: Kinetic parameters for model.

Summary and Illustration of Solution Technique. Orthogonal collocation provides a means to reduce the population balance equation to a set of $n_N + n_S - 1$ ODEs (Eqs. 3.29 and Eqs. 3.36) with initial conditions specified by Eqs. 3.30 and 3.37, and an algebraic equation (Eq. 3.31). These equations, along with the mass and energy balances and the equation for transmittance, can be solved by DASSL. In this study, the integral terms in the mass balance, energy balance, and transmittance equations are evaluated using the quadrature weights at the collocation points.

To illustrate this solution technique, simulations were performed for a hypothetical chemical system—a system for which the choice of kinetic parameters was arbitrary. The kinetic parameters are given in Table 3.1 and the physical properties are those given in Appendix C. The solvent and seed charges were taken to be 1650 grams and 4.8 grams, respectively. A temperature profile of constant-rate cooling from 35°C to 30°C was imposed.

One of the results of the solution is the time evolution of the CSD, as shown in Figure 3.4. The resulting concentration and transmittance profiles are given in Figure 3.5.

The results given in Figures 3.4 and 3.5 are for size-independent growth rate. In this case, the seed distribution does not change shape; it simply moves out along the L axis at a rate equal to G. The use of this fact make the solution much more efficient, because the differential equations for the seed subpopulation can be disregarded. This is the approach used by Witkowski [173].

The solution technique given above is applicable to cases of size-dependent growth rate. Consider the case in which large crystals grow at a faster rate than small crystals, and assume that this size dependence is characterized by

$$G = k_g S^g (1 + L)^{0.3} \tag{3.38}$$

This is of the form of the empirical model suggested by Abegg et al. [1] to describe growth rate size dependency. The CSD-time surface corresponding

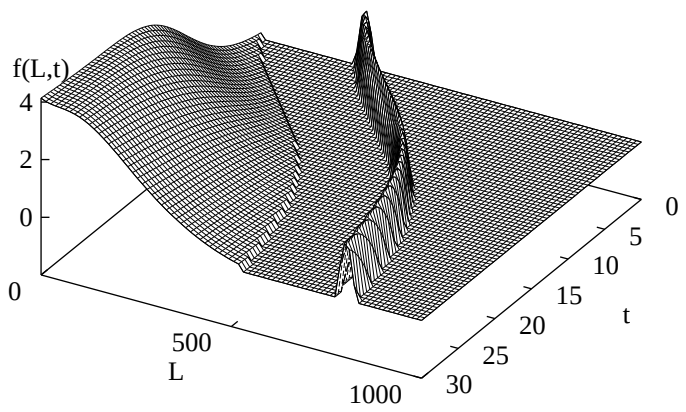

Figure 3.4: Evolution of CSD for case with size-independent growth rate.

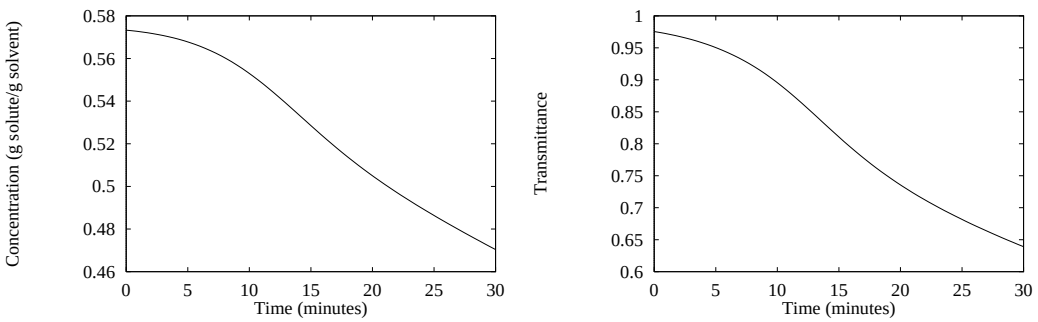

Figure 3.5: Concentration and transmittance for case with size-independent growth rate.

to this size-dependent growth rate is given in Figure 3.6. To demonstrate the dispersion over time inherent to a such size-dependent growth rate, the initial and final-time seed distributions are also given. While the seed distribution spreads, its integral over L is constant (in the absence of agglomeration and breakage, the number of seed crystals is constant). The corresponding concentration and transmittance profiles are given in Figure 3.7.

It should be noted that the orthogonal collocation solution technique discussed above does have limitations. It assumes that the solution can be represented by a (hopefully low-order) polynomial, and it is possible that this is not the case. For example, consider the case in which there is an initial jump in the supersaturation to a value that is then held constant. For size-independent growth rate, the resulting nucleated crystal subpopulation evolves to a distribution that is totally flat except for a sharp front at L_{N_u}. Clearly, such a function could not be represented accurately by a polynomial, and the result of the collocation solution would contain misleading oscillations. Such a problem could be handled by further partitioning of the size domain into more elements. Application of adaptive finite elements methods, methods that would probably provide the most efficient technique for this partitioning, is a currently active area of research. Reviews of adaptive methods in boundary value problems and integral equations are provided by Russell and Christiansen [144] and Delves and Mohamed [35], respectively.

3.2.2 Method of Moments

The method of moments is suggested by Randolph and Larson [129] and Hulburt and Katz [78] as a way to reduce the population balance to a set of ODEs. This method is based on averaging the population balance in the L direction by integrating it against L^j over the entire size domain. For example, the result for the population balance for the batch cooling crystallizer without fines dissolution is

$$\int_0^\infty L^j \frac{\partial f}{\partial t} + \int_0^\infty L^j \frac{\partial (Gf)}{\partial L} dL = 0 \tag{3.39}$$

Exchanging the order of integration and time differentiation, and assuming that growth rate is independent of size,

$$\frac{d\mu_j}{dt} + GL^j f\Big|_{L=0}^{L=\infty} - \int_0^\infty jL^{j-1} f dL = 0 \tag{3.40}$$

where μ_j is the j^{th} moment of the distribution: $\mu^j = \int_0^\infty L^j f dL$. With some nonrestrictive assumptions (f is finite at $L = 0$ and goes to zero as $L \to \infty$),

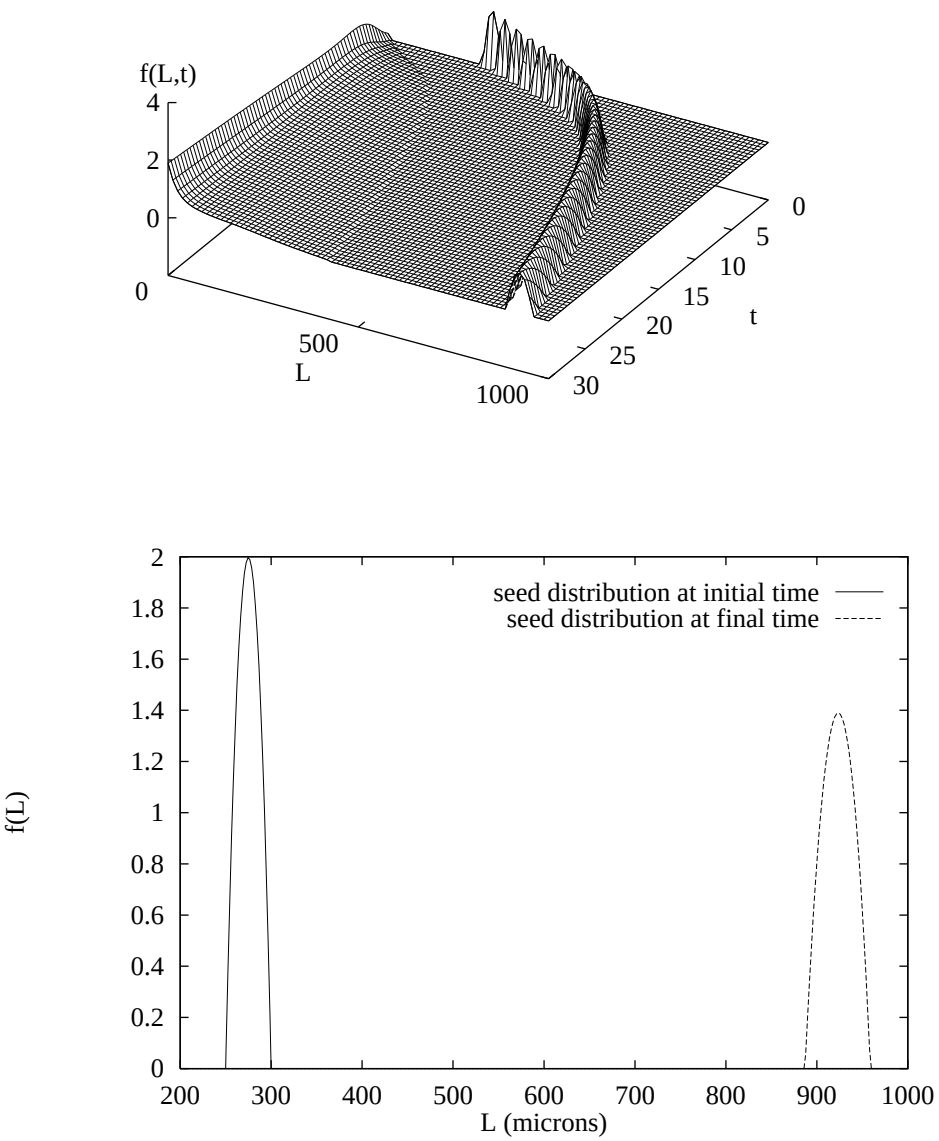

Figure 3.6: Evolution of CSD for case with size-dependent growth rate (above), and corresponding seed distributions at t_0 and at t_f (below).

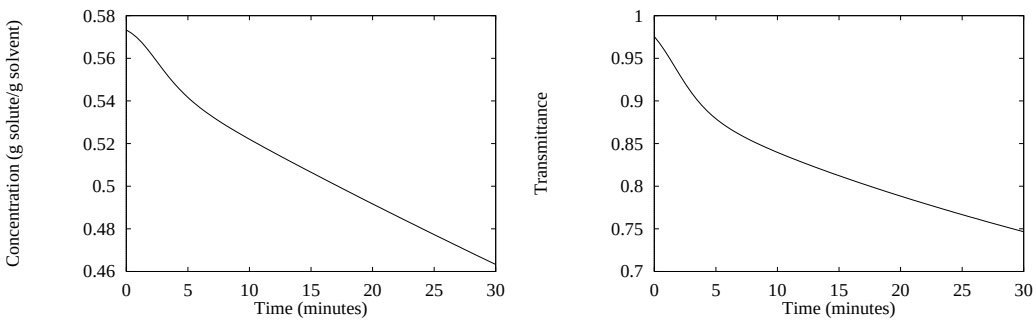

Figure 3.7: Concentration and transmittance for case with size-dependent growth rate.

and recalling that $f(0,t) = B^\circ/G$,

$$\frac{d\mu_0}{dt} = B^\circ \tag{3.41a}$$

$$\frac{d\mu_j}{dt} = jG\mu_{j-1} \qquad j = 1, 2, ... \tag{3.41b}$$

These moments are for the entire CSD. For the case of size-independent growth rate and negligible agglomeration and breakage, the moments of the seed subpopulation also can be obtained by noting that the seed distribution simply moves out in the L direction at a rate equal to G without changing shape. The j^{th} moment of the seed subpopulation at a given time is given by

$$\mu_{\mathrm{S}_j} = \int_{L_{\mathrm{S}_l}(0)}^{L_{\mathrm{S}_u}(0)} f_{\mathrm{S}_0}(Z,t)\ \ (Z + L_{\mathrm{N}_u})^j dZ \tag{3.42}$$

where $Z = L - L_{\mathrm{N}_u}(t)$. The j^{th} moment of the nucleated crystal subpopulation is, of course, equal to the difference between μ_j and μ_{S_j}.

Unlike the orthogonal collocation technique, the recovery of the CSD from the quantities resulting from this transformation (the moments) is usually very difficult. Nevertheless, this method is useful because, for the case of size-independent growth rate and no fines dissolution, the population balance is coupled with the mass balance, energy balance, and transmittance equation through the second moment. For the batch cooling crystallizer without fines dissolution and with size-independent growth rate, the mass and energy balances and transmittance equation can be written as:

$$\frac{d\hat{C}}{dt} = -3\rho_c k_v h G \mu_2 \tag{3.43a}$$

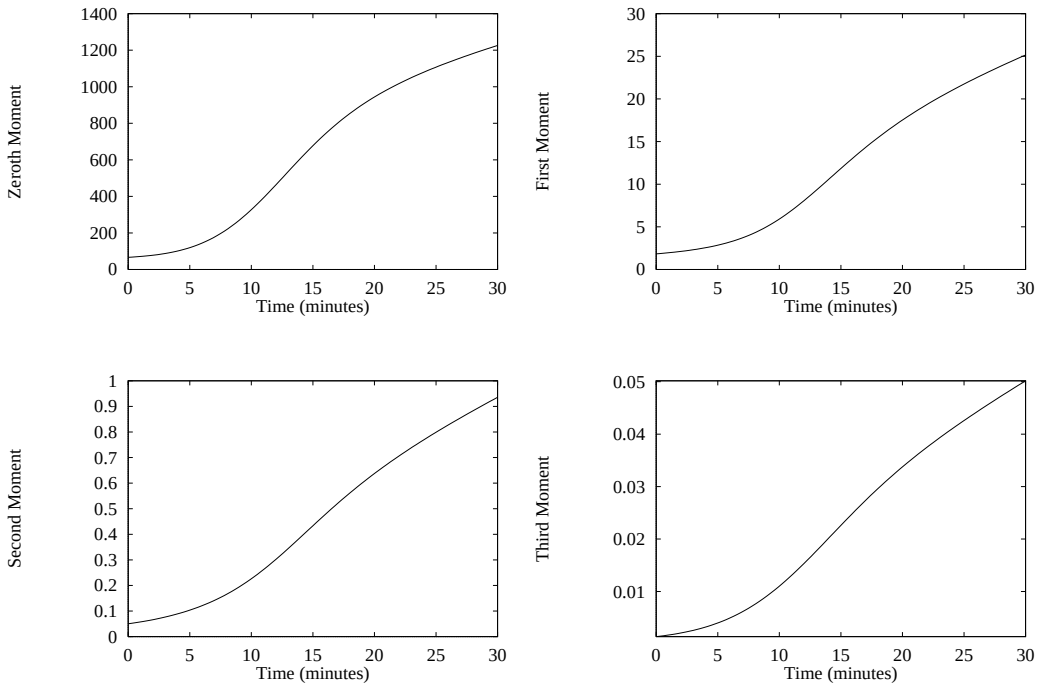

Figure 3.8: Time profiles of first four moments of the crystal size distribution (converted to a per-mass-solvent basis).

$$\rho V c_p \frac{dT}{dt} = -3\Delta H_c \rho_c k_v V G \mu_2 - U A_c (T - T_c) \tag{3.43b}$$

$$\frac{I}{I_0} = \exp\left(-\frac{k_a}{2} l \mu_2\right) \tag{3.43c}$$

As shown in Section 2.5, even the weight mean size and the coefficient of variation of the CSD can be obtained from the first five moments.

The solution of Eqs. 3.41 and 3.43 for the first four moments with the kinetic parameters in Table 3.1 and physical properties in Appendix C is shown in Figures 3.8 and 3.9. As in the previous example, a constant-rate cooling profile from 35°C to 30°C is imposed. As expected, the concentration and transmittance profiles shown in Figure 3.9 are exactly the same as those obtained from the orthogonal collocation approach (see Figure 3.5).

For the model for a crystallizer with size-independent growth rate and without fines destruction, the method of moments has an advantage over collocation in that it makes no assumption of the form of the solution (i.e., it

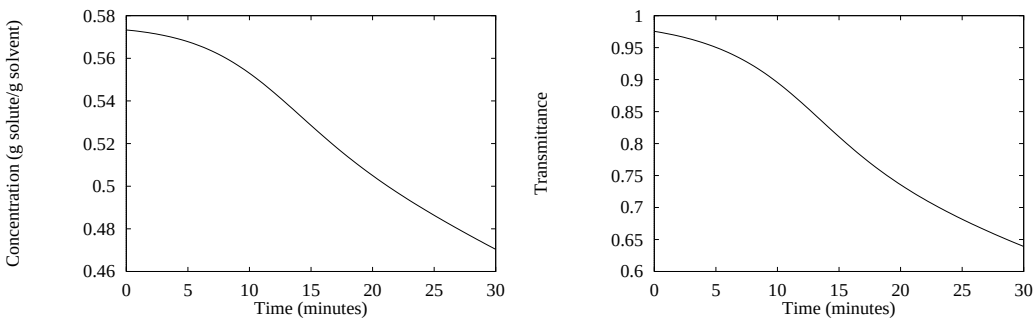

Figure 3.9: Concentration and transmittance from the method of moments.

does not assume that the solution can be represented with a low-order polynomial). Because solution via the method of moments allows evaluation of the variables that can be measured (transmittance, concentration, mean size and coefficient of variation), it is the primary solution technique used in this study. The orthogonal collocation technique described earlier should be used for cases in which the method of moments is not applicable, with the addition of adaptive finite elements if necessary.

Chapter 4

Parameter Estimation and Model Validation

In fact, no amount of data can ever prove a model; all we can hope is that it does not disprove it.

— Yonathan Bard

Model formulation—described in the previous chapter—is the first step in the twofold process of model identification. As explained in Section 3.1.4, complete specification of the model requires parameter estimation.

Figure 4.1 is an abstract depiction of the model-based prediction of the observations (or measurements). The composite operator $\mathcal{F} = \mathcal{H} \circ \mathcal{S}$ represents the mapping of the parameters into the model-predicted observation space, $\mathcal{Y}$. $\mathcal{F}$ depends on the model structure and solution technique.

For a given parameter set $\boldsymbol{\theta} \in \Theta$, a prediction of the system observations is given by

$$\mathbf{y} = \mathcal{F}(\boldsymbol{\theta})$$

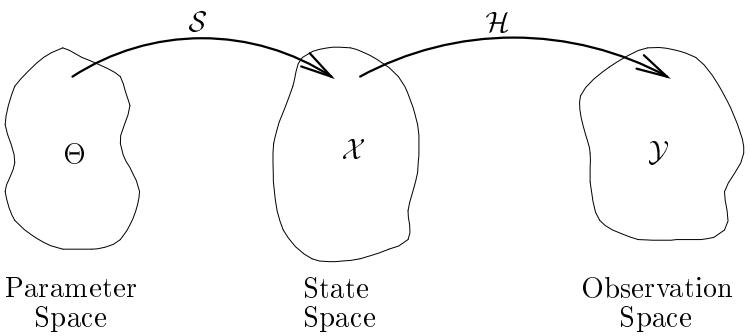

Figure 4.1: Abstraction of relationship between parameters and measurements.

Parameter estimation is simply the use of a given set of observations, $\mathbf{y} \in \mathcal{Y}$, in the inverse problem.

If every $\mathbf{y} \in \mathcal{Y}$ is the image of some element of Θ ($\mathcal{F}$ is surjective), then the parameter estimation problem has *a* solution. If, in addition, there is a one-to-one relationship between every $\mathbf{y}$ in the range of $\mathcal{F}$ ($\mathcal{F}$ is injective), then the solution is unique; in other words, $\mathcal{F}$ is invertible and the parameter estimation problem can be stated as

$$\boldsymbol{\theta} = \mathcal{F}^{-1}(\mathbf{y})$$

The only additional requirement for the problem to be well-posed is that the solution be stable, which is assured if $\mathcal{F}^{-1}$ is continuous.

The above discussion seemingly provides a succinct statement of the requirements for the unique solution of a parameter estimation problem; however, the following factors make the problem less straightforward:

- The requirements for a unique solution are difficult to check because, for the crystallizer problem, the parameter estimation operator, $\mathcal{F}^{-1}$, is nonlinear, and the measurements are corrupted with noise.

- The parameter estimation operator does depend on the model structure, which may be in error. In the case of model structure error, $\mathcal{F}^{-1}$ must implicitly project the actual observation space onto $\mathcal{Y}$.

The abstract statement of the crystallizer parameter estimation problem characterizes all parameter estimation from experimental data. All parameter estimation problems present hurdles that are common in the analysis and solution of inverse problems, but Seinfeld [147] highlights challenges that are peculiar to parameter estimation for distributed parameter systems:

- Parameters may be present only in the boundary conditions of the differential equations (note that this is true of the nucleation parameters).

- Measurements may be functions of space and time or represent integrated functions of the system states.

This chapter provides a review of the techniques that have been used for parameter estimation for crystallizers. A maximum likelihood method and a technique for determining parameter confidence regions are then presented. It is demonstrated that these techniques can be used to design experiments and determine reliable parameter estimates.

4.1 Parameter Estimation Methods

The most common method for simultaneously determining nucleation and growth kinetics involves operating a continuous mixed suspension, mixed product removal (MSMPR) crystallizer. There is one removal stream for a MSMPR, and its CSD is representative of the CSD in the crystallizer. The steady-state solution of Eq. 3.5 for this configuration and with the additional assumption that $G \neq G(L)$ is

$$f_{ss}(L) = \exp(-L/G_{ss}\tau)\frac{B^{\circ}_{ss}}{G_{ss}} \tag{4.1}$$

The plot of the logarithm of the CSD versus L should give a straight line,

$$\log(f_{ss}) = \log(B^{\circ}_{ss}/G_{ss}) - L/G_{ss}\tau \tag{4.2}$$

in which $\tau = V/Q$ is the crystallizer residence time, and f_{ss}, B°_{ss} and G_{ss} are the steady-state CSD, nucleation rate, and growth rate, respectively. The growth rate can be obtained from the slope of the semi-log plot, and the nucleation rate can then be calculated from the intercept.

For the common power-law kinetic expressions, the dependence of nucleation and growth rates on supersaturation can be determined by measuring the steady-state CSD at several different operating conditions and making log-log plots of G_{ss} and B°_{ss} versus S. This method of parameter estimation predominates the crystallization literature; Chen and Larson [26] provides a representative sample of papers describing application of the method. Timm and Larson [158] also use this method, but use the additional measurement of the slurry density to fix the intercept and determine B°_{ss}. Hartel et al. [70] use the measurement of the slurry density and the cumulative number density, the semilog plot of which should provide a straight-line relationship similar to that of Eq. 4.2, to determine G_{ss} and B°_{ss}.

Nývlt and Žáček [111] claim that the two most common sources of errors of the graphical, steady-state MSMPR method are uncertainties in the determination of the CSD from sieve data and the extrapolation of the CSD to $L = 0$. In other words, the data are always noisy and the intercept and, thus, the nucleation rate estimate are sensitive to this noise. They suggest that the use of cumulative weight distribution data will abate both of these difficulties. They show that an expression for the cumulative weight distribution can be obtained from Eq. 4.1; the term $G_{ss}\ \tau$ shows up as the only unknown in the cumulative weight distribution and can be estimated using nonlinear regression on sieve data. After obtaining $G_{ss}\ \tau$, B°_{ss} can be determined using a measurement of the slurry density in the following expression,

$$B^{\circ}_{ss} = \frac{M_T}{6\rho k_v \tau (G_{ss}\tau)^3} \tag{4.3}$$

where M_T is the slurry density. Zumstein and Rousseau [176] also use this method.

There are several disadvantages to determining kinetics with MSMPR experiments. First of all, the system must achieve steady state before the CSD is measured. This can be time-consuming, especially if one obtains sufficient data to ensure statistical confidence in the parameters [151], and it is often not feasible for producers of fine and specialty chemicals due to lack of sufficient material to run continuous experiments. Secondly it is sometimes difficult to achieve a true steady state. Crystallizers are often quite sensitive to small upsets and can actually be unstable and oscillate continuously.

Further problems are encountered with steady-state MSMPR experiments when the semi-log plot of the steady-state CSD is not a straight line. Significant upward curvature is often reported at the small crystal sizes. The upward curvature is a signal that the model structure is incorrect—the mixed product withdrawal assumption is not met, growth rate dispersion is occurring, and/or growth rate is size dependent. Jančić and Garside [81] and Hartel et al. [70] provide attempts to extend the MSMPR technique to cases of size-dependent growth rate.

As discussed in Section 4.3, the information content of the data of an experiment is an important consideration in parameter estimation. Another disadvantage of the steady-state MSMPR method is that it throws away any dynamic data. Timm and Larson [158] use transient responses to confirm kinetic characterization performed on steady-state MSMPR data of three different chemical systems and suggest the use of transient data for parameter estimation. Tavare [156] outlines attempts to use the dynamic CSD measurement from a MSMPR crystallizer in three simplified parameter estimation procedures. While the methods seemed successful when using simulated experimental observations, there was substantial scatter and disagreement between the different algorithms when actual data were used. After noting the sensitivity of the results to noise, Tavare suggests that MSMPR transient analysis may be used to confirm kinetics derived from steady-state analysis, but that additional work on experimental design would be needed for use in parameter estimation.

Parameter estimation based on transient batch crystallization is an attractive alternative to the MSMPR method. Tavare [157] summarizes the advantages of the batch crystallizer: a large number of operating variables can be studied in a relatively short time and a batch crystallizer can be successfully operated with a minimum development time and investment.

Garside et al. [59] and Palwe et al. [113] propose using transient solute concentration data from a batch experiment in an "initial derivatives" tech-

nique to determine growth parameters. After assuming a simple power law expression for G, the kinetic parameters are expressed in terms of the first and second derivatives of the supersaturation-time curve at zero time. The derivatives are obtained from a polynomial fit to the data. Tavare [155] extends this approach to non-isothermal crystallizers.

Without the assessment of parameter reliability, the parameter estimation problem is not complete. Uncertainty bounds are not reported in most of the crystallization parameter estimation studies, which casts doubt on the validity of the kinetic parameter values. Tavare [156] demonstrates that the scatter in parameter estimates using different estimation algorithms on the same set of data is significant, so it is not surprising that several different investigators have published quite different kinetic parameters for identical systems. Causes for this disagreement have been discussed by Jones [88], Qian et al. [119], Nývlt and Broul [110], Budz [19], Jančić and Garside [81], and Timm and Larson [158]. Section 4.2 demonstrates how uncertainties for typical crystallization kinetic studies can be large enough to account for much of the disagreement in previous studies. As shown in Section 4.3, this problem can be overcome by carefully designing the experiments.

4.1.1 Parameter Estimation Posed as an Optimization Problem

As Biegler et al. [10] demonstrate in a case study of a chemical reactor, nonlinear parameter estimation problems are challenging, but optimization schemes provide an intuitive approach to their solution. However, the use of optimization to estimate crystallizer parameters is not a guaranteed path to success.

Palwe et al. [113] report that convergence is difficult to achieve for straightforward parameter estimation with a rigorous optimization of the sum of the squared errors between predicted and measured supersaturation. It is not clear from their discussion why this method fails. Winter [171] uses an optimization scheme with dynamic slurry density measurements from a batch crystallizer (obtained by analyzing the final product from runs that are replicates except for the batch duration time), but does not address the uncertainty in his optimal parameter values. While Qiu and Rasmuson [120] do not give a great deal of detail about their estimation technique, they successfully use an optimization routine with measurements of concentration and final CSD to estimate growth and nucleation parameters and confidence intervals. Qiu and Rasmuson show that results simulated using the estimated parameters allow predictions of weight mean sizes that agree with experimental data to within 25%.

This section describes how the crystallization kinetics of a system can be efficiently determined by casting the estimation problem as a nonlinear optimization problem. With careful selection of objective function and experimental design, the result is a method that is general and that does not require model simplification.

Rippin [139] demonstrates that the choice of the experimental configuration can strongly influence the information content of the data used to characterize a system, and he points out that it should be the first step in setting up a parameter estimation problem. Because of the dynamic nature of batch crystallization, much information about a system can be obtained from a single run and, as discussed previously, batch crystallization offers advantages of operating convenience over continuous crystallization. As will be demonstrated in Section 4.3, solid-phase information is very important in parameter estimation; batch crystallization has the additional advantage that, assuming the seed CSD is known, a measure of the solute concentration gives a measure of the 3^{rd} moment of the CSD. Therefore, a batch crystallizer is chosen to illustrate the optimization techniques for parameter estimation.

A summary of the model developed in Chapter 3 for the batch cooling crystallizer used in this study is given below:

$$\frac{\partial f}{\partial t} = -G\frac{\partial f}{\partial L} \tag{4.4}$$

$$\frac{d\hat{C}}{dt} = -3\rho_c k_v G h \int_0^\infty f L^2 dL \tag{4.5}$$

$$\rho V c_p \frac{dT}{dt} = -3\Delta H_c \rho_c k_v V G \int_0^\infty f L^2 dL - U A_c (T - T_c) \tag{4.6}$$

The boundary condition and initial conditions are as follows,

$$\begin{aligned} f(L,t) &= \frac{B^\circ}{G}, \qquad L = 0 \\ f(L,t) &= f_0(L), \qquad t = 0 \\ \hat{C}(t), &= \hat{C}_0, \qquad t = 0 \end{aligned} \tag{4.7}$$

The constitutive relations for operation in which the temperature variation is small are

$$G = k_g \hat{S}^g \qquad B^\circ = k_b \hat{S}^b \hat{\mu}_3 \tag{4.8}$$

Operating variables include the transient cooling profile and the initial conditions for the experiment—the initial concentration and the seed distribution. Possible measurements include $\hat{C}(t)$, the final CSD, and the dynamic CSD (or some function of the CSD, such as transmittance). Section 4.3 discusses the

consequences on the estimation results of the assignment of operating variables and the choice of measurements, but assume for the moment that these decisions have been made. One then chooses an objective function that measures how well the model solution with a given set of parameter values predicts the experimental data. The least squares objective function is a common choice because it is intuitive and does not involve explicit consideration of the error structure of the experimental data. As discussed by Witkowski et al. [174], weighted least squares allows the scaling of measurements that have different dimensions and weighting so that parameter estimates will be most influenced by the measurements felt to be most reliable; in this case, the objective function is

$$\Phi(\boldsymbol{\theta}) = \sum_{i=1}^{N_m} \sum_{j=1}^{N_d} \omega_i (y_{ij} - \tilde{y}_{ij}(\boldsymbol{\theta}))^2 \tag{4.9}$$

where $\tilde{y}_{ij}$ and y_{ij} denote the i^{th} model prediction and measurement, respectively, taken at the j^{th} sampling instant during the experiment, ω_i is the weighting assigned to the i^{th} measured variable, N_m is the number of measured variables (i.e., concentration, transmittance, etc.), N_d is the number of samples of each measured variable, and $\boldsymbol{\theta}^T = [k_g, k_b, b, g,]$ represents the unknown parameter vector.

While the weights of Eq. 4.9 can be chosen to incorporate the data error structure (e.g., letting ω_i equal the inverse of the variance of the i^{th} measurement), it would require replicate experiments to assess this statistical information. Therefore, other than accounting for scaling of the measurements, the weights are usually set somewhat arbitrarily. The maximum likelihood method, on the other hand, enables the estimation of weights for the data along with the estimation of the parameters.

If one assumes that the model structure is correct, then the deviations between the data and the model predictions are due to random (and possibly biased) errors in the measurements. The maximum likelihood method can be thought of as determining the parameters that maximize the probability that a given set of data could be obtained, considering the error structure of the measurements.

Consider the following additional assumptions about the error structure of the measurements:

- Independent variables are deterministic.
- Errors at the j^{th} sampling instant are normally distributed with zero mean (no bias) and are homoscedastic (variance of errors are independent of the magnitude of the measured variable).

- Errors at different sampling instants are uncorrelated.

With these assumptions, it can be shown that the maximum likelihood method is equivalent to the minimization of

$$\Phi(\boldsymbol{\theta}) = \frac{N_d}{2} \log \det(\mathbf{M}(\boldsymbol{\theta})) \tag{4.10}$$

where $M_{ab} = \sum_{j=1}^{N_d} e_{aj} e_{bj}$, and $e_{ij} = y_{ij} - \tilde{y}_{ij}$ [4]. The method also yields the following estimate for the measurement error covariance matrix:

$$\mathbf{V} \approx \tilde{\mathbf{V}} = \frac{1}{N_d} \mathbf{M}(\boldsymbol{\theta}^\star) \tag{4.11}$$

where $\boldsymbol{\theta}^\star$ is the set of optimal parameters.

With the additional assumption that the errors in the measured variables are independent (an assumption that was checked and verified for the measured variables used in this study), the maximum likelihood estimates are obtained from the minimization of

$$\Phi(\boldsymbol{\theta}) = \frac{N_d}{2} \sum_{i=1}^{N_m} \log \left(\sum_{j=1}^{N_d} e_{ij}^2(\boldsymbol{\theta}) \right) \tag{4.12}$$

The estimates of the elements of the diagonal covariance matrix are

$$\tilde{V}_{ii} = \tilde{\sigma}_i^2 = \frac{1}{N_d} \sum_{j=1}^{N_d} e_{ij}^2(\boldsymbol{\theta}^\star) \tag{4.13}$$

For cases in which the sampling rates of different measurements are not equal (e.g., instruments for concentration and transmission measurement sample at different rates), Eqs. 4.12 and 4.13 become

$$\Phi(\boldsymbol{\theta}) = \sum_{i=1}^{N_m} \frac{N_{d_i}}{2} \log \left(\sum_{j=1}^{N_{d_i}} e_{ij}^2(\boldsymbol{\theta}) \right) \tag{4.14}$$

$$\tilde{\sigma}_i^2 = \frac{1}{N_{d_i}} \sum_{j=1}^{N_{d_i}} e_{ij}^2(\boldsymbol{\theta}^\star) \tag{4.15}$$

Whether the objective function is chosen for weighted least squares or for maximum likelihood, the optimal parameter values are found by solving the nonlinear optimization problem,

$$\begin{aligned} \min_{\boldsymbol{\theta}} \quad & \Phi(\mathbf{y}(t), \tilde{\mathbf{y}}(t); \boldsymbol{\theta}) \\ \text{subject to} \quad & \text{Crystallizer Model} \end{aligned}$$

In this study, the successive quadratic programming code NPSOL [62] was used to solve this optimization problem.

4.2 Interpretation of Estimates

As discussed in the introduction to this chapter, the estimation process can be thought of as a nonlinear operator that transforms a data set into an estimate of the parameters. Due to the random errors of the measurements, the parameter estimates are also random variables with a probability distribution that depends on the nature of the estimator and on the distribution of the measurement errors; Bard [4] refers to the distribution of the estimates as the sampling distribution. The sampling distribution can be used to establish a region of confidence for the parameter estimates.

If many replicates of the experiment used to estimate the parameters were available, the sampling distribution could be rigorously characterized. Since replicate data from crystallization experiments are difficult to obtain, an alternative is to perform a Monte Carlo study in which simulated replicate data are derived by adding random errors to the original data set in accordance with the assumed measurement probability distribution.

As pointed out by Bard [4], systems for which the parameters are known are not common. Therefore, the sampling distribution does not provide a measure of the estimator bias. A Monte Carlo study in which the parameter estimates from the original set of data are taken as the true parameters provides an estimate of the bias. Nevertheless, as is the case for experimental replication, Monte Carlo studies are too time-consuming for many purposes, because the estimation process can be computationally intensive.

An approximation of the confidence region can be obtained by assuming that the model can be represented by linear functions in the vicinity of the estimate,

$$\tilde{\mathbf{y}}_j(\boldsymbol{\theta}) \approx \tilde{\mathbf{y}}_j(\boldsymbol{\theta}^\star) + \mathbf{B}_j(\boldsymbol{\theta} - \boldsymbol{\theta}^\star) \tag{4.16}$$

where $\tilde{\mathbf{y}}_j^T(\boldsymbol{\theta}) = [\tilde{y}_{1j}(\boldsymbol{\theta}), ..., \tilde{y}_{N_m j}(\boldsymbol{\theta})]^T$, and $\mathbf{B}_j$ is the $N_m \times N_p$ matrix (where N_p is the number of parameters) given below

$$\mathbf{B}_j = \left.\frac{\partial \tilde{\mathbf{y}}_j}{\partial \boldsymbol{\theta}}\right|_{\boldsymbol{\theta}=\boldsymbol{\theta}^\star}$$

These partial derivatives can be obtained by finite difference; however, since the model involves differential equations, they can be efficiently and accurately computed by integrating the sensitivity equations along with the model equations [23, 4].

With the linearized model and the assumption that the measurement errors are random and normally distributed, the estimates are normally distributed

and it can be shown that the quantity

$$(\boldsymbol{\theta} - \boldsymbol{\theta}^\star)^T \left(\sum_{j=1}^{N_d} \mathbf{B}_j^T \mathbf{V}^{-1} \mathbf{B}_j \right) (\boldsymbol{\theta} - \boldsymbol{\theta}^\star)$$

is distributed as χ^2 with N_p degrees of freedom [4]. $\mathbf{V}$ is the measurement error covariance matrix. Therefore, letting $\mathbf{V}_\theta^{-1} = \sum_{j=1}^{N_d} \mathbf{B}_j^T \mathbf{V}^{-1} \mathbf{B}_j$ ($\mathbf{V}_\theta$ is the parameter covariance matrix for the linearized problem),

$$\Pr\{(\boldsymbol{\theta} - \boldsymbol{\theta}^\star)^T \mathbf{V}_\theta^{-1} (\boldsymbol{\theta} - \boldsymbol{\theta}^\star) \leq \chi^2_{N_p}(\alpha)\} = 1 - \alpha \tag{4.17}$$

where $\Pr\{E\}$ denotes the probability of some event E. In other words, the approximate $100(1-\alpha)\%$ confidence region from the linearization method is the ellipsoidal region defined by

$$(\hat{\boldsymbol{\theta}} - \boldsymbol{\theta}^\star)^T \mathbf{V}_\theta^{-1} (\hat{\boldsymbol{\theta}} - \boldsymbol{\theta}^\star) = \chi^2_{N_p}(\alpha) \tag{4.18}$$

where $\hat{\boldsymbol{\theta}}$ represents the true parameter set. This region can be characterized by the eigenvectors and eigenvalues of $\mathbf{V}_\theta^{-1}$. The eigenvectors give the direction of the ellipsoid's axes, which have lengths that depend on the eigenvalues—the i^{th} semi-axis lies along the i^{th} eigenvector of $\mathbf{V}_\theta^{-1}$ and has length $\sqrt{\chi^2_{N_p}(\alpha)/\lambda_i}$, where λ_i is the i^{th} eigenvalue.

The shape and orientation of the ellipsoid indicate the degree of correlation between the parameters. As can be seen in Figure 4.2 from the elongated ellipse for a hypothetical 2-parameter problem, θ_1 and θ_2 may be varied individually by only ± 0.5; however, if they are adjusted simultaneously, they can be varied significantly and still be in the confidence region.

Note that for cases in which the sampling rates of different measurements are not equal,

$$\mathbf{V}_\theta^{-1} = \sum_{i=1}^{N_m} \sum_{j=1}^{N_{d_i}} \mathbf{B}_{ij}^T \mathbf{V}^{-1} \mathbf{B}_{ij}$$

where $\mathbf{B}_{ij}$ is the $1 \times N_p$ vector defined as

$$\mathbf{B}_{ij} = \left. \frac{\partial \tilde{y}_{ij}}{\partial \boldsymbol{\theta}} \right|_{\boldsymbol{\theta} = \boldsymbol{\theta}^\star}$$

The meaning of the report of a confidence region is usually not immediately clear for cases in which $N_p > 2$; therefore, confidence intervals—$\Pr\{\hat{\boldsymbol{\theta}} \in [\boldsymbol{\theta}^\star \pm \boldsymbol{\delta\theta}(\alpha)]\} = (1-\alpha)$—are often desired. Conservative estimates of these can be obtained by locating the box in the parameter space that circumscribes the ellipsoid (see Figure 4.2).

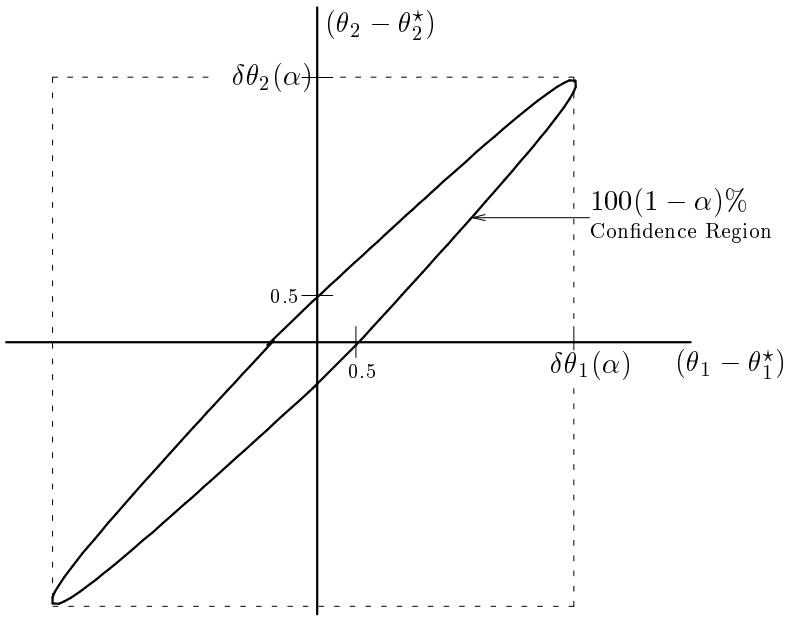

Figure 4.2: Confidence region demonstrating significant correlation between parameters. Conservative confidence interval for θ_i is defined by $\delta\theta_i$.

Bard [4] gives several other approximate techniques for obtaining approximate confidence regions and intervals, and Donaldson and Schnabel [40] give an extensive discussion of confidence regions for nonlinear least squares problems. As illustrated by several Monte Carlo studies [40, 3], approximate techniques can overestimate confidence regions, but there is no guarantee that the true confidence region will not be grossly underestimated. Nevertheless, the approximate technique outlined above does give a convenient method for assessing parameter uncertainty that at least gives qualitative information about how well-determined the parameters are.

4.3 Experimental Design

The goal of the experimental design can now be stated precisely. One wishes to choose operating conditions and measurements such that the correlation between parameters and the volume of the confidence region are minimized. As shown in the previous section, techniques for assessing parameter uncertainty is not global; the techniques use nominal values for the parameters. A related complication exists for the experimental design problem—a model-

based procedure requires the values of the parameters in order to minimize the parameter uncertainty. Whether the approach is trial-and-error or quantitative and model-based, experimental design is sequential in nature: collect data, estimate parameters and confidence region, design new experiments.

4.3.1 Measured Variables

Physical arguments provide some insight into the choice of measured variables. For example, intuition suggests that since the 3^{rd} moment is the only solid-phase information that can be derived from the concentration measurement, this measurement alone is probably insufficient for the independent determination of all of the kinetic parameters. Nevertheless, it is not obvious which measurements or sets of measurements contain sufficient information for successful parameter estimation.

In order to study this question, the data from bench-scale, potassium nitrate/water crystallization experiments were analyzed to assess the impact on parameter estimation of different measurement choices. Details of the experimental setup are given in Chapter 2. Concentration and transmittance measurements were made for a batch run with the temperature profile shown in Figure 4.3. Zero time corresponds to the time of the addition of seeds, which were added at approximately zero supersaturation (i.e., initial concentration is just above the saturation concentration).

The concentration and transmittance measurements are given in Figures 4.4 and 4.5, respectively. Since concentration is a common measurement choice in the literature previously reviewed, we first consider parameter estimation using this measurement alone.

Applying the techniques outlined in Sections 4.1.1 and 4.2 to the data shown in Figure 4.4 results in the optimal parameters and approximate uncertainties given in Table 4.1. The fit to the data of the model with these parameters is shown in Figure 4.6. As can be seen, while the model fit to the data is good there is significant parameter uncertainty, especially in the nucleation parameters. Many combinations of parameters in the large confidence region described in Table 4.1 have roughly the same ability to predict the observations. A physical explanation for this is that many different transient CSDs can take up the solute from the continuous phase to produce nearly identical $\hat{C}(t)$ curves. The concentration measurement does not contain sufficient information to determine the parameters uniquely. This result is the central point that is overlooked in much of the crystallization literature and is a possible explanation for the disagreement between various investigators' reported parameters. The practical significance is that crystallizer control based

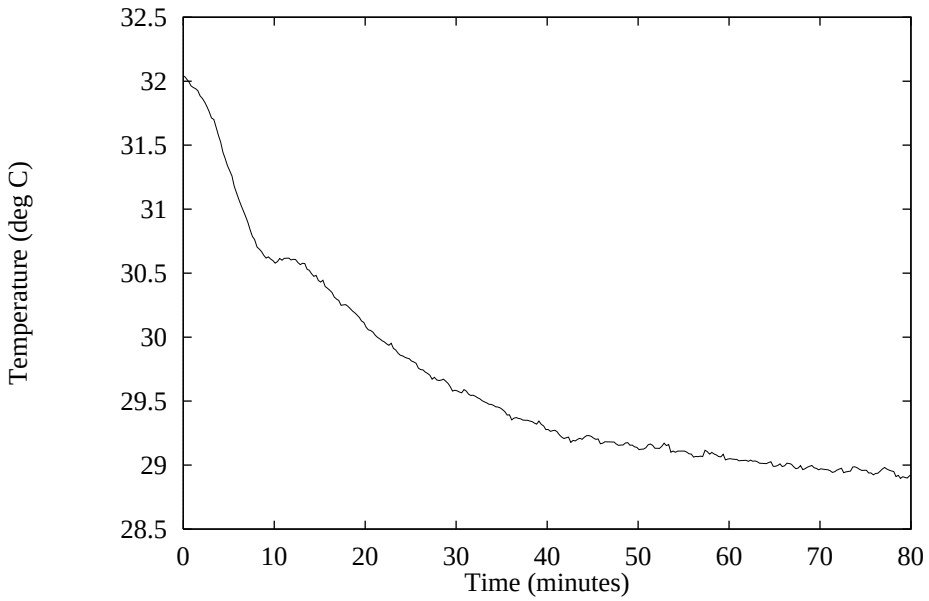

Figure 4.3: Temperature profile for batch crystallization of KNO_3 from water.

	$\ln(k_g)$	g	$\ln(k_b)$	b
Estimate	8.014	1.10	14.710	0.85
Interval	± 0.423	± 0.12	± 6.268	± 2.48

Table 4.1: Parameter estimates resulting from concentration measurements.

on the parameters identified using concentration measurements alone is not likely to achieve the product CSD that is desired.

The transmittance data and that predicted by the model using the parameters obtained using concentration data only is shown in Figure 4.7. Notice that the fit is not satisfactory.

As discussed in Section 2.4.6, there is a one-to-one relationship between transmittance and the 2^{nd} moment of the CSD. It is therefore reasonable to expect that the measurement of transmittance would provide independent in-

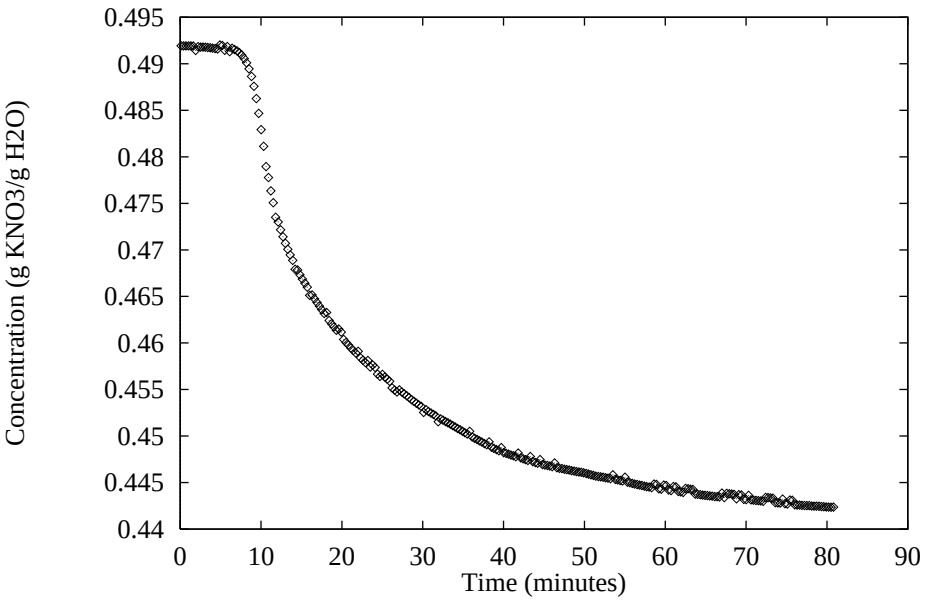

Figure 4.4: Concentration measurements from experiment with temperature profile given in Figure 4.3.

	$\ln(k_g)$	g	$\ln(k_b)$	b
Estimate	8.167	1.09	15.779	1.39
Interval	± 0.205	± 0.06	± 1.475	± 0.406

Table 4.2: Parameter estimates resulting from concentration and transmittance measurements.

formation for the estimation process. A comparison of Tables 4.1 and 4.2 demonstrates that the transmittance measurement is in fact effective in reducing parameter uncertainty.

The reduction in parameter uncertainty has important implications for process and controller design. For example, controller design would be difficult using the model with the parameter results in Table 4.1, because the sign of the nucleation order is not known with confidence. The controller would take control action without knowing with certainty whether increasing

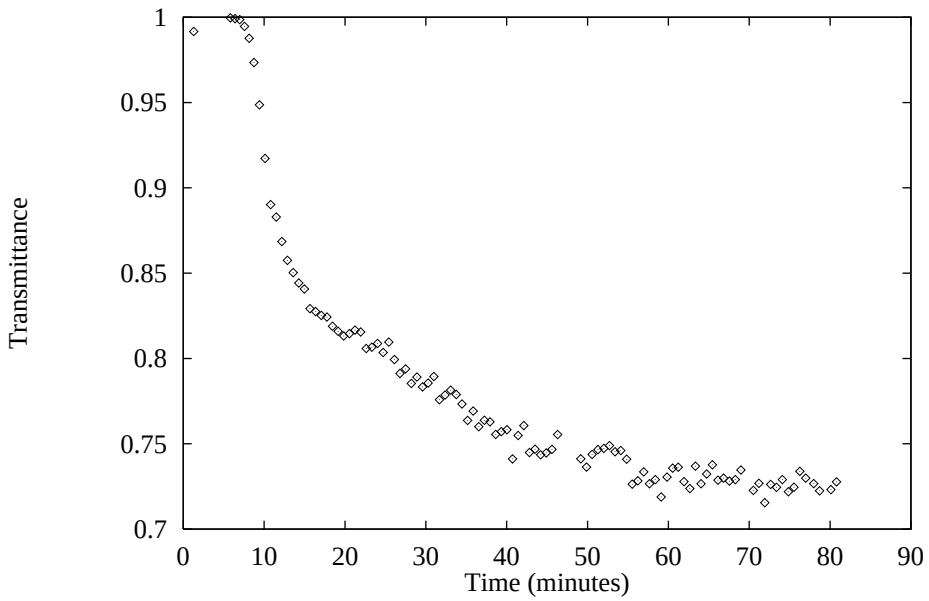

Figure 4.5: Transmittance measurements from experiment with temperature profile given in Figure 4.3.

supersaturation would increase or decrease the nucleation rate. This level of model uncertainty is a consequence of the poor experimental design used for identification. The decrease in parameter uncertainty attained by using the transmittance measurement would simplify the controller design problem. It would be a much simpler matter to detune a controller to be robust for the uncertainty shown in Table 4.2.

4.3.2 Operating Variables

The inspection of the kinetic expressions, Eq. 4.8, provides considerable insight for the choice of operating variables. For example, it is obvious that if one wishes to identify k_b and b independently, then the variation in the supersaturation should be made as large as possible during the course of the experiment. The justification is simply that if the supersaturation is constant during the experiment, one can only estimate the product, $k_b \hat{S}^b$. Similarly, if temperature dependence is being characterized, the temperature variation should be made as large as possible.

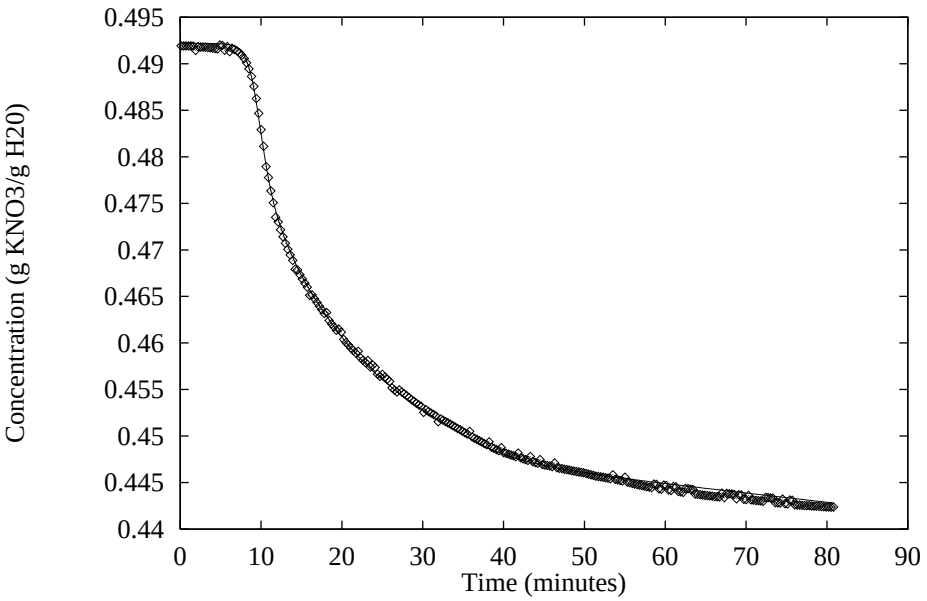

Figure 4.6: Fit to the data of the model with nominal parameters given in Table 4.1.

The parameter estimation results obtained in the previous section were based on a single batch experiment using a temperature profile with a rapid initial drop and a slow approach to the final temperature. It is possible that the choice of a different temperature profile would lead to improved parameter estimation (a smaller parameter confidence region). As discussed previously, the experimental design procedure for a nonlinear problem is sequential. With the results obtained above, simulations could be used to determine a temperature profile that would be expected to reduce the parameter uncertainty. The process is actually often trial-and-error—analysis is performed using data from experiments with new operating conditions that were selected using intuition. For example, intuition suggests that additional information could be obtained by performing an experiment that is a replicate of the one described above, with the exception of the use of gradual cooling like that shown in Figure 4.8 instead of the rapid cooling shown in Figure 4.3. The results from parameter estimation using concentration and transmittance data from *both* experiments are given in Table 4.3. The fit of the model to the data is given in Figures 4.9 and 4.10. As expected, the additional information contained in the data of the

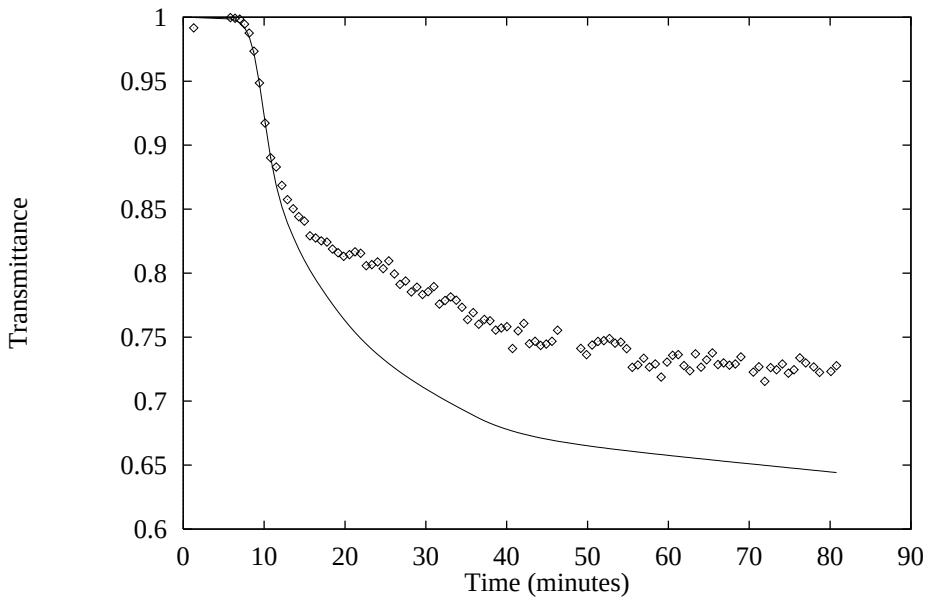

Figure 4.7: Transmittance data and prediction from model with nominal parameters given in Table 4.1.

.

	$\ln(k_g)$	g	$\ln(k_b)$	b
Estimate	8.918	1.32	17.207	1.78
Interval	± 0.127	± 0.03	± 0.356	± 0.09

Table 4.3: Parameter estimates resulting from concentration and transmittance measurements from two batch runs.

new experiment leads to a decrease in the parameter uncertainty. It should be noted that not all of the nominal parameters of Table 4.3 fall within the significantly larger confidence intervals given in Table 4.2. Although the interpretation of this could be that there is bias in the parameter estimates, it is likely that this disagreement is a manifestation of the nature of experimental design for nonlinear problems—the approximate confidence region obtained using poorly-determined parameters may be inadequate.

One of the assumptions for parameter estimation given in Section 4.1.1 is

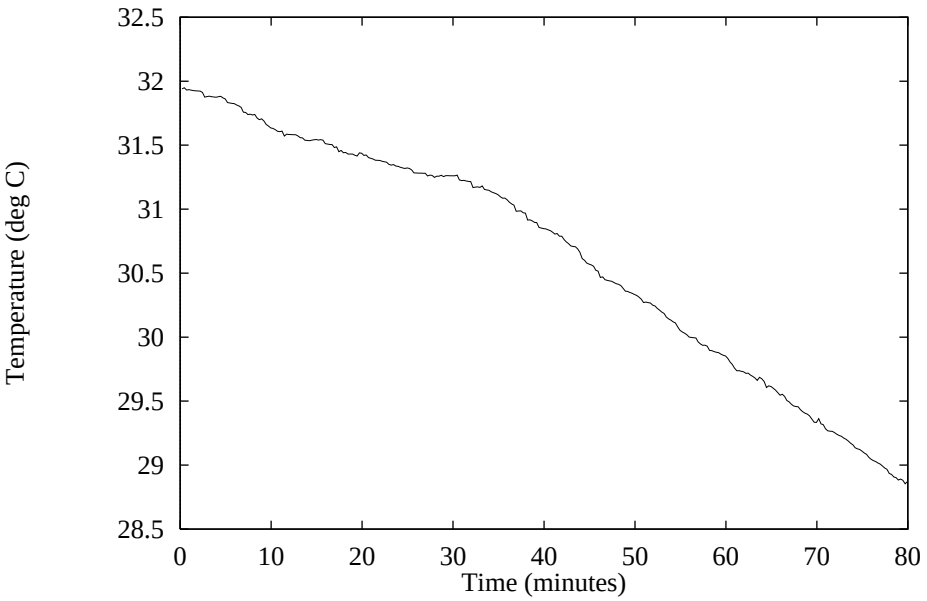

Figure 4.8: Gradual-cooling temperature profile for batch crystallization of KNO_3 from water.

that there is no autocorrelation (serial correlation) in the errors of each of the measurement types. Tests of this assumption for the i^{th} measurement type are usually based on the residuals, e_{ij}. The most common indicator of autocorrelation is referred to as the 1^{st} autocorrelation, which is the correlation between the series e_{ij} and the series of residuals shifted one step, $e_{i(j-1)}$. As shown in Figures 4.11 and 4.12, the residuals indicate significant autocorrelation. In fact, the 1^{st} autocorrelations for the concentration and transmittance measurements are 0.78 and 0.72, respectively. As explained by Brook and Arnold [14], high autocorrelations could suggest that the model neglects some physical effects, but the presence of high autocorrelations is not a basis for model rejection and does not mean that the estimated parameters are biased. Bard [4] points out that for models fitted to good data, non-randomness of residuals is the rule rather than the exception; this is because any neglected effects are prominent when the fit is very good.

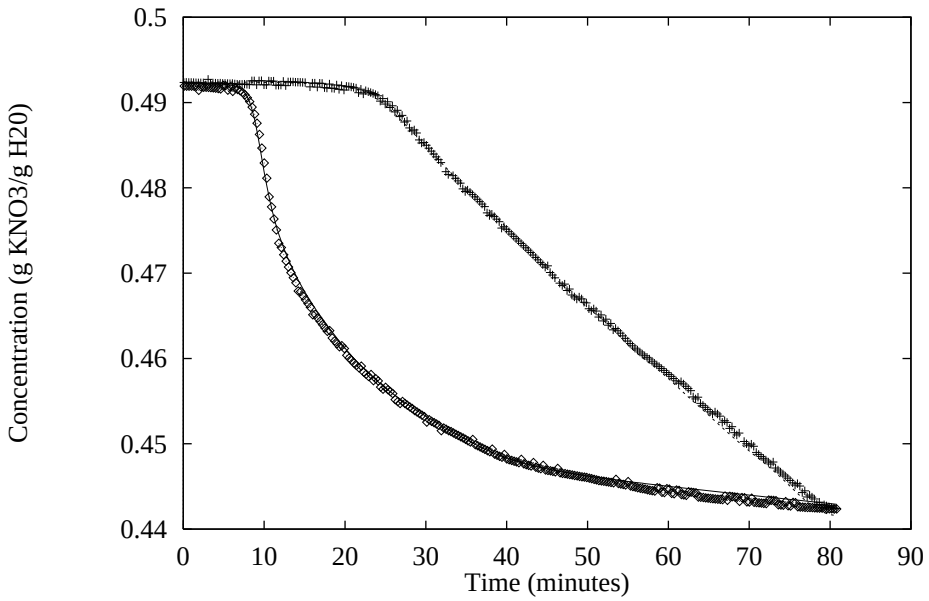

Figure 4.9: Fit to concentration data from two runs of model with nominal parameters given in Table 4.3.

4.3.3 Experimental Design Summary

Experimental design is the process of choosing the measurements and operating variables for experiments to be used in parameter estimation. A method, like that discussed in Section 4.2, to characterize the uncertainty of the parameter estimates is required to evaluate the effectiveness of the parameter estimation technique and the experimental design.

As pointed out in Section 4.2, the validity of the approximate parameter confidence region obtained by linearizing the model and using linear statistics is problem specific but can be tested using a Monte Carlo study. To do so, the following procedure was followed:

- Took the data shown in Figures 4.9 and 4.10 as the base data set.
- Constructed 500 "replicate runs" by adding error to the base data set according to pseudorandom numbers drawn from a normal distribution with zero mean and covariance $\mathbf{V}$—the assumed error structure. Parameter estimation corresponding to the minimization of Eq. 4.14 is based on a diagonal measurement error covariance matrix with $V_{ii} = \sigma_i^2 \approx \tilde{\sigma}_i^2$.

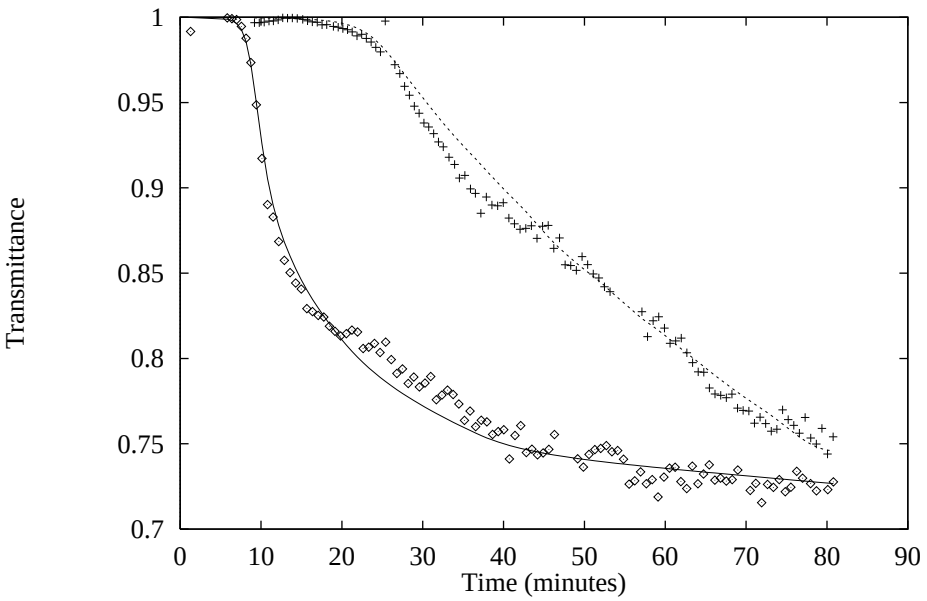

Figure 4.10: Fit to transmittance data from two runs of model with nominal parameters given in Table 4.3.

For this study, $i = 1$ corresponds to concentration measurements, and $i = 2$ corresponds to transmittance measurements. For the base-case parameter estimation, Eq. 4.15 gives $\tilde{\sigma}_1 = 0.0005$ and $\tilde{\sigma}_1 = 0.009$; these values were used to construct the Monte Carlo replicate data.

- For each Monte Carlo replicate data set, it was recorded whether or not the parameter estimates fall in the linear statistics confidence region defined by Eq. 4.18. This check was performed for various confidence levels (i.e., various values of α).

The results of this study are summarized in Table 4.4. This Monte Carlo study does not deal with the issue of the adequacy of the model structure or the validity of the error structure assumption; however, it does confirm that the elliptical confidence regions from linear statistics adequately characterize the parameter uncertainty for the system of this study.

Although it is not practical to perform enough experiments to allow construction of a confidence region, a replicate data set was obtained by repeating the two experiments used in the parameter estimation summarized in Ta-

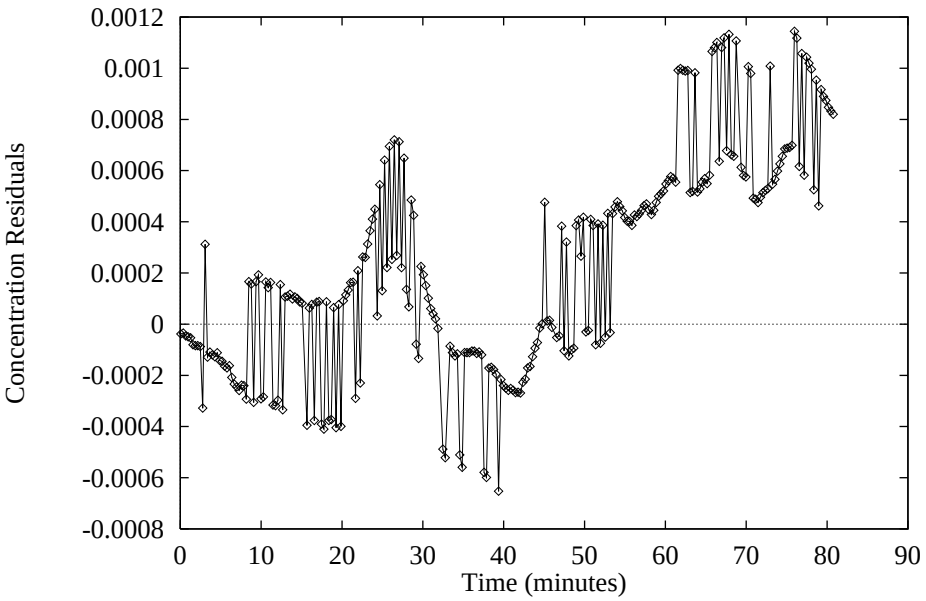

Figure 4.11: Residuals between concentration data and model predictions for one of the runs illustrated in Figure 4.9.

Linear statistics confidence level	Frequency that parameter estimates from replicate data are within the elliptical confidence region
50%	49%
70%	67%
80%	76%
90%	87%
95%	93%
98%	97%

Table 4.4: Comparison of linear statistics with Monte Carlo analysis of 500 replicate data sets.

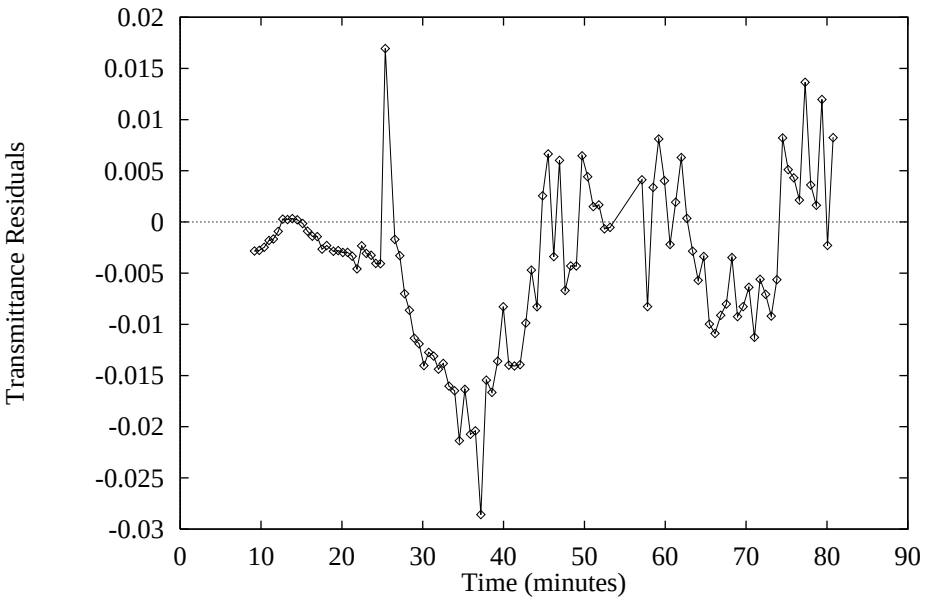

Figure 4.12: Residuals between transmittance data and model predictions for one of the runs illustrated in Figure 4.10.

	$\ln(k_g)$	g	$\ln(k_b)$	b
Estimate	8.817	1.32	16.766	1.69
Interval	± 0.147	± 0.04	± 0.602	± 0.15

Table 4.5: Parameter estimates resulting from replicate runs of those used to obtain Table 4.3.

ble 4.3. The parameter estimation results for the replicate data are given in Table 4.5. A comparison of Tables 4.3 and 4.5 demonstrates agreement between the results from the two data sets.

Table 4.6 gives the parameter estimation results obtained using data from all four runs. These parameters are used as the nominal parameters in subsequent discussion.

Tables 4.1 and 4.2 demonstrate that the addition of the solid-phase information provided by the transmittance measurement significantly reduces

	$\ln(k_g)$	g	$\ln(k_b)$	b
Estimate	8.849	1.32	17.142	1.78
Interval	± 0.112	± 0.03	± 0.360	± 0.09

Table 4.6: Parameter estimates resulting from concentration and transmittance measurements from four batch runs. Estimates taken as nominal parameters of KNO_3—H_2O system.

uncertainty in the parameter estimates for the KNO_3–H_2O system. As shown by a comparison of Tables 4.2 and 4.3, the addition of data from an experiment in which the temperature is gradually reduced to the data from an experiment in which the temperature is allowed to cool rapidly further decreases the parameter confidence region. The parameter estimates given in Tables 4.1, 4.2, 4.3, and 4.6 are consistent (with only a few exceptions, the confidence intervals for each parameter overlap), and the confidence regions are consistently reduced as more information is added.

The seed load used in the experiments discussed above was quite light. The rationale behind this was that experiments with light seed loading would be expected to yield more information about nucleation than experiments in which the solute is primarily deposited on the seeds. This initial condition is another operating variable that could be used to affect the quality of parameter estimation.

It should be noted that, depending upon the number of data sets used, the computation time required for the parameter estimation problems discussed in this chapter ranged from 3 to 18 minutes on a DECstation 5000/240.

4.4 Further Model Validation

As discussed by Denn [36], the objectives of the problem must be considered when determining the quality of a model. The model is of sufficient quality if it allows prediction of the variables of interest with desired accuracy. It has been established that, even over a wide range of operating conditions, the model identified for the KNO_3–H_2O system provides accurate and reproducible predictions of concentration and transmittance (see Figures 4.9 and 4.10).

As discussed in Chapter 2, sieve analysis yields qualitative information about a sample of crystals and, while subject to several sources of error, does

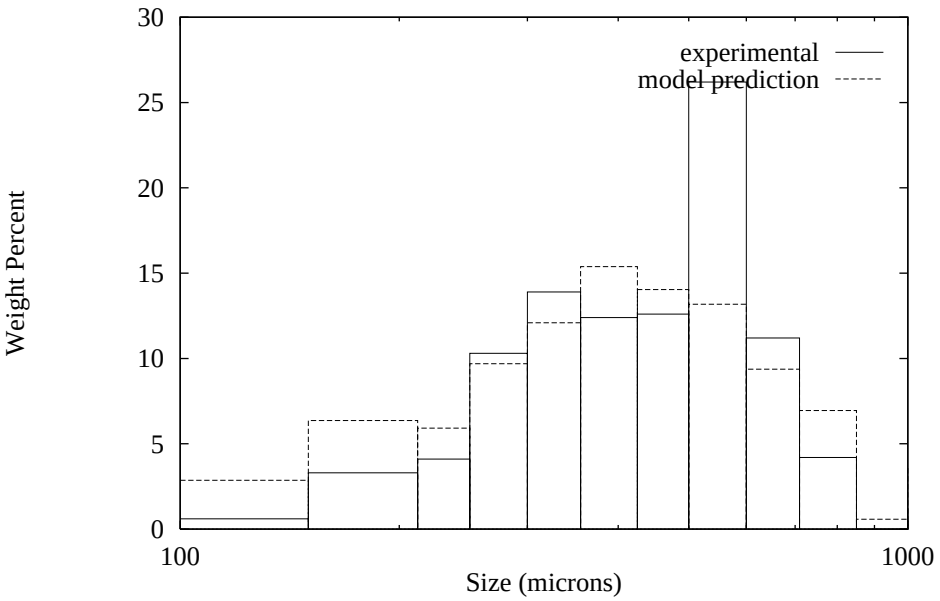

Figure 4.13: Comparison of sieve analysis results and the model prediction for a crystallizer product.

provide measurements of the weight mean size, L_{wm}, and the coefficient of variation, $c.v.$, of the CSD. For further model validation, sieve analysis was performed on the products of several crystallization runs and the results compared with model predictions. A comparison of sieve analysis measurements and model predictions of L_{wm} and $c.v.$ for several experiments is given in Chapter 5, but Figures 4.13 and 4.14 show the results from two sample runs.

Figure 4.13 gives the model prediction and the sieve analysis results for the product of a crystallization experiment. There is reasonable agreement between the experimental and model-predicted maximum crystal size and location of the primary mode of the distribution. The weight mean size and coefficient of variation also agree fairly well—experiment: $L_{wm} = 460$ μm, $c.v. = 0.36$; model prediction: $L_{wm} = 450$ μm, $c.v. = 0.47$. Nevertheless, the experimental sieve analysis does show an unexpectedly low presence of crystals in the smaller size classes and an unexpectedly high peak at around 550μm. This could be explained by agglomeration of small crystals during the drying process.

There is some discrepancy between the sieve analysis results and the model

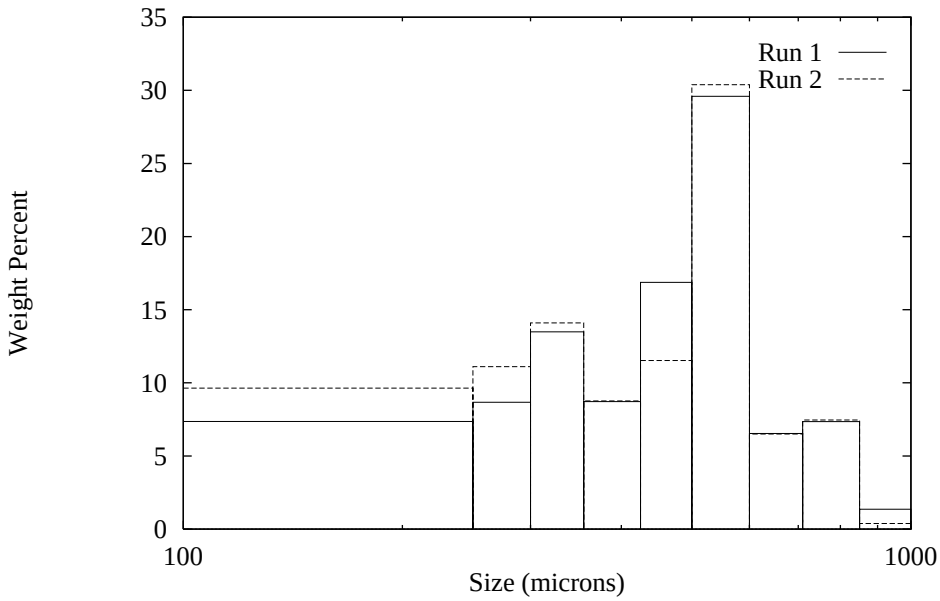

Figure 4.14: Sieve analysis results for two replicate experiments.

prediction, but they do demonstrate the same qualitative characteristics. It should also be noted that, while there are several sources for error in the sieve analysis, the analysis results are reproducible. The sieve analysis results for two replicate runs are given in Figure 4.14. The measured weight mean sizes for the two runs agree to within 16 μm, the coefficients of variation vary by only 0.03.

Chapter 5

Batch Crystallizer Control

Trying to control the future is like trying to take the master carpenter's place.

— Lao-tzu, as translated by Stephen Mitchell

The model formation and identification techniques described in previous chapters allow consideration of model-based control strategies. This chapter presents a flexible open-loop control strategy and the results of its experimental implementation. Possible feedback schemes are also discussed.

5.1 Review of Previous Open-loop Optimal Control Studies

Supersaturation is the driving force for both growth and nucleation. As shown by Mullin and Nyvlt [106], adjusting the supersaturation to maintain a constant nucleation rate increases crystal size and decreases fouling of heat exchanger surfaces. Most of the previous process control studies of batch crystallizers have dealt with finding the supersaturation-versus-time trajectory that has a desired effect on the product CSD.

The CSD of a cooling crystallizer can be affected by the cooling profile, because the supersaturation is a function of the crystallizer temperature. Jones and Mullin [90] demonstrate the determination of a cooling profile that maintains a constant supersaturation and conclude from simulations that this operating policy leads to a product CSD that is superior to that from natural or linear (constant-rate) cooling policies. They provide experimental verification that the constant-supersaturation cooling policy improves both the mean size and the variance of the CSD compared with natural cooling. Ulrich [162] provides results from implementing various cooling profiles on a system of an organic product in an acetone/water solution, showing that a temperature curve qualitatively similar to that suggested by Jones and Mullin gives products with larger crystals and less variation than that corresponding to natural

cooling or linear cooling.

Ajinkya and Ray [2] suggest that it would be desirable to determine the optimal operating policy that maximizes mean particle size and minimizes CSD variance in minimum time. Nevertheless, with the simplified model examined (assumptions included monodispersion of seeds and negligible nucleation), the only problem that could be addressed was that of manipulating cooling rate to maximize the size of the crystals. Morari [104] determines the analytical solution of this problem and tests the algorithm using a simulation study, but the model used is unrealistically simple and no experimental verification was performed.

Jones [86] applies optimal control theory and control vector iteration to find the cooling curve that maximizes the final size of the seed crystals. The temperature of the size-optimal control profile decreases slowly at early times and then rapidly at the end of the batch time, in direct contrast to the natural cooling curve. Chang and Epstein [24] also compute optimal temperature profiles for a variety of objective functions based on average size, volume, or variance of the final CSD. They use a gradient method to solve the two point boundary value problem for the optimal profile. Surprisingly, their results show an initial increase in supersaturation followed by a slow decrease, which is much closer to natural cooling than Jones' result. Although these works employ slightly different objective functions and crystallizer models, the source of the disagreement is not immediately clear. This disagreement is discussed further by Jones [87], who provides a general review of attempts to control batch crystallizers.

It should be noted that the open-loop optimal controllers of Jones and of Chang and Epstein are based on the ODEs that result from applying the method of moments to the population balance, so the objective function for the optimization must be a function of the moments of the CSD. The moment equations are a closed set only for the cases of no classified removal and for growth rates that are size-independent or linearly dependent on size. It should also be pointed out that the applicability of these methods is limited by the difficulty of incorporating constraints.

5.2 Statement of Control Problem as an NLP Problem

A general statement of the open-loop optimal control problem is:

$$\begin{aligned} \min_{\mathbf{u}(t)} \quad & \Phi(\mathbf{u}(t), \mathbf{x}(t_f); \boldsymbol{\theta}) \\ \text{subject to:} \quad & \text{Crystallizer Model} \\ & \mathbf{h}(\mathbf{u}(t), \mathbf{x}(t)) = \mathbf{0} \\ & \mathbf{g}(\mathbf{u}(t), \mathbf{x}(t)) \geq \mathbf{0} \end{aligned}$$

where $\mathbf{x}(t)$ is the vector of system states, and $\mathbf{u}(t)$ is the vector of system inputs (manipulated variables). This formulation is flexible with respect to the crystallizer configuration, the form of the kinetic expression, and the choices of objective function and manipulated variables. It allows the incorporation of input, output, and final-time constraints (e.g., constraints on cooling rate, supersaturation, and yield, respectively). With a finite-dimensional representation of the control, this formulation becomes a nonlinear programming (NLP) problem, for which there are standard algorithms.

Consider the case in which the crystallizer temperature is the manipulated variable. If the temperature is parameterized as piecewise linear, and the constraints consist of nonlinear state constraints and linear constraints on the temperature, then the optimal control problem can be restated as the following NLP problem:

$$\begin{aligned} \min_{\mathbf{T}} \quad & \Phi(\mathbf{T}, \mathbf{x}(t_f); \boldsymbol{\theta}) \\ \text{subject to:} \quad & \text{Crystallizer Model} \\ & \mathbf{b}_l \leq \mathbf{AT} \leq \mathbf{b}_u \\ & \mathbf{h}(\mathbf{x}(t_i)) = \mathbf{0} \quad i = 1, ..., m \\ & \mathbf{g}(\mathbf{x}(t_i)) \geq \mathbf{0} \quad i = 1, ..., m \end{aligned} \tag{NLP1}$$

where t_i is one of m points in time over the run, $\mathbf{A}$ is a constant matrix with n columns, and $\mathbf{T}$ is a vector of temperature values at n points in time between $t = 0$ and $t = t_f$.

For the control problems discussed subsequently, the successive quadratic programming code NPSOL [62] was used to solve the nonlinear programming problem.

5.2.1 Final-Time Constraints

There are cases in which constraints on final-time states of the system are necessary. In the absence of final-time constraints, there are many objective functions for which the solution of the optimal control is trivial but undesirable. For example, to minimize the number of nucleated crystals in the product, optimal operation would simply be a constant temperature profile at the saturation temperature—no formation of new crystals. The objective function would be at an absolute minimum, but the yield would be zero.

Final-time constraints allow the consideration of variables such as crystallizer yield. For a batch crystallizer, there is a one-to-one relationship between final solute concentration and yield. Therefore, if a desired yield is determined to correspond to a final concentration of, say $\hat{C}_y$, then a minimum yield is assured by imposing the final-time constraint:

$$\hat{C}_y - \hat{C}(t_f) \geq 0$$

This constraint clearly fits into the framework of NLP1.

5.2.2 Input Constraints

Because of physical limitations of equipment, there are usually bounds on manipulated variables and constraints on the rate at which they can be changed. NLP1 allows the incorporation of such constraints.

Because the temperature profile is parameterized as piecewise linear, a rate-of-change constraint and bounds on the temperature can be expressed as a set of linear constraints:

$$\left[\begin{array}{c} \mathbf{T}_{\min} \\ \hline -R_{\max}\Delta t_i \\ \vdots \\ -R_{\max}\Delta t_{n-2} \\ -R_{\max}\Delta t_{n-1} \end{array}\right] \leq \left[\begin{array}{ccccc} & & \mathbf{I} & & \\ \hline -1 & 1 & 0 & \cdots & 0 \\ 0 & -1 & 1 & & \vdots \\ \vdots & & \ddots & & 0 \\ 0 & \cdots & \cdots & -1 & 1 \end{array}\right] \mathbf{T} \leq \left[\begin{array}{c} \mathbf{T}_{\max} \\ \hline R_{\max}\Delta t_i \\ \vdots \\ R_{\max}\Delta t_{n-2} \\ R_{\max}\Delta t_{n-1} \end{array}\right]$$

where $\mathbf{I}$ is an $n \times n$ identify matrix, $R_{\max}$ is the maximum allowable cooling rate, $\mathbf{T}_{\min} = [T_{\min}, ..., T_{\min}]^T$, $\mathbf{T}_{\max} = [T_{\max}, ..., T_{\max}]^T$, $\mathbf{T} = [T(t_1), ..., T(t_n)]^T$, and $\Delta t_i = t_{i+1} - t_i$. These constraints can be enforced in NLP1 by defining $\mathbf{A}$, $\mathbf{b}_u$, and $\mathbf{b}_l$ accordingly.

An illustration of the implementation of a cooling rate constraint is given in Section 5.3.

5.2.3 State Constraints

There may be cases in which there are path constraints on the states (i.e., constraints on the states of the crystallizer over the course of a batch run). For example, to attempt to avoid homogeneous nucleation, an upper bound on the supersaturation over the run may be desired. But the methods by which to deal with state path constraints are not as transparent as for final-time and input constraints.

There have been several methods suggested for handling path constraints. A path constraint can be converted to a set of nonlinear constraints by time discretization of the states of interest, this is only an approximation and it can lead to a very large number of nonlinear constraints. Bryson and Ho [17] suggest augmenting the objective function with the integral of the path constraint violations; this, however, requires the choice of a suitable weighting parameter.

Sargent and Sullivan [145] suggest converting the path constraints into a final-time constraint by defining a new state variable that is equal to the integral of the squares of the path constraint violations. Consider the case in which there are p path constraints of the form

$$g_i(\mathbf{x}(t)) \geq 0$$

If a new state variable is defined as

$$\begin{aligned} \dot{x}_{q+1} &= \sum_{i=1}^{p} \{ \max(\, 0, -g_i(\mathbf{x}(t)) \,) \}^2 \\ x_{q+1}(t_0) &= 0 \end{aligned} \tag{5.1}$$

where q is the number of system states, the path constraints are satisfied if and only if the terminal constraint $x_{q+1}(t_f) = 0$ is satisfied.

This method avoids the computational difficulties of the time discretization technique and the arbitrary nature of the penalty function approach. An example of the implementation of this method to impose a state path constraint is given in Section 5.3.

5.3 Open-loop Optimal Control Examples

5.3.1 Maximizing Terminal Seed Size

The control policy that maximizes the final size of the seed crystals subject to $T(t) \in [T_{\min}, T_{\max}]$ can be determined by solving NLP1 with: $\mathbf{A}$ equal to the

Cooling Policy	Maximum Seed Size (μm)
Natural	895
Linear	959
Optimal	1043

Table 5.1: Summary of predicted effect of maximizing final seed size.

identity matrix, $\mathbf{b}_l = [T_{\min}...T_{\min}]^T$, $\mathbf{b}_u = [T_{\max}...T_{\max}]^T$, and the following objective function

$$\Phi = -\int_0^{t_f} G(t)dt$$

For the kinetic parameters of the KNO_3–H_2O system given in Table 4.6 and the physical parameters provided in Chapter 2, the optimal temperature profile and the corresponding model-predicted supersaturation profile are shown in Figure 5.1. The results for natural and linear cooling profiles are also given. As summarized in Table 5.1, optimal cooling leads to a predicted 17% increase in the terminal seed size over that of natural cooling and a 9% increase over that of linear cooling.

5.3.2 Minimizing Nucleated Crystal Mass

Downstream processes such as thickening and filtration are often time consuming steps—sometimes the production-limiting steps. The formulation of the control problem given by NLP1 allows consideration of the efficiency of downstream processes.

Compared to unimodal distributions, there are indications that the precipitate permeability and filtration efficiency are lower for bimodal CSDs—an inherent property of products of seeded crystallizers. Thus, the minimization of the ratio of the final mass of nucleation-formed crystals, $m_n(t_f)$, to the final mass of seed crystals, $m_s(t_f)$, would be expected to favorably affect the rate of filtration. This optimal control problem corresponds to the solution of NLP1 with: $\mathbf{A}$ equal to the identity matrix, $\mathbf{b}_l = [T_{\min}...T_{\min}]^T$, $\mathbf{b}_u = [T_{\max}...T_{\max}]^T$, and the following objective function and constraint:

$$\Phi = \left.\frac{m_n}{m_s}\right|_{t_f}$$

$$\hat{C}_y - \hat{C}(t_f) \geq 0$$

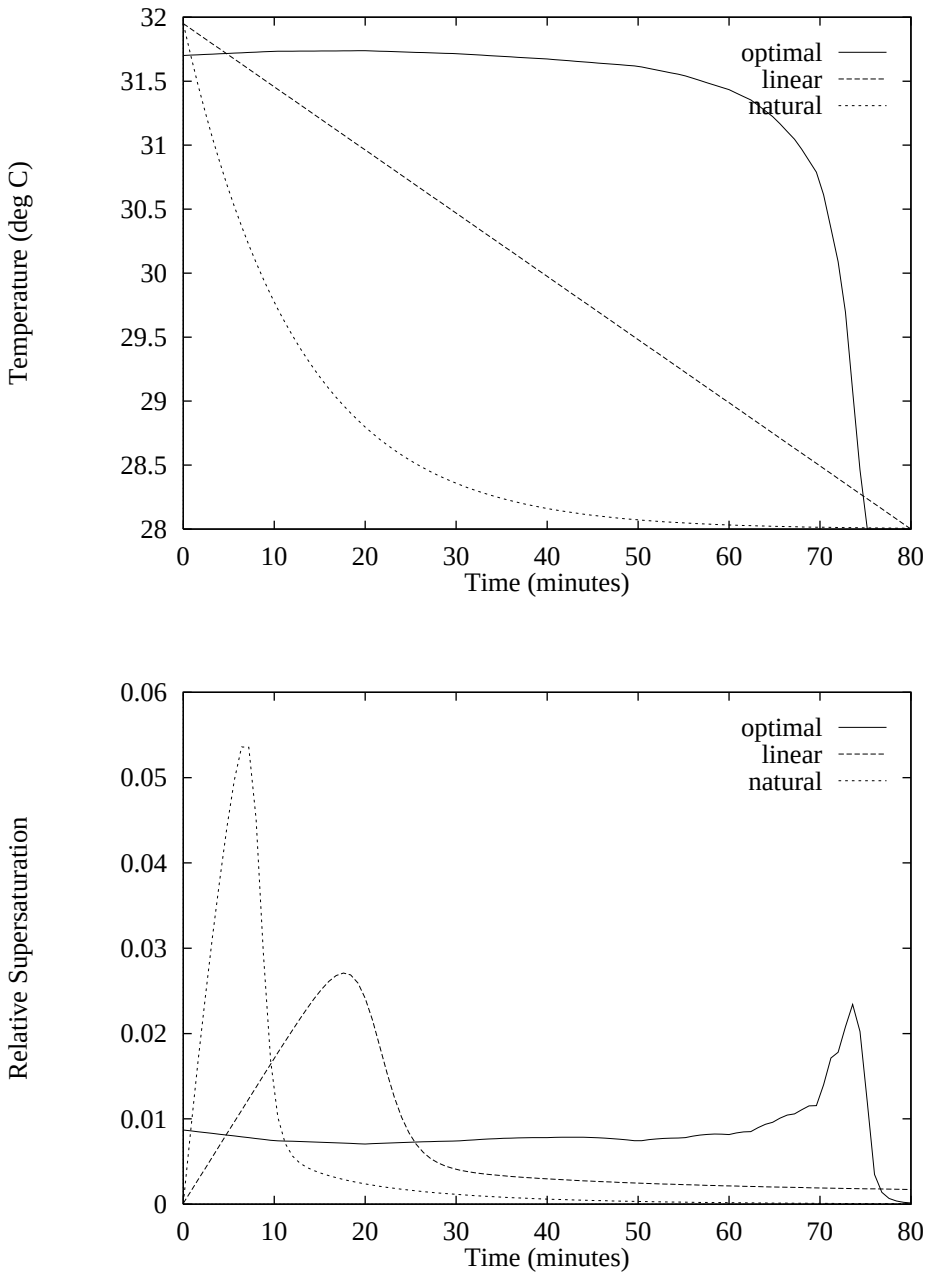

Figure 5.1: Temperature and supersaturation profiles for batch crystallizer. Cooling policies illustrated include natural cooling, constant-rate or linear cooling, and cooling controlled to maximize final-time seed size.

where the constraint represents the requirement of a minimum acceptable yield. For this problem, $\hat{C}_y$ was selected to be the final solute concentration resulting from cooling at a constant rate to $T = T_{\min}$.

The temperature profile that is predicted to minimize $m_n(t_f)/m_s(t_f)$ for the KNO_3–H_2O system is given in Figure 5.2; the corresponding supersaturation profile is also given. This optimal cooling policy requires a very rapid temperature decrease at the end of the batch run. Because of physical constraints or to avoid fouling of the cooling surface, this large cooling rate might not be feasible. As explained in Section 5.2, the control algorithm can handle a cooling rate constraint. Figure 5.3 shows the results of limiting the cooling rate to 0.1°C/min. To meet the yield constraint, the temperature must start its descent earlier for the case in which the cooling rate is constrained, resulting in an earlier and less-pronounced supersaturation peak.

There have been attempts to characterize the metastable region of crystallization, the region between saturation and spontaneous homogeneous nucleation. The saturation concentration can usually be represented as a simple, often linear, function of temperature. The metastable limit is the concentration above which there is spontaneous homogeneous nucleation. While it is usually dependent on the cooling rate, it is often characterized as a curve that is approximately parallel to the saturation concentration. With this type of characterization of the metastable region, spontaneous nucleation would be avoided by imposing a simple upper bound on $\hat{C} - \hat{C}_{\text{sat}}$:

$$g(\mathbf{x}(t)) = (\text{metastable bound}) - (\hat{C} - \hat{C}_{\text{sat}}) \geq 0$$

As discussed in Section 5.2, such a constraint on the path of a state of the crystallizer can be incorporated into the solution of the optimal control problem. To do so, g($\mathbf{x}$(t)) can be substituted into Eq. 5.1 to define an additional state variable that is constrained to a final-time value of zero. The result of placing a bound on the path of $\hat{C} - \hat{C}_{\text{sat}}$ is demonstrated in Figure 5.4.

The predicted effects of implementing temperature profiles to minimize the final-time value m_n/m_s, with and without constraints, are summarized in Table 5.2. Experimentally, the product of a batch crystallizer can be analyzed by sieve analysis. It is usually impossible to distinguish the difference between nucleated and seed crystals with sieve analysis, so this technique cannot provide a measurement of m_n/m_s. The weight mean size, L_{wm}, which can be assessed using sieve analysis, is included in Table 5.2 to provide a reference for the experimental study discussed in Section 5.6. Notice that the optimal temperature profiles have a positive effect on the weight mean size.

Because the optimal control policies are intended for open-loop implementation and are therefore to be solved off-line, computational efficiency issues

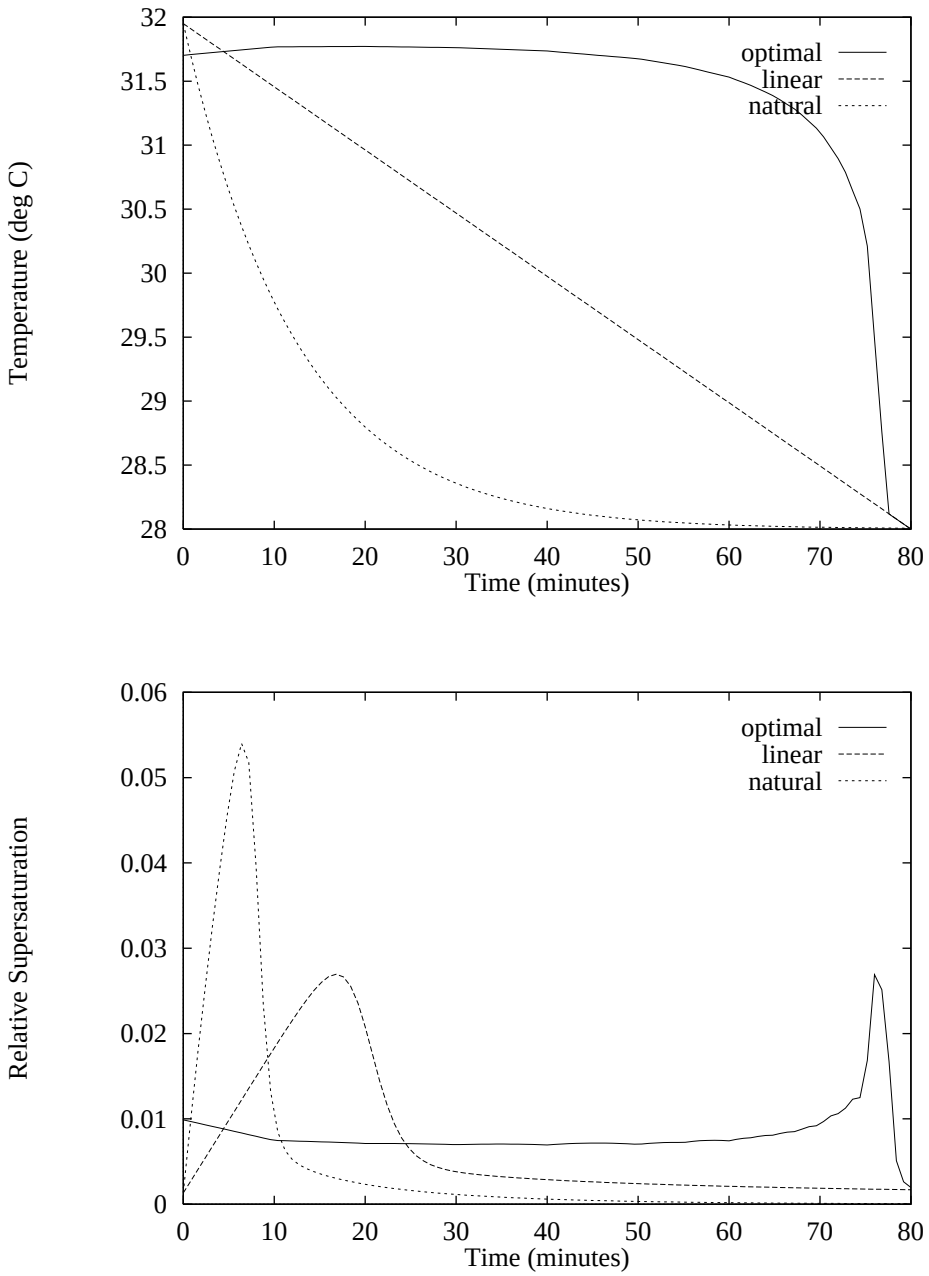

Figure 5.2: Temperature and supersaturation profiles for batch crystallizer. Cooling policies illustrated include natural cooling, constant-rate or linear cooling, and cooling controlled to minimize final-time value of m_n/m_s.

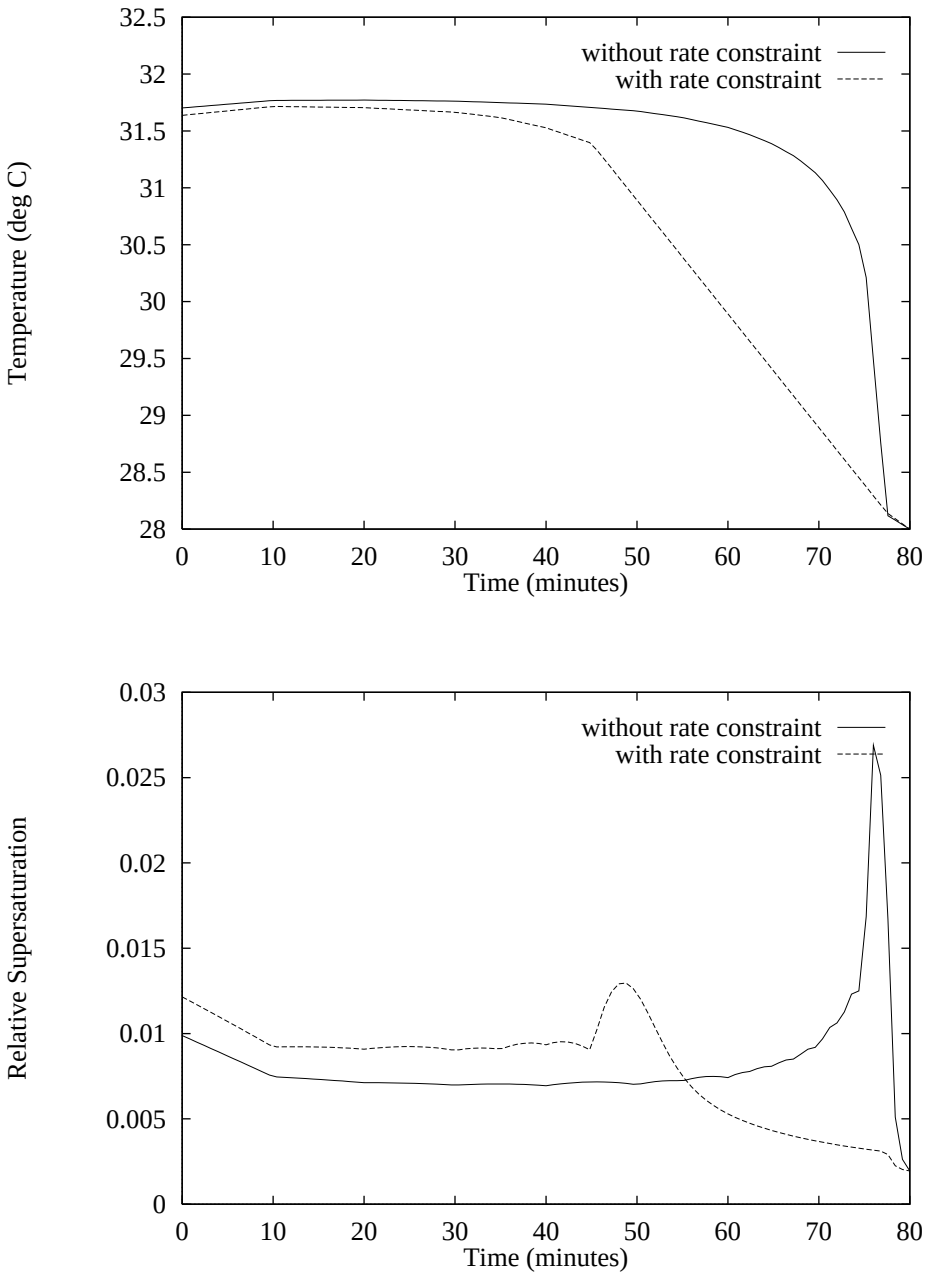

Figure 5.3: Demonstration of addition of cooling rate constraint of 0.1°C/min. Profiles are those for minimization of the final-time value of m_n/m_s.

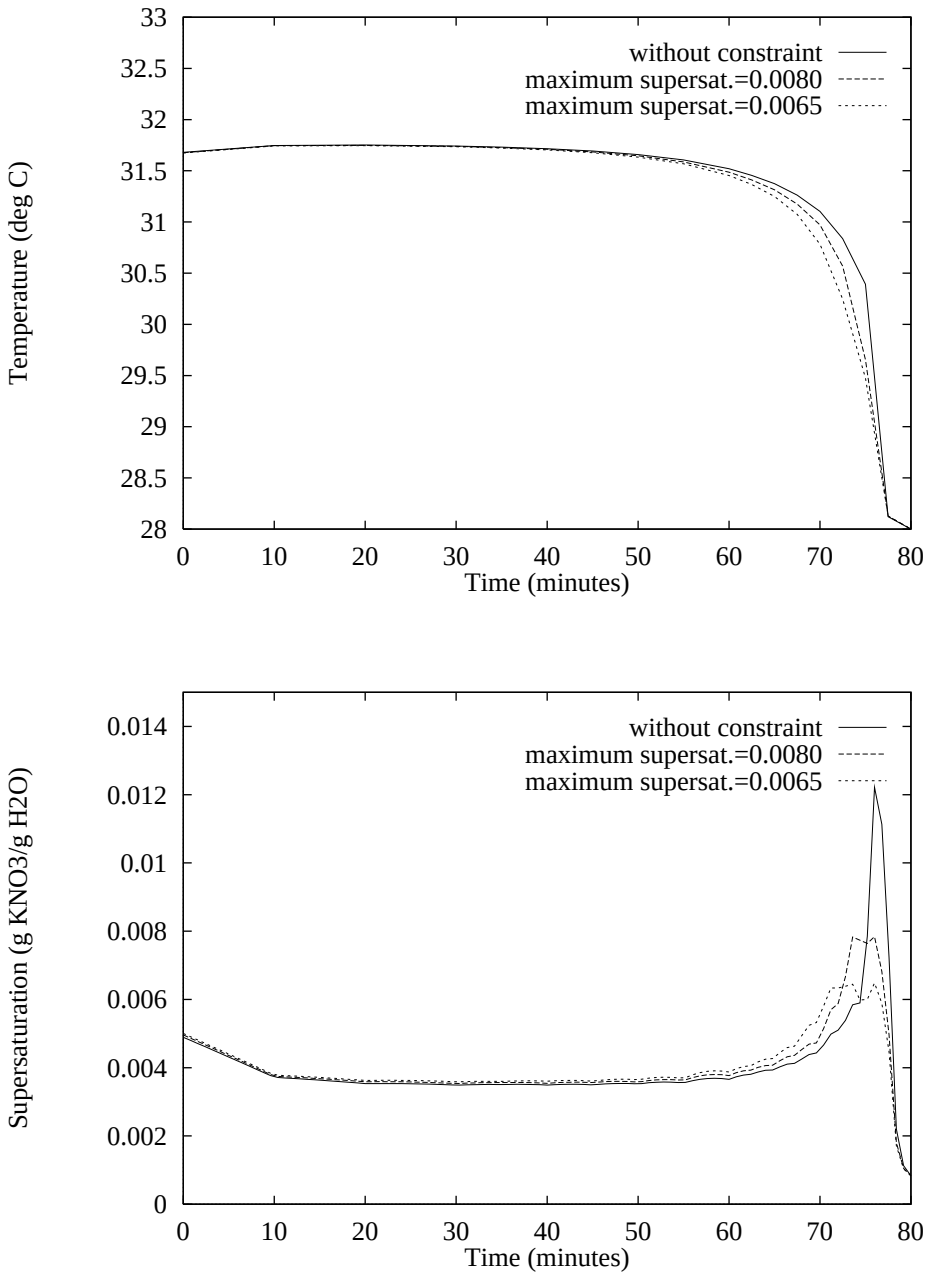

Figure 5.4: Implementation of a constraint on the maximum allowable value of $\hat{C} - \hat{C}_{\rm sat}$. Profiles are those for minimization of the final-time value of m_n/m_s.

Cooling Policy	m_n/m_s	Maximum Seed Size (μm)	L_{wm} (μm)
Natural	26.5	895	439
Linear	22.0	959	487
Optimal	17.5	1042	524
w/ cooling rate constraint	18.5	1023	521
w/ 0.0065 bound on $\hat{C} - \hat{C}_{\text{sat}}$	17.6	1042	527

Table 5.2: Summary of predicted effects of minimizing $m_n(t_f)/m_s(t_f)$.

were not carefully considered. Nevertheless, the following computation times on a DECstation 5000/240 are given to provide a point of reference: 45 minutes required for optimal policy subject to the yield constraint and simple bounds; 11 minutes required for problem with the additional constraint of a maximum bound on cooling rate; 21 minutes required for problem with the path constraint on supersaturation.

5.4 Assessment of Effectiveness of Method

In batch crystallization, nucleation and growth compete in the depletion of the solute concentration. Therefore, as Jones [86] suggests, controlling the CSD of the crystallizer product may be regarded as optimally distributing a resource among a population.

Maximizing terminal seed size and minimizing nucleated crystal mass are similar problems in that the ideal for both is exclusive allocation of the solute to the seed crystal with no new crystal formation. While this ideal is not attainable, the difference in the order of the dependence of growth and of nucleation on supersaturation does allow one phenomenon to be favored over the other.

For the KNO_3–H_2O system,

$$G = \exp(8.849)(\hat{S})^{1.32} \qquad B^\circ = \exp(17.142)(\hat{S})^{1.78}\hat{\mu}_3$$

The order of the dependence of nucleation rate on $\hat{S}$ is greater than that of growth rate. Therefore, the magnitude of both rates decrease as supersaturation is decreased, but relative to nucleation rate, the growth rate gains ground as $\hat{S}$ is decreased. This explains the supersaturation profiles for the optimal control examples given above (see Figures 5.1 and 5.2). In both cases, optimal

Cooling Policy	m_n/m_s	L_{wm} (μm)
Natural	6.18	876
Linear	3.64	1139
Optimal	1.98	1458

Table 5.3: Summary of predicted effects of minimizing $m_n(t_f)/m_s(t_f)$ for hypothetical chemical system.

operation corresponds to keeping the supersaturation very small over most of the run. Only at the end of the runs are there peaks of supersaturation, leading to rapid growth of existing crystals and bursts of new crystals; the timing is such that deposition of solute to new crystals is minimized because of the limited opportunity for their growth.

As shown in Tables 5.1 and 5.2, the benefit of implementing an optimal cooling profile for the KNO_3–H_2O system should be perceivable; as shown in Section 5.6 it is. The attainable benefit could be more or less significant, depending on the difference in the dependence of the growth and nucleation rates on supersaturation. To illustrate, consider a hypothetical chemical system with the following kinetic expressions:

$$G = \exp(8.849)(\hat{S})^{1.32} \qquad B^\circ = \exp(17.142)(\hat{S})^{2.78}\hat{\mu}_3$$

This is a system with the same growth kinetics as the KNO_3–H_2O system, but the order of dependence of nucleation rate on supersaturation is 2.78 instead of 1.78. As can be seen from Table 5.2, optimal cooling for the KNO_3–H_2O system leads to a predicted 33% decrease in the terminal value of m_n/m_s compared to that of natural cooling and a 20% decrease compared to that of linear cooling. As shown in Table 5.3, the relative benefit of optimal cooling for the hypothetical system is approximately twice as great.

5.5 Sensitivity of Optimal Profile to Model Parameters

Model-based control policies are, of course, determined using a nominal set of parameters. While these parameters are not known with total certainty, the parameter estimation scheme presented in Chapter 4 provides an assessment of the uncertainty. An analysis of the sensitivity of control policies to parameter

uncertainty and the impact of the uncertainty on the performance of the control strategy constitute a link between model identification and model-based control.

The dependence of the optimal open-loop control policy on the model parameters is illuminated by representing the control problem by a nonlinear operator $\mathcal{N}$ that maps the parameter space into the manipulated variable space:

$$\mathcal{N} : \Theta \rightarrow \mathcal{U}$$

The notation for the subsequent discussion can be simplified by considering an optimal control problem in which the input is parameterized as piecewise linear in time (like that stated in NLP1), because the input can be represented by a vector. The optimal control problem can be stated as

$$\mathbf{u} = \mathcal{N}(\boldsymbol{\theta})$$

where $\mathbf{u}$ is a vector representing the optimal profile of the manipulated variable for a given set of parameters, $\boldsymbol{\theta}$.

Let $\boldsymbol{\delta}\mathbf{u}$ be the difference between the optimal profile determined for parameters $\boldsymbol{\theta}$ and for that determined for $\boldsymbol{\theta}^\star$, the nominal set of parameters:

$$\boldsymbol{\delta}\mathbf{u} = \mathcal{N}(\boldsymbol{\theta}) - \mathcal{N}(\boldsymbol{\theta}^\star)$$

One way to examine the relationship between the optimal control policy and the parameter uncertainty is to determine the $\boldsymbol{\theta}$ in the confidence region that "maximizes" $\boldsymbol{\delta}\mathbf{u} = \mathcal{N}(\boldsymbol{\theta}) - \mathcal{N}(\boldsymbol{\theta}^\star)$. In other words, one approach is to find the worst-case deviation of the optimal control policy from the nominal profile for a given parameter confidence region. Maximizing $\boldsymbol{\delta}\mathbf{u}$ requires the definition of a norm of $\boldsymbol{\delta}\mathbf{u}$. While there are several reasonable choices, the 2 norm:

$$||\boldsymbol{\delta}\mathbf{u}||^2 = \boldsymbol{\delta}\mathbf{u}^T\boldsymbol{\delta}\mathbf{u}$$

provides a measure of the overall deviation of an optimal profile from the nominal optimal profile.

The vector that is amplified most (in the 2-norm sense) by the linear matrix operator $\mathbf{L}$ is the first column of the right singular matrix of $\mathbf{L}$. The singular value decomposition can be performed efficiently by routines in LINPACK [41].

Linearizing $\mathcal{N}$ about the nominal parameter set allows an approximate statement of the optimal control problem:

$$\mathbf{u} \approx \mathbf{L}\boldsymbol{\theta}$$
$$L_{ij} = \left.\frac{\partial u_i}{\partial \theta_j}\right|_{\theta^\star}$$

According to this linear approximation of the control problem,

$$\boldsymbol{\delta}\mathbf{u} = \mathbf{L}(\boldsymbol{\theta} - \boldsymbol{\theta}^\star) = \mathbf{L}\boldsymbol{\delta\theta}$$

and the $\boldsymbol{\delta\theta}$ that maximizes $\boldsymbol{\delta}\mathbf{u}^T\boldsymbol{\delta}\mathbf{u}$ is a multiple of $\boldsymbol{\delta\theta}_{\text{worst}}$, the first column of the right singular matrix of $\mathbf{L}$. In other words, the vector $\boldsymbol{\delta\theta}_{\text{worst}}$ is the direction in which $\boldsymbol{\theta}^\star$ can be perturbed that should lead to the largest change in $\mathbf{u}$.

For the KNO_3–H_2O system,

$$\theta^\star = [8.849 \;\; 1.32 \;\; 17.142 \;\; 1.78]^T$$

For the optimal control problem of minimizing the final-time value of m_n/m_s, the singular value decomposition of the finite difference approximation of $\mathbf{L}$ gives

$$\boldsymbol{\delta\theta}_{\text{worst}} = [-0.161 \;\; 0.930 \;\; -0.065 \;\; 0.324]^T$$

Figure 5.5 gives the results of solving the optimal control problem after perturbing the nominal parameter by $\pm 0.1(\boldsymbol{\delta\theta}_{\text{worst}})$. The analysis presented above suggests that the effect of perturbation of $\boldsymbol{\theta}^\star$ by an equal or lesser amount in any other direction should be less than that illustrated in Figure 5.5.

It was shown in Chapter 4 that the $100(1-\alpha)\%$ approximate confidence region is a hyperellipsoid defined by:

$$\boldsymbol{\delta\theta}^T\mathbf{V}_\theta^{-1}\boldsymbol{\delta\theta} = \chi^2_{N_p}(\alpha)$$

where $\chi^2_{N_p}$ is a random variable of a chi-square distribution with N_p degrees of freedom. The parameter sets in the confidence region that differ most from $\boldsymbol{\theta}^\star$ are the endpoints of the major axis of the hyperellipsoid. For $\Phi = m_n(t_f)/m_s(t_f)$,

$$\text{major axis endpoints} \equiv \pm\boldsymbol{\delta\theta}_{\max} = [-0.029 \;\; -0.006 \;\; 0.349 \;\; 0.090]^T$$

Perturbing $\theta^\star$ by $\pm\boldsymbol{\delta\theta}_{\max}$ leads to an imperceptible change in $\mathbf{u}$. As illustrated by Figure 5.6, perturbation of the same magnitude ($||\boldsymbol{\delta\theta}|| = 0.36$) in the direction of $\boldsymbol{\delta\theta}_{\text{worst}}$ leads to a significant change in the optimal $\mathbf{u}$.

While perturbing $\boldsymbol{\theta}^\star$ by a multiple of $\boldsymbol{\delta\theta}_{\text{worst}}$ can lead to a markedly different predicted optimal temperature profile, $0.36(\boldsymbol{\delta\theta}_{\text{worst}})$ is well outside of the 95% confidence region. The task of finding the parameter perturbation *within*

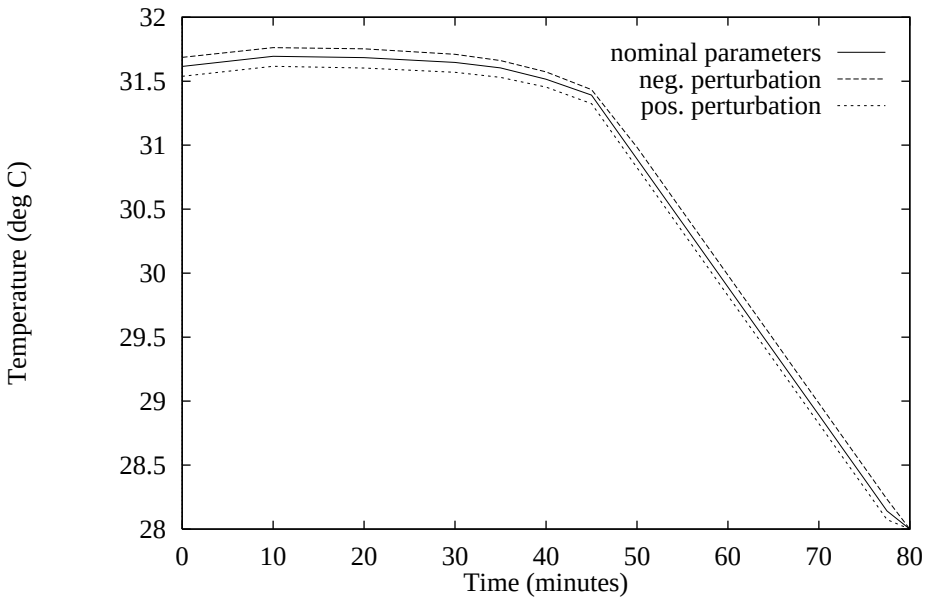

Figure 5.5: Sensitivity of control profile to parameter uncertainty. Optimal control policy for nominal parameters and for parameter sets perturbed by $\pm 0.1(\boldsymbol{\delta\theta}_{\text{worst}})$.

the confidence region that has the greatest effect on $\boldsymbol{\delta}\mathbf{u}$ can be stated as:

$$\boldsymbol{\delta\theta} = \boldsymbol{\theta}^{\star} \pm \gamma \boldsymbol{\delta\theta}_{\text{worst}} \tag{5.2a}$$

$$\gamma = \left(\frac{\chi^2_{N_p}(\alpha)}{\boldsymbol{\delta\theta}^T \mathbf{V}_{\theta}^{-1} \boldsymbol{\delta\theta}} \right)^{1/2} \tag{5.2b}$$

For the 95% confidence region of the KNO_3–H_2O system, $\gamma = 0.004$, which does not lead to a perceivable change in $\mathbf{u}$ from that determined for the nominal set of parameters. In other words, the sensitivity analysis suggests that for the tight confidence region of the KNO_3–H_2O kinetic parameters, the parameter uncertainty is not a concern in the determination of an optimal open-loop control policy.

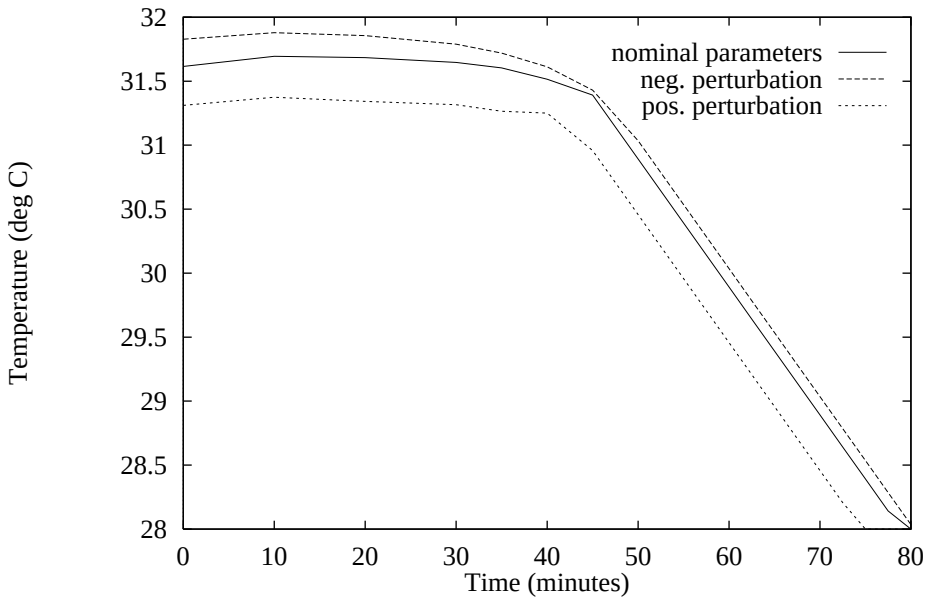

Figure 5.6: Sensitivity of control profile to parameter uncertainty. Optimal control policy for nominal parameters and for parameter sets perturbed by $\pm 0.36(\boldsymbol{\delta\theta}_{\text{worst}})$.

5.6 Experimental Implementation of Open-loop Control

The bench-scale crystallizer with a KNO_3–H_2O chemical system, the construction and operation of which is described in Chapter 2, was used to test the model-based control strategy. The example discussed above in which the objective was to minimize the terminal value of m_n/m_s was posed to possibly benefit efficiency of subsequent processing steps. This policy was chosen for implementation. As discussed, it is usually impossible to experimentally evaluate m_n/m_s, but the policy that minimizes m_n/m_s is expected to have measurable effects on variables that *can* be assessed.

The temperature measurements for typical runs of natural, linear and optimal cooling policies are shown in Figure 5.7. To incorporate the physical limitations of the cooling system, the optimal control policy was subject to a cooling rate constraint of 0.1°C/min. As shown, the temperature control system was able to track the linear and optimal temperature trajectories.

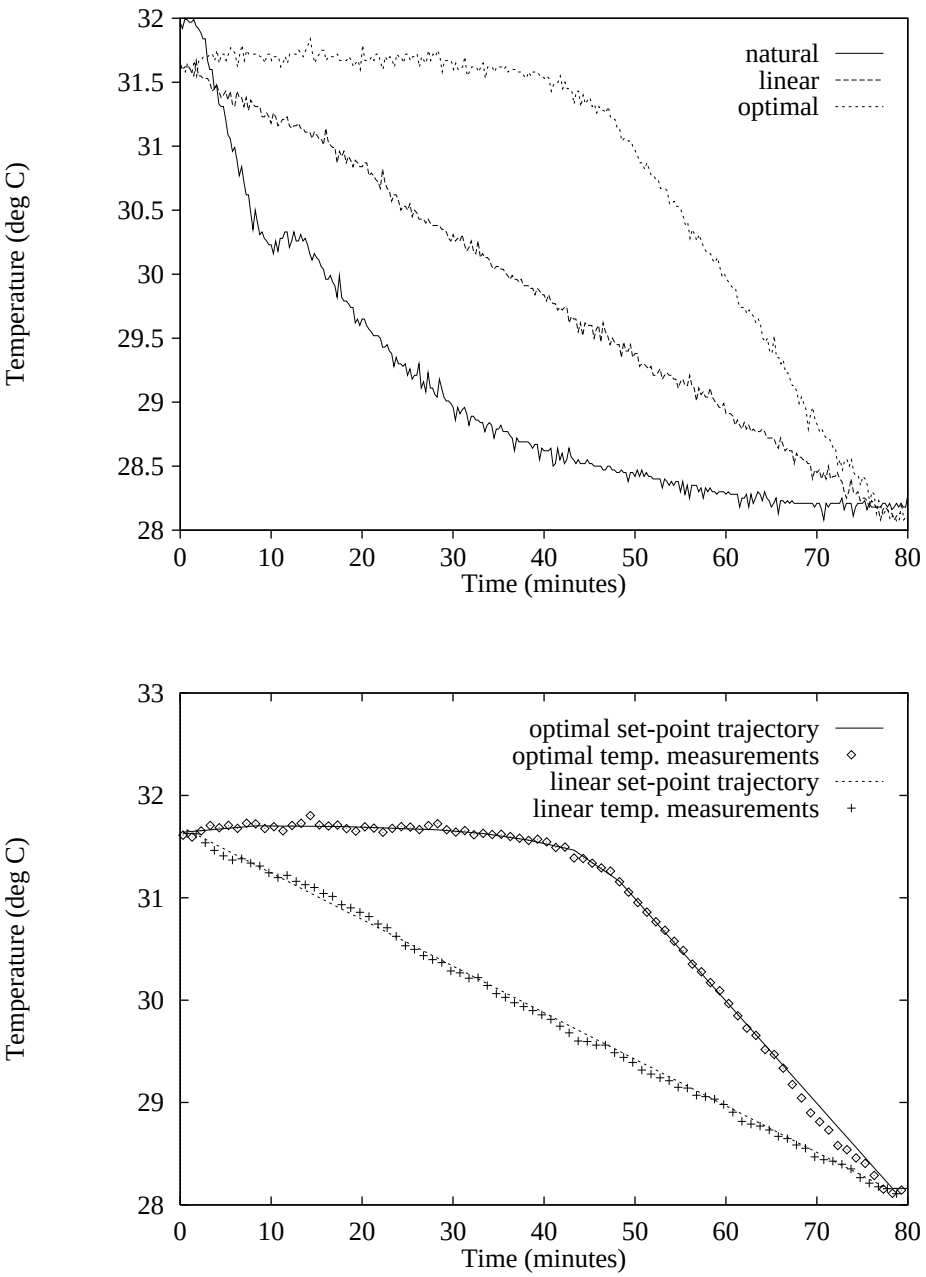

Figure 5.7: Experimental temperature data for natural, linear, and optimal cooling. Set-point trajectory tracking is also shown.

Figures 5.8–5.10 present the concentration and transmittance data corresponding to the natural, linear, and optimal cooling profiles shown in Figure 5.7. A comparison of these figures demonstrates the relationship between the temperature profile and the system output variables. The figures also demonstrate the effectiveness of the model in predicting the behavior of the system. The model parameters used were those given in Table 4.6—those obtained from the experiments discussed in Chapter 4.

The effect of the temperature profiles on the product of the crystallizer is demonstrated by the weight mean sizes given in Table 5.4; these are results from sieve analysis for the runs corresponding to Figures 5.8–5.10. The model predicted mean sizes are also given.

The sieve analysis results of several runs are given in Table 5.5. Operation was performed according to the policy given in Section 2.6 with initial concentrations of approximately 0.493 g KNO_3/g H_2O. With the exception of the case with higher seed loading (noted in the table), the only difference in the operating conditions for the runs was the cooling policy used. Because the final temperatures for the runs were not all equal, the yields were not consistent. To assess the effect of the cooling policy, runs with similar yields should be compared. (The crystallizer yields shown in the table were computed from the initial and final concentration measurements.)

As explained in Section 2.5, there are several sources of error in sieve analysis. From observations made during these experiments, the most likely source of error was agglomeration of small crystals during drying, which would be consistent with the unexpectedly high values of L_{wm} and low values of the coefficient of variation.

There is error in the sieve analysis results, and there is undoubtedly some error in the model, so it is not surprising that there is some disparity between the measured and model-predicted values of L_{wm}. Nevertheless, the qualitative effect of the cooling policy is the same: the weight mean size can be increased by using a linear cooling profile instead of allowing natural cooling, and a further increase can be realized by using the optimal cooling policy.

As discussed in Section 5.4, the increase in L_{wm} obtained by using cooling policies other than natural cooling is attained by avoiding the strong peak in supersaturation that is characteristic of natural cooling. The supersaturation data for natural, linear, and optimal cooling runs are given in Figure 5.11.

Table 5.5 includes the results from the implementation of an optimal control policy in which the seed loading was higher than that of the other runs—loading was higher by a factor of 10. Figure 5.12 demonstrates that the difference between the optimal temperature trajectories implemented for the lower and the higher seed loading was not very great. However, as shown by a com-

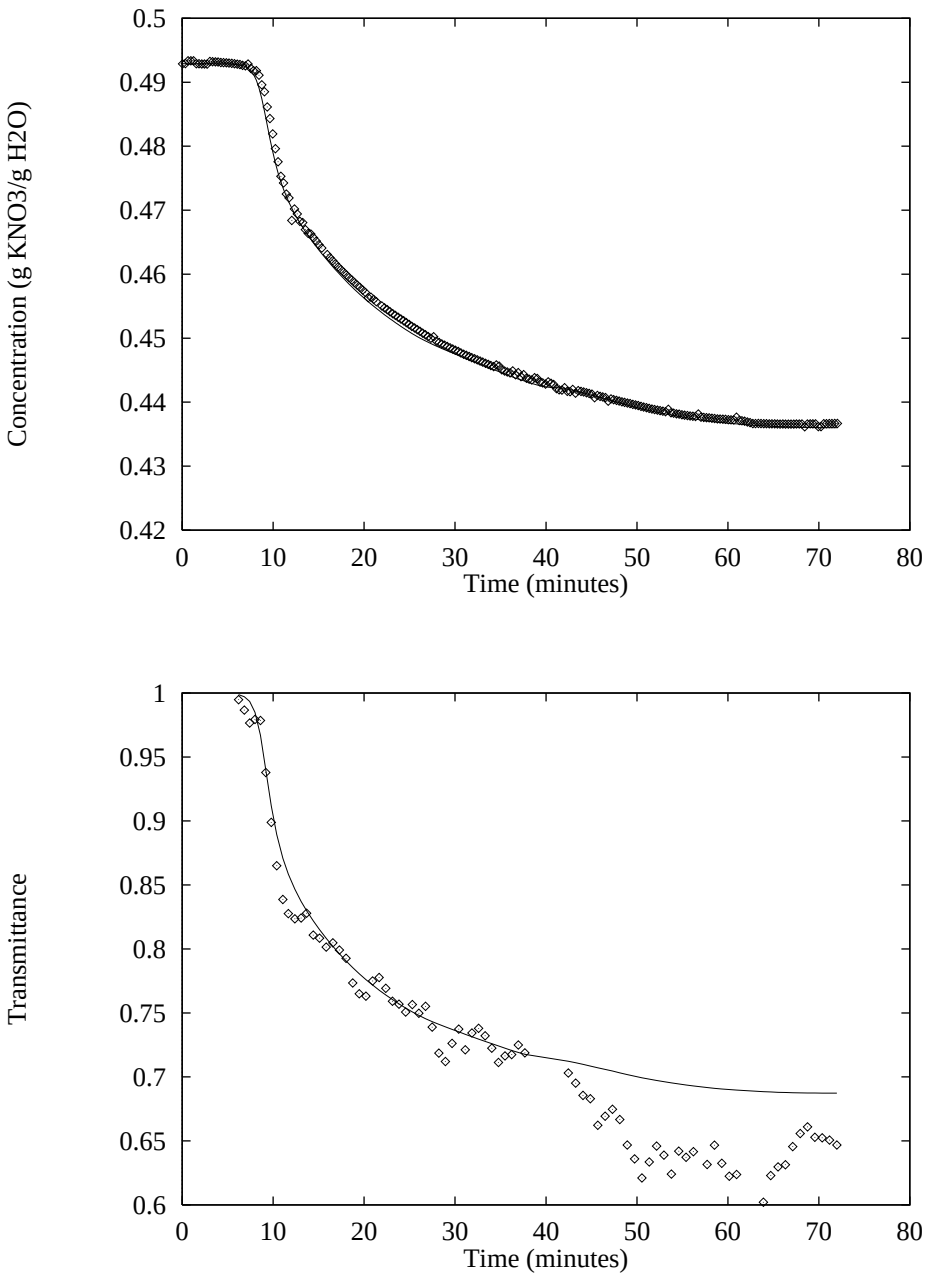

Figure 5.8: Concentration and transmittance measurements and model predictions for natural cooling operation.

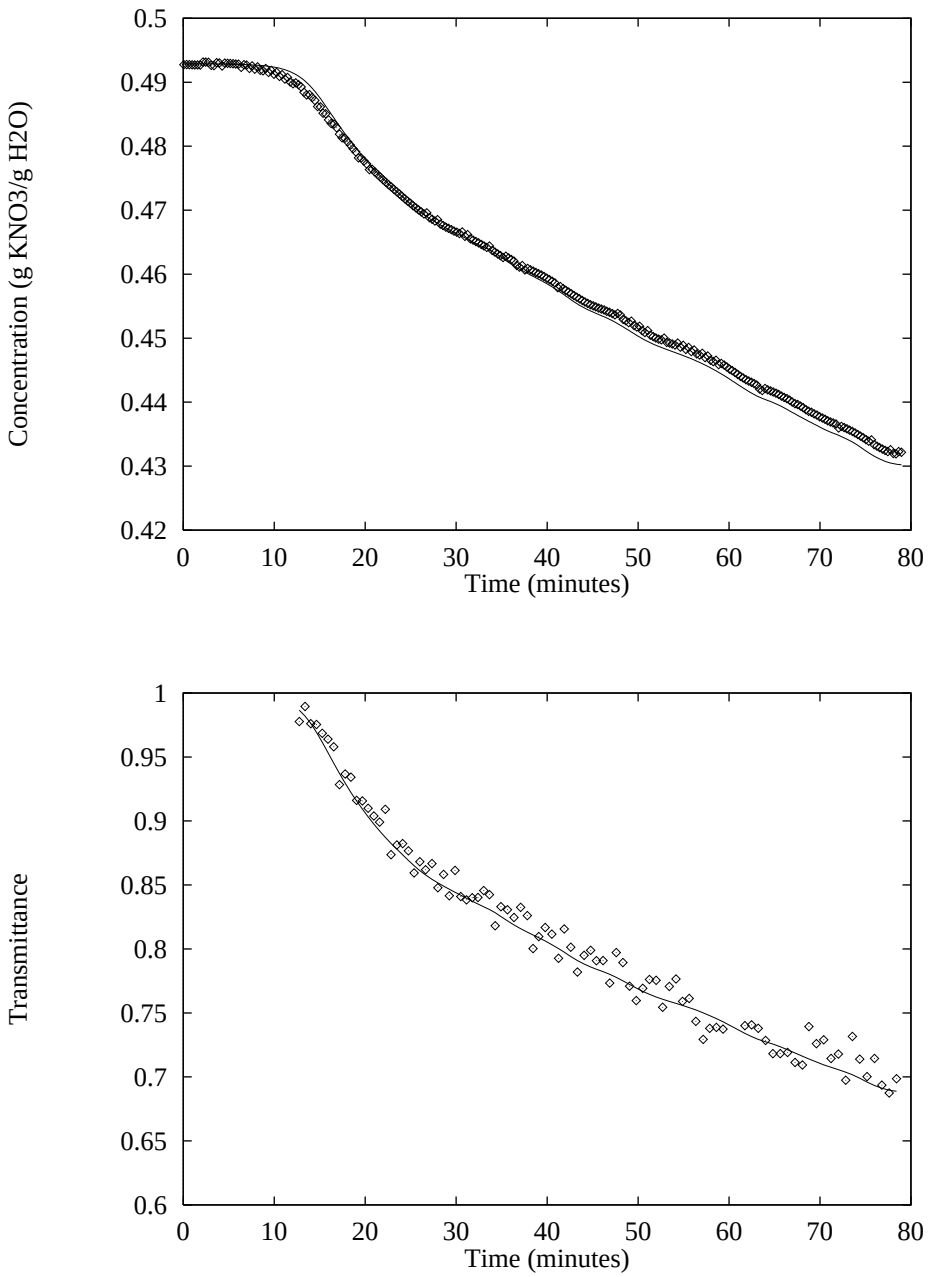

Figure 5.9: Concentration and transmittance measurements and model predictions for linear cooling operation.

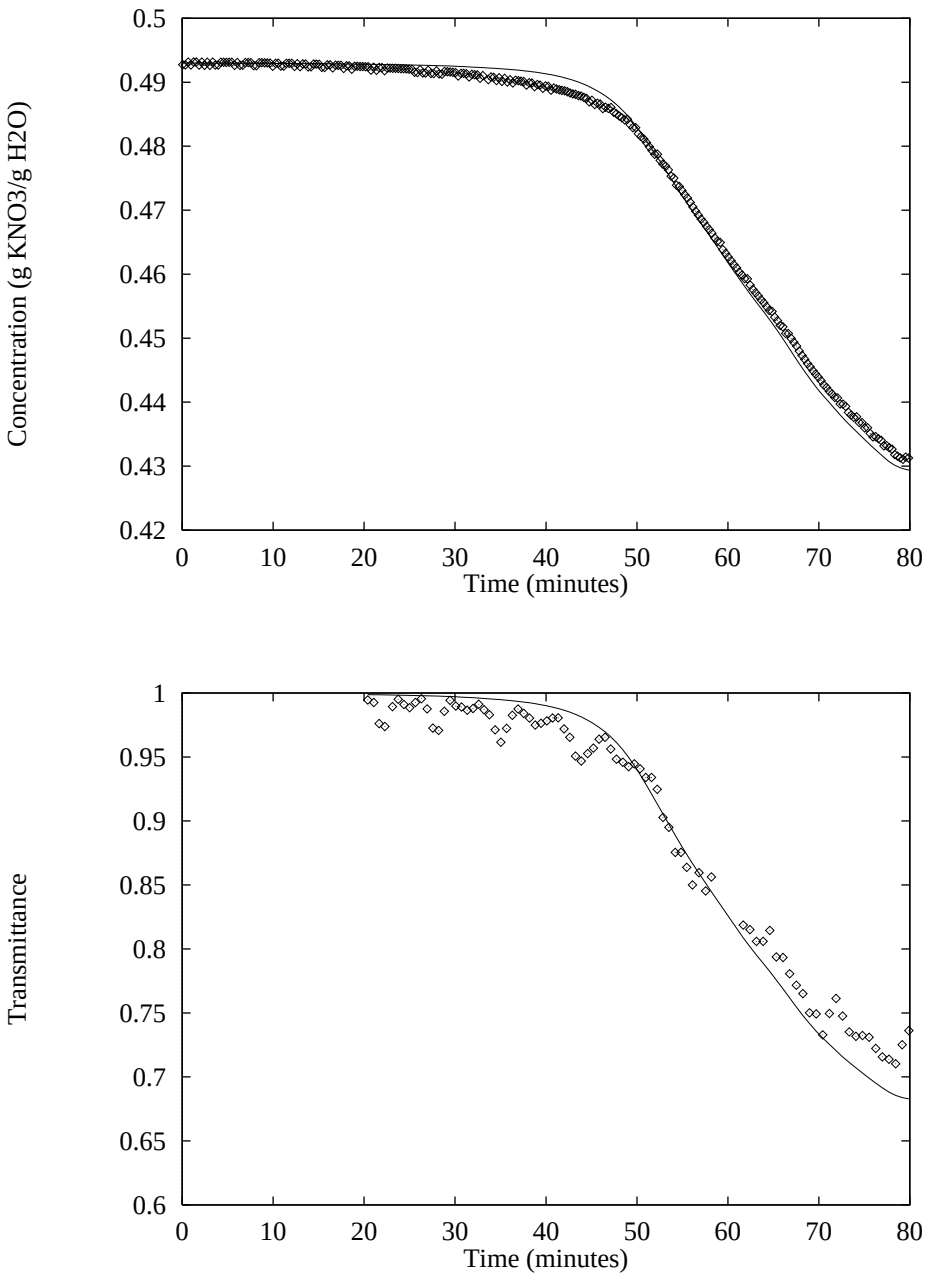

Figure 5.10: Concentration and transmittance measurements and model predictions for optimal cooling policy implementation.

Cooling Policy	Measured L_{wm} (μm)	Model-predicted L_{wm} (μm)
Natural	449	448
Linear	630	493
Optimal	666	514

Table 5.4: Effects of temperature profiles on weight mean size of crystallizer product.

Cooling Policy	T_f (°C)	Yield (g)	Measured L_{wm} (μm)	Predicted L_{wm} (μm)	Measured $c.v.$	Predicted $c.v.$
Natural	28.2	98	449	448	0.40	0.47
	28.3	99	460	450	0.36	0.47
	28.4	93	465	448	0.37	0.47
Linear	28.1	101	630	493	0.41	0.46
	28.1	103	564	492	0.39	0.47
	28.5	92	532	492	0.36	0.47
Optimal	28.1	102	666	514	0.49	0.50
	28.4	91	507	481	0.44	0.50
	*27.8	107	574	470	0.26	0.22

* High seed loading used in run.

Table 5.5: Weight mean size and coefficient of variation of crystallizer product of several runs.

parison of Figures 5.10 and 5.13, the difference in the system behavior was significant. The high seed loading led to an immediately perceivable transmittance decrease. The seed load was high enough that the solute deposition on the seed crystals resulted in a decrease in the concentration early in the run, while there was a relatively long induction period for the case of low seed loading. It should be noted that the model is able to predict the system behavior for the high seed loading experiment, even though model identification was performed using data from low seed loading experiments.

The examples discussed in Section 5.3 and the experimental results described in this section demonstrate the use of the open-loop optimal control strategy. Other performance indices may be determined to be more beneficial, and the use of temperature as the lone manipulated variable may be deemed

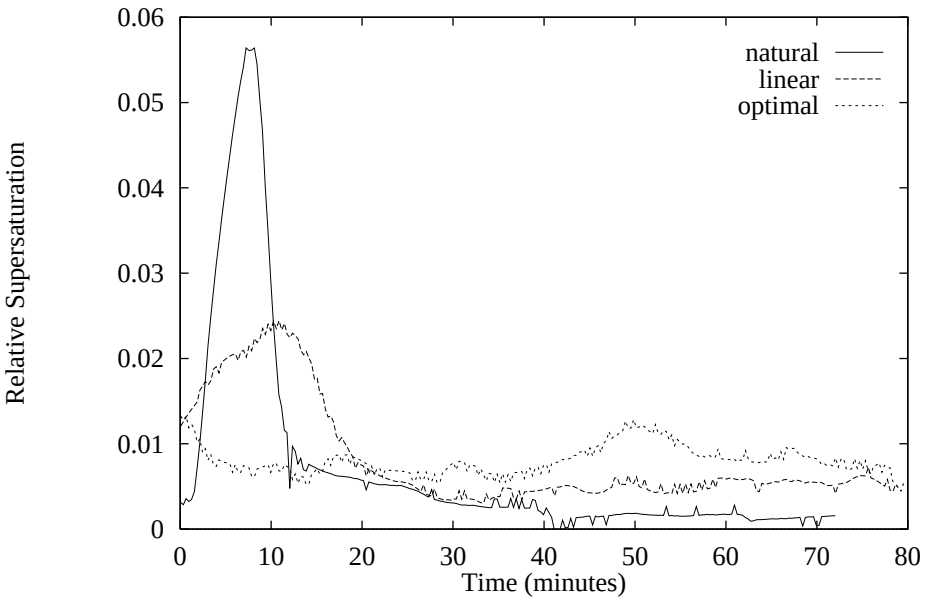

Figure 5.11: Experimental relative supersaturation data for natural, linear, and optimal cooling.

to be inadequate for a particular system. Nevertheless, the technique is flexible enough to accommodate various performance indices and manipulated variable choices.

5.7 Suggestions for Incorporating Feedback

Much insight is provided by computing the optimal open-loop cooling profiles for batch crystallizers. Such calculations allow determination of general operating guidelines for producing CSDs with selected characteristics. The optimal cooling profile by itself, however, may not be sufficient to control a crystallizer. As demonstrated by Bohlin and Rasmuson [11] via simulation and experimentally by Chianese et al. [27], even the qualitative benefits expected from optimal cooling profiles are not necessarily realized, at least not reproducibly. Poorly characterized kinetics and inaccurate process control (i.e., poor implementation of profiles) are the probable causes of the shortcomings.

It has been shown in this chapter that there are effective techniques for

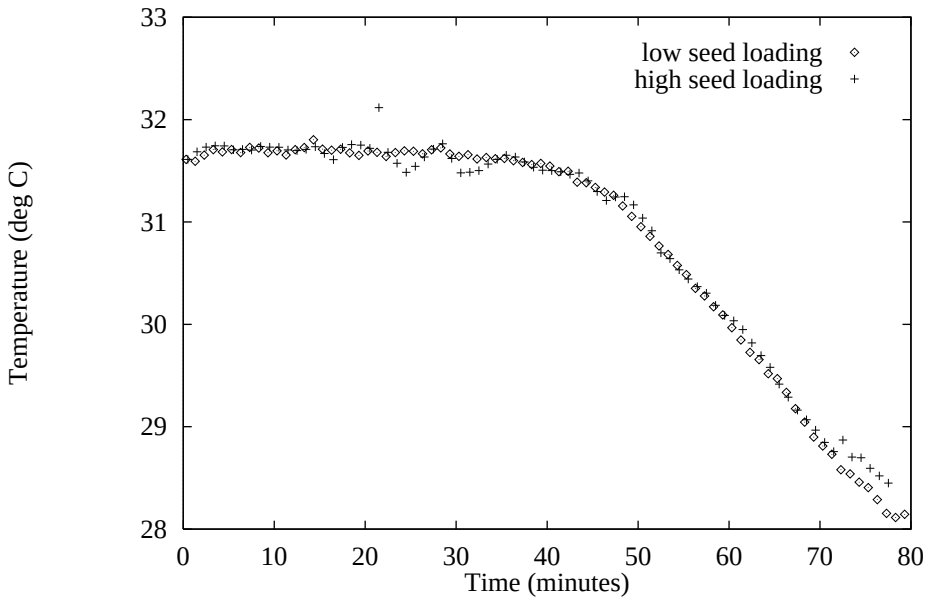

Figure 5.12: Optimal temperature profiles for high and low seeding.

implementing an optimal manipulated variable trajectory. It has also been shown that the kinetic parameters and their confidence regions can be estimated, and that, at least for the KNO_3–H_2O system, the kinetic characterization is sufficiently reliable to assure the desired system behavior. Nevertheless, for a particular system, the plant/model mismatch, the deviations from the nominal trajectory, or the system disturbances may be significant. Possible disturbances include improper seeding (e.g., adding incorrect size or amount of seeds, or seeding at the incorrect system state) and batch-to-batch variations (usually due to impurities and solvent effects). In other words, there are cases in which feedback compensation would be necessary.

Chang and Epstein [25] suggest a strategy for incorporating feedback in the optimal control scheme that is based on the assumption that the system state trajectory is in the vicinity of the nominal optimal trajectory. Assuming that the moments of the CSD can be measured or estimated, a one-step iteration in a gradient search technique is used to find a new trajectory with an improved performance index. Simulation studies were used to demonstrate the application of this control scheme, but it has not been experimentally verified.

A natural way to incorporate feedback into the controller is to periodically

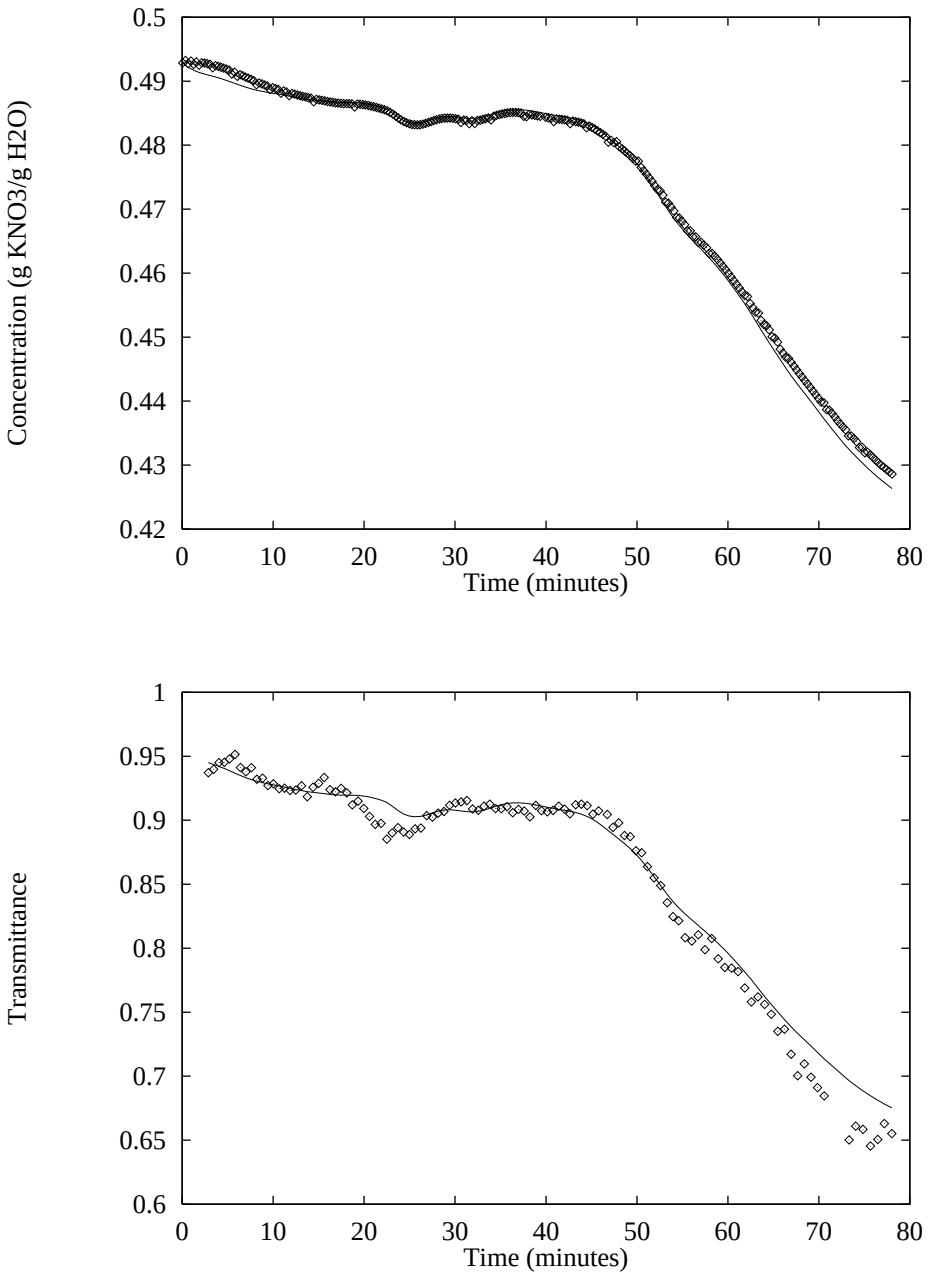

Figure 5.13: Concentration and transmittance measurements and model predictions for optimal cooling policy implementation with high seed loading.

compute an optimal control trajectory after using available measurements to estimate the unmeasured states and possibly update the model's parameters. Eaton et al. [46, 44] and Patwardhan et al. [114] have applied on-line nonlinear estimation and control strategies to several chemical engineering processes. For a system like that used in this study, the temperature and measures of the second and third moments can be obtained. The nonlinear state estimation problem may be possible with an extended Kalman filter or by a nonlinear optimization technique suggested by Jang et al. [82] and Liebman et al. [100].

A more conventional approach that could be used as a basis of comparison is to use state estimation with a linear quadratic (LQ) optimal controller based the linearized ODEs obtained after using some lumping technique on the crystallizer model (method of moments, method of lines, etc.). Kwakernaak and Sivan [96] and Bryson and Ho [17] are standard references for LQ design.

A feedback control scheme that is not rooted in optimal control theory has been suggested be Rohani et al. [142]. The strategy is based on the hypothesis that the final CSD can be improved by maintaining the fines slurry density at some constant value over a batch run. They experimentally verify that by maintaining the fines slurry density at a set point using a conventional PI controller to manipulate the fines destruction rate, the final mean crystal size is increased and the coefficient of variation is reduced. A simulation study by Rohani and Bourne [141] shows a self-tuning regulator to be more effective in set-point tracking and disturbance rejection than the PI controller.

Some simple feedback schemes have proven to be effective. The timing of the seeding of a batch sucrose crystallizer is one of the steps that is automated in a control system discussed by Virtanen [165]. The goals of automating the existing batch equipment were to shorten the crystallization time, produce a more uniform CSD, and reduce the labor and energy costs. In the control strategy, a microcomputer adjusts the steam flow rate to maintain constant supersaturation based on on-line density and refractive index measurements. The computer also regulates the timing of the feed addition, concentration, seeding, and growing steps for each batch. The control scheme was implemented at the Finnish Sugar Co. Ltd. and the biggest gains were achieved in decreasing batch-to-batch variations, decreasing the labor costs, and improving power plant economy.

Chapter 6

Conclusions and Future Work

Education is hanging around until you've caught on.
— Robert Frost

Batch crystallizers are used extensively in the chemical industry, but most of the crystallizer control efforts have focused on continuous crystallizers. The control algorithms that have been developed for control of batch crystallizers are limited to specific crystallizer configurations and do not allow incorporation of constraints. The main objective of this work was to determine a flexible, model-based strategy for batch cooling crystallizers that handles input, output, and final-time constraints. While control of the distribution of purity and shape of a population of crystals is of industrial interest, the purpose of this research was control of crystal size distribution (CSD), a property of importance to the consumer and one that has a strong effect on the efficiency of downstream processes.

Model identification plays an important role in a model-based control algorithm, and development of a model identification technique was an important part of this research. The determination of model parameter uncertainty allows analysis of the information content of various measurement techniques. To obtain a model that reliably characterizes the behavior of the system, an assessment of parameter uncertainty was considered a necessary element of the identification technique.

Model Identification and Measurement Techniques

The population balance approach provides a modelling framework for determining the structure of models for crystallizers, but the limitations of measurement technology for these systems have confounded parameter estimation. This difficulty has been obscured by the fact that most of the previous studies of crystallization kinetic parameter estimation have not provided an assessment of the reliability of the parameter estimates. One of the principal goals of this research was to develop a parameter estimation technique that includes

	$\ln(k_g)$	g	$\ln(k_b)$	b
Estimate	8.014	1.10	14.710	0.85
Interval	$\pm$0.423	$\pm$0.12	$\pm$6.268	$\pm$2.48

Table 6.1: Results of parameter estimation based on concentration measurements.

a determination of the uncertainty of model parameters.

The parameter confidence regions obtained in this study are elliptical regions based on linear statistics. It has been shown that for nonlinear problems these approximate confidence regions can underestimate or overestimate the actual confidence regions. Nevertheless, Monte Carlo studies and replicate data were used to demonstrate that, at least for the system of interest, the elliptical regions provide a reasonable representation of the actual confidence regions. It was then demonstrated that the assessment of parameter uncertainty can be used in experimental design; experimental design becomes the task of choosing operating conditions and measurements that minimize the volume of the confidence region and the correlation between parameters.

Using data from a bench-scale KNO_3–H_2O crystallizer, it was shown that measurement of continuous-phase concentration, the sole data source in many parameter estimation studies, provides insufficient information for identifying a model. This is illustrated by the large uncertainty shown in Table 6.1 for the parameter estimates resulting from concentration measurements. As intuition would suggest, solid-phase information is necessary to obtain kinetic parameters for both crystal growth and nucleation.

This dissertation points out the shortcomings of CSD measurement techniques based on light scattering, but it demonstrates the potential of the measurement of the transmittance of light through a sample of crystals. It is shown that, while there is a limit to its range of applicability, the Beer-Lambert law provides a model that relates the CSD and the transmittance measurement; the result is a one-to-one connection between transmittance and the second moment of the CSD. For the batch cooling crystallizer used in this study, the transmittance and concentration measurements contain enough information to obtain reliable parameter estimates. The uncertainty in the parameter estimates can be reduced further by using data from experiments that achieve a wide range of supersaturation. The parameter estimates and confidence intervals obtained for the KNO_3–H_2O system are summarized in Table 6.2.

	$\ln(k_g)$	g	$\ln(k_b)$	b
Estimate	8.849	1.32	17.142	1.78
Interval	± 0.112	± 0.03	± 0.360	± 0.09

Table 6.2: Summary of parameter estimates and confidence intervals for KNO_3—H_2O system. Estimation based on concentration and transmittance measurements from experiments with various temperature profiles.

The model with these parameters was shown to accurately predict the behavior of the system, even in operating regions significantly different from the experiments used for model identification.

For further model validation, the results of sieve analysis were compared to the model predictions. The agreement was reasonable, but there was some variance between the experimental and model-predicted results. The crystal weight/size mode from sieve analysis and the model predictions were basically in agreement, but there were consistently fewer small crystals than expected and a greater-than-expected number of crystals in one of the larger size classes. This is consistent with aggregation of small crystals. From observations before and after drying, aggregation during filtration and drying is the most likely explanation, and the decision to neglect agglomeration during crystallization is probably reasonable.

As discussed by Estrin [47], there are some systems for which agglomeration during crystallization cannot be neglected. Agglomeration is difficult to characterize, but, as described by Estrin, there have been some attempts to include its effect in the model structure. From control considerations, agglomeration is of concern because the degree to which it occurs is strongly dependent on the operating conditions and, therefore, on the manipulated variables.

The solid-phase information obtained from the transmittance measurement is sufficient for model identification for the system used in this study, but the CSD information content is limited and probably would not be reliable for systems in which agglomeration is significant or in which the crystal shape is not regular or well defined.

Kane et al. [92] used a strobe and a camera to obtain images that, with considerable tedium, provided a CSD measurement. The recent advances in image processing and analysis algorithms and computer hardware may make such an approach feasible for on-line application. The advantages of direct

observation techniques are that they do not suffer from the ill-conditioning of inference techniques, and an assumption about particle shape is not necessary.

The primary remaining challenges of imaging techniques are obtaining quality images that are representative of the CSD and compensating for flaws in the images. Fantini et al. [49] give an algorithm that automatically handles images that are out of focus, a problem in analysis of microscopic images. They compare their results for characterizing droplets in a spray with those of light scattering techniques.

Use of digital image processing for particle sizing is still in the developmental stage, but there have been several demonstrations of the application of digital image analysis to determining particle size distributions [154, 69]. Direct digital imaging may prove to be the most effective technology for the future.

For engineering design and control purposes, the crystal nucleation and growth expressions are empirical and will likely remain so in the near future due to the complexity of these phenomena. Hoare's Law of Large Problems states that within every large problem is a small problem trying to get out; within the large problem of crystallization modelling, the characterization of growth and nucleation is a problem that requires further attention.

Although the structure of the power-law expressions allowed characterization of the growth and nucleation rates for the system used in this study, it would not be appropriate for some systems. There are chemical systems for which there is a dispersion in the growth rate of crystals; these are systems for which the growth rate expression used in this study would be inadequate. Perhaps what is required in the near term for developing models with an intended control purpose is a more flexible empiricism. Fundamental models used in conjunction with flexible empirical models such as neural networks, radial basis functions, or multivariate splines is a developing area of research [118, 95, 84]. The use of such flexible nonlinear functions for nucleation and growth, within the fundamental population balance framework to describe the CSD, may prove to be a useful approach.

This dissertation demonstrates efficient solution techniques for batch crystallizers with size-independent and size-dependent growth rates, but development of a solution method is still on a case-by-case basis. The solution of a model for a new crystallizer configuration requires significant effort. Therefore, substantial benefit would be derived from the development of a unified approach that handles the entire class of population balance models, an approach analogous to the implicit predictor/corrector methods with variable step-size that efficiently handle a large class of ODEs.

Model-Based Control

A model-based control strategy was developed for determining and implementing an open-loop policy that is optimal with respect to a specified performance index. The control scheme handles input, output, and final-time constraints, and it permits flexibility in crystallizer configuration and in objective function formulation. This flexibility allows consideration of objective functions that take into account solid-liquid separation in subsequent processing steps.

In this dissertation, temperature was the only manipulated variable considered. Compared to natural cooling, increases in the weight mean size of up to 48% were achieved through implementation of optimal cooling policies on the bench-scale KNO_3–H_2O system. As shown from a simulation study of a hypothetical chemical system, the impact of the optimal temperature profile on the final CSD is strongly dependent on the growth and nucleation parameters.

Jones et al. [89] have investigated the feasibility of using fines dissolution in a batch crystallizer. Their experimental results indicate that fines dissolution can remove the crystals formed by secondary nucleation, increase the average crystal size, and decrease the coefficient of variation of the CSD. The energy costs of using fines dissolution would have to be taken into account, but the rate of dissolution would provide an additional manipulated variable that could be used in the optimal control strategy presented in this study.

Although reactive crystallization was not studied in this work, it does fit into the model identification and control framework presented in this dissertation. The feed flow rates of reactants could be used as manipulated variables, providing other means by which to influence the driving force of crystallization.

Sensitivity of control policies to parameter uncertainty is the issue that links the model identification problem and the control problem. This issue was investigated by calculating the direction of perturbation of the nominal parameter set that would most affect the determination of the optimal control policy. It was shown that the confidence region of the KNO_3–H_2O system is such that parameter uncertainty is not a concern in the determination of a control policy.

It was shown that there are effective techniques for implementing an optimal manipulated variable trajectory. It was also shown that the kinetic parameters and their confidence regions can be estimated with sufficient reliability to assure the desired behavior for the KNO_3–H_2O system. Possible disturbances of an industrial process include improper seeding (e.g., adding incorrect size or amount of seeds, or seeding at the incorrect system state) and batch-to-batch variations (usually due to impurities and solvent effects). It is also possible to have deviations from the nominal input trajectory. A discus-

sion is given of the potential need for feedback compensation, and suggestions are given for methods to incorporate feedback.

Goals for future work should include the development of measurement techniques and the attainment of a level of understanding of the underlying phenomena that are sufficient for modelling and control of crystal morphology and purity. Public domain software for morphology prediction [37, 30, 38] has been developed recently. The use of this software for quantitative prediction of crystal morphology for certain ideal organic crystals is well established, and progress is being made for the more difficult ionic crystals as well [101].

Attempts have been made to calculate the effect of impurities and different solvent mixtures on final crystal habit [109]. Myerson's conclusions from his review of this area are that there are not as yet reliable methods to predict habit or select solvents and habit modifiers without extensive trial-and-error experimentation, but recent progress may make habit and purity control a realistic goal for the near future [107].

While quantitative microscopic prediction of crystal shape and purity is not as well developed as the macroscopic modelling techniques discussed in this work, a worthwhile goal for future research is to bridge these two levels of modelling; this would allow design and control decisions to be made with models that contain the best available knowledge of the microscopic chemistry.

Appendix A

Model-Predictive Control of Crystallizer Temperature

A cascade control system is used to control the crystallizer temperature. The secondary (slave) loop controls the jacket temperature by manipulating the flow ratio of the hot and cold streams to the jacket inlet. The operation of the batch crystallizer usually entails following a known and continuously changing temperature profile, but the response of the crystallizer to jacket temperature changes is sluggish and the jacket temperature is, of course, bounded. Therefore, the performance of a primary (master) controller that uses standard feedback would be limited—at best, the temperature would lag behind the set-point trajectory.

Model-predictive control (MPC) is able to improve performance over that of standard feedback by acting on model predictions of future errors between the temperature and the known set-point trajectory. Constraints on the manipulated variables (input constraints) can also be handled by MPC. As defined by Eaton and Rawlings [45], MPC is a control scheme that determines a manipulated variable profile that optimizes some open-loop performance objective on a time interval extending from the current time to the end of a prediction horizon.

As discussed by García and Morshedi [53], quadratic dynamic matrix control (QDMC) uses a linear step response model and a quadratic performance objective, and it explicitly incorporates input constraints. A QDMC controller is used as the primary-loop controller of the crystallizer temperature.

Letting y be the crystallizer temperature and u be the manipulated variable (the set point for the jacket temperature), a step response model can be expressed as

$$\begin{bmatrix} \tilde{y}(k+1) \\ \tilde{y}(k+2) \\ \vdots \\ \tilde{y}(k+p) \end{bmatrix} = \begin{bmatrix} a_1 & 0 & \cdots & 0 \\ a_2 & a_1 & & \vdots \\ \vdots & & \ddots & 0 \\ a_p & a_{p-1} & \cdots & a_{p-m+1} \end{bmatrix} \begin{bmatrix} \Delta u(k) \\ \Delta u(k+1) \\ \vdots \\ \Delta u(k+m-1) \end{bmatrix} + \begin{bmatrix} y^\star(k+1) \\ y^\star(k+2) \\ \vdots \\ y^\star(k+p) \end{bmatrix}$$

where k denotes the present sampling instant, p is the prediction horizon (the number of future sampling periods considered), m is the control horizon,

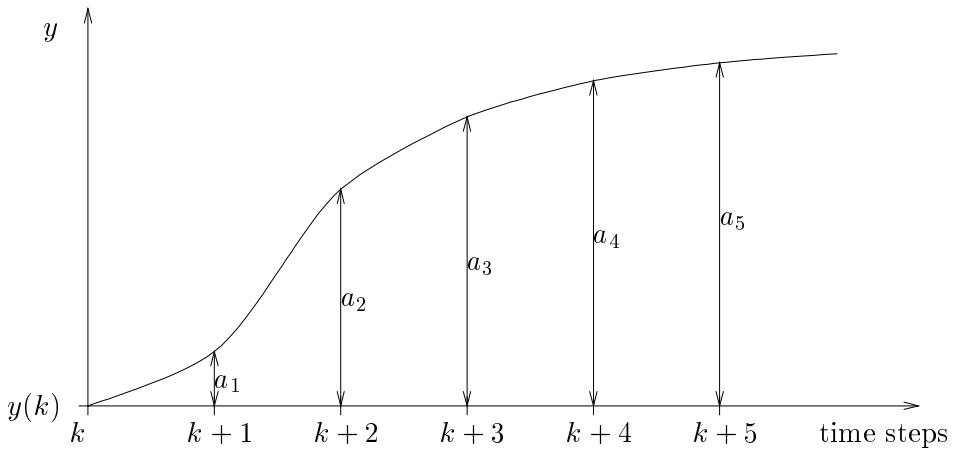

Figure A.1: Response of system to a unit step change in the input variable at the k^{th} sampling instant.

$\tilde{y}(k+i)$ is the model-predicted output i sampling intervals in the future, $\Delta u(i)$ is the input change implemented at the i^{th} sampling instant, and $y^{\star}(k+i)$ is the predicted output i sampling intervals in the future if no more control moves were made (i.e., if $\Delta u(k+i) = 0$ for $i = 0, 1, ...$). The a_i are step response coefficients, which can be obtained from the response of the system to a step change in the input as shown in Figure A.1.

To simplify the notation, let $\tilde{\mathbf{y}}$, $\mathbf{\Delta u}$, and $\mathbf{y}^{\star}$ represent the vectors of $\tilde{y}(i)$, $\Delta u(i)$, and $y^{\star}(i)$, respectively, and let $\mathbf{A}$ represent the matrix of step response coefficients (commonly referred to as the "dynamic matrix"). The step response model is then given by

$$\tilde{\mathbf{y}} = \mathbf{A}\mathbf{\Delta u} + \mathbf{y}^{\star}$$

Note that because there is no steady state for batch operation, the control horizon should be equal to the prediction horizon, making $\mathbf{A}$ a $p \times p$ matrix.

Representing the reference or set point trajectory as $\mathbf{y}_r$, the QDMC controller determines the input trajectory, $\mathbf{\Delta u}$, that minimizes

$$(\mathbf{y}_r - \tilde{\mathbf{y}})^T(\mathbf{y}_r - \tilde{\mathbf{y}}) + \mathbf{\Delta u}^T\mathbf{\Gamma}\mathbf{\Delta u}$$

subject to bounds on u. The matrix $\mathbf{\Gamma}$ is a penalty matrix on the control moves. Therefore, the QDMC problem can be posed as a quadratic programming (QP)

problem:

$$\begin{aligned} \min_{\mathbf{\Delta u}} \quad & \mathbf{c}^T\mathbf{\Delta u} + \tfrac{1}{2}\mathbf{\Delta u}^T\mathbf{H}\mathbf{\Delta u} \\ \text{subject to:} \quad & \begin{bmatrix} u_{\min} - u_{\text{curr}} \\ \vdots \\ u_{\min} - u_{\text{curr}} \end{bmatrix} \leq \mathbf{L}\mathbf{\Delta u} \leq \begin{bmatrix} u_{\max} - u_{\text{curr}} \\ \vdots \\ u_{\max} - u_{\text{curr}} \end{bmatrix} \end{aligned} \tag{QP2}$$

where

$$\mathbf{L} = \begin{bmatrix} 1 & & 0 \\ \vdots & \ddots & \\ 1 & \cdots & 1 \end{bmatrix}$$

$\mathbf{H} = \mathbf{A}^T\mathbf{A} + \mathbf{\Gamma}$, $\mathbf{c} = -\mathbf{A}^T(\mathbf{y}_r - \mathbf{y}^\star)$, and $u_{\min}$, $u_{\max}$, and u_{curr} are the minimum bound, maximum bound, and current value of the input, respectively. This QP problem is solved at each sampling period, and the first element of the newly computed $\mathbf{\Delta u}$ is implemented.

Before the solution of each QP problem, $\mathbf{y}^\star$ is updated in a two step process—first, the predicted dynamic response to the last input is determined:

$$\mathbf{y}^\star = \mathbf{y}^\star_{\text{old}} + \mathbf{A}_1\Delta u(k-1)$$

where $\mathbf{y}^\star_{\text{old}}$ is the previous value of $\mathbf{y}^\star$, $\mathbf{A}_1$ is the first column of $\mathbf{A}$, and $\Delta u(k-1)$ is the most recently-implemented control move. At this point, the first element of $\mathbf{y}^\star$ corresponds to the present time; to account for the horizon moving forward, the vector must be shifted by one, using extrapolation to obtain the last element.

Feedback is incorporated by estimating a disturbance and using it to update the model before the solution of each QP problem. The disturbance, d, is estimated at each sampling period as shown in Figure A.2 and is assumed to be constant over the prediction horizon. The disturbance can be included when updating $\mathbf{y}^\star$:

$$\mathbf{y}^\star = \mathbf{y}^\star_{\text{old}} + \mathbf{A}_1\Delta u(k-1) + d$$

The penalty matrix was chosen to be $\mathbf{\Gamma} = \gamma\mathbf{I}$, reducing the tuning of the primary controller to the selection of the penalty coefficient, γ, and the prediction/control horizon, p.

The selection of γ involves balancing performance and robustness—large values of γ lead to less aggressive but more robust control action. In light of the discussion provided by Shaw [148] about a problem similar to that of QP2,

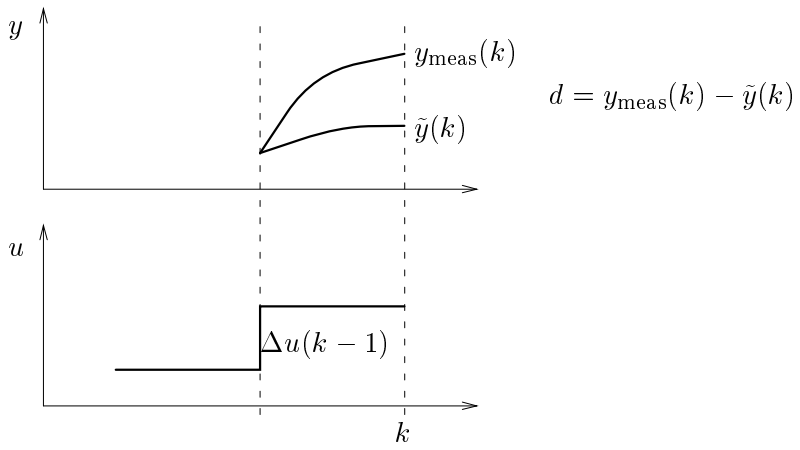

Figure A.2: Estimation of disturbance, d. k represents the present time. y_{meas} = measured value.

the eigenvalues of $\mathbf{A}^T\mathbf{A}$ can be used as a guide for the selection of γ; a value for γ that is one or two orders of magnitude less than the largest eigenvalue is a reasonable initial setting.

The choice of p is a tradeoff between robustness and computation time. This choice requires pragmatism; with the computational hardware available, p should be as large as possible such that the computation time is small when compared to the sampling interval.

The step response coefficients for the crystallizer temperature cascade control system were obtained from a model fit to step-test data; a linear first order model with deadtime was used. A least squares fit yielded the following estimates: gain = 0.8, time constant = 18.7 minutes, deadtime = 0.47 minutes. Figure A.3 shows the fit of this model to crystallizer temperature data corresponding to a -2°C step in the jacket temperature.

The performance of the control system with $\Delta t = 1$ minute, $p = 25$, and $\gamma = 0.01$ (the settings used for this study) is shown in Figure A.4. For the case shown, the primary controller output is constrained between 24.5°C and 30.5°C. Notice that this example illustrates two of the important features of a model-predictive controller—its ability to minimize the impact of active input constraints on performance, and its ability to incorporate information of the future and act accordingly.

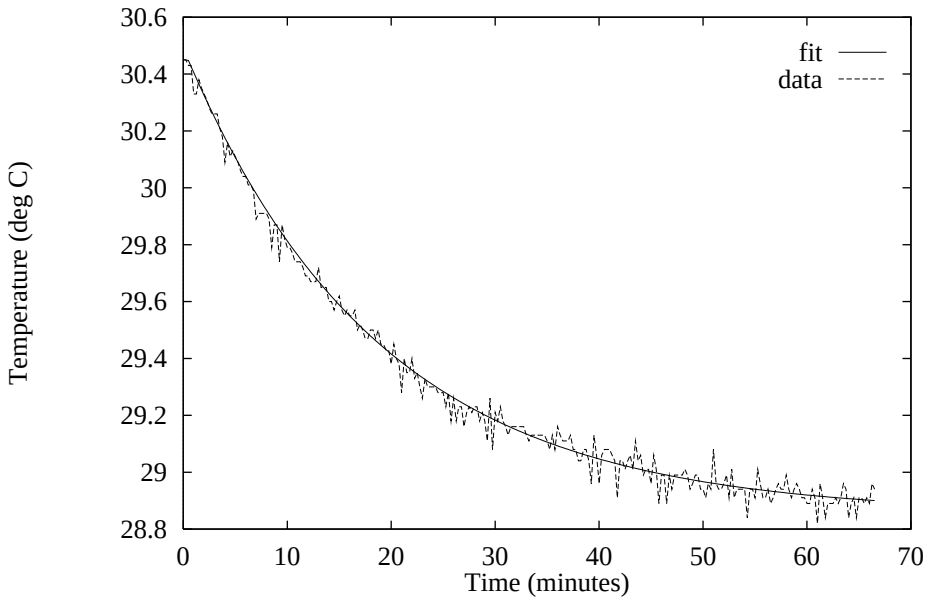

Figure A.3: Response of crystallizer temperature to a -2°C step in the jacket temperature. The fit of a first order model with deadtime is also shown.

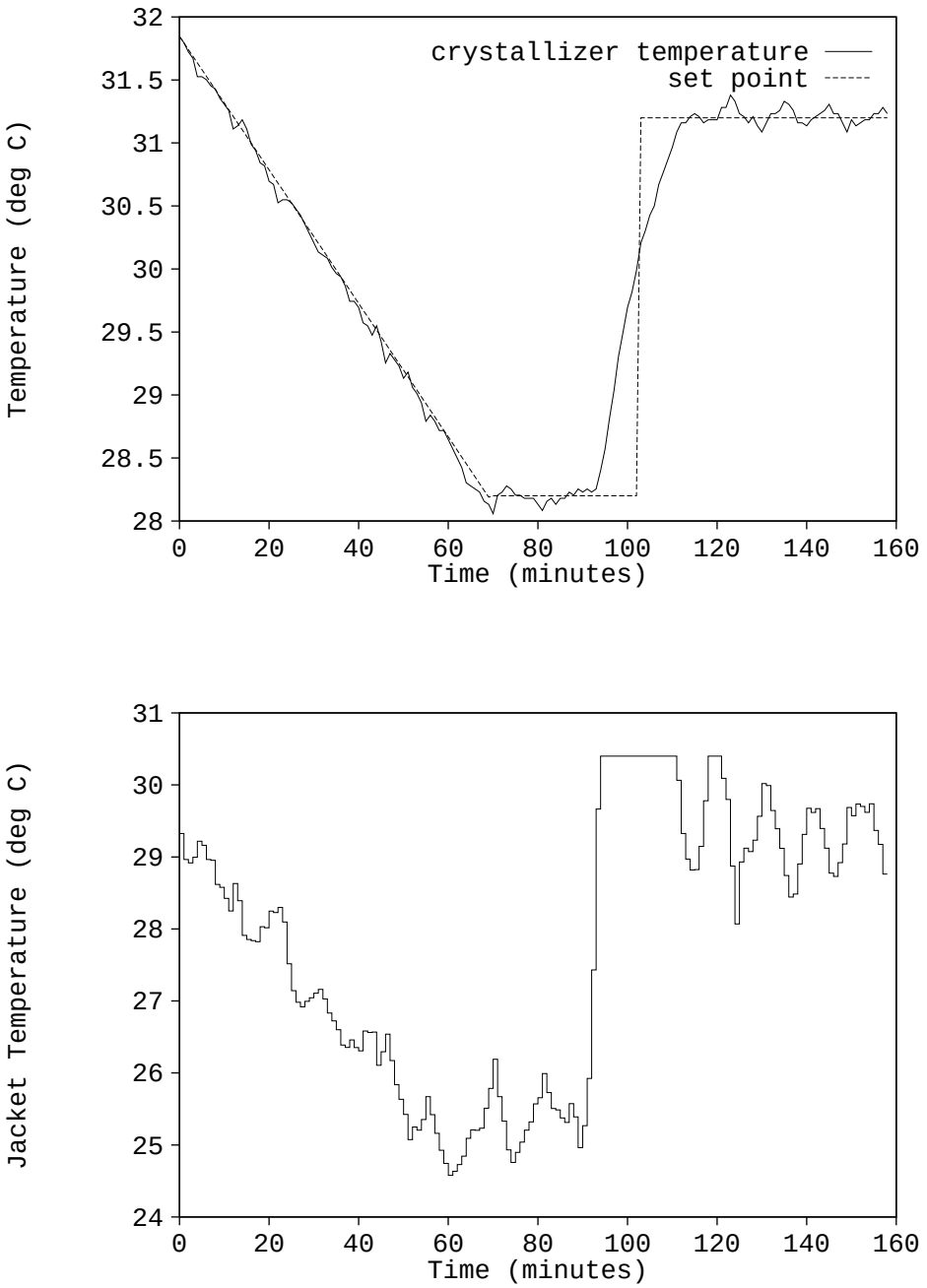

Figure A.4: Performance of the cascade control system with QDMC primary controller and PID secondary controller. The crystallizer jacket temperature (output of QDMC controller) is also shown; $u_{\min} = 24.5°$, $u_{\max} = 30.5°$

Appendix B

Mass and Energy Balances, and Population Balance Simplification

B.1 Mass Balance

The mass balance for the solute of a crystallization process is

$$\frac{d(V_c C)}{dt} = -\sum_k \varepsilon_k Q_k C_k - R \tag{B.1}$$

where V_c is the volume of the solids-free or continuous phase, V is the slurry volume, C is the concentration of the solute, ε is the solids-free volume fraction (V_c/V), Q is a volumetric flow rate (positive sign denotes flow out), the subscript k denotes the k^{th} stream, and R is the overall rate of mass transfer of solute from solution to crystals.
Using the definition of ε, Eq. B.1 can be written as

$$\frac{d(\varepsilon V C)}{dt} = -\sum_k \varepsilon_k Q_k C_k - R \tag{B.2}$$

To examine the term R, consider the crystallizer population balance:

$$\frac{\partial(fV)}{\partial t} + V\frac{\partial(Gf)}{\partial L} - VB^\circ\delta(L - L_0) + \sum_k Q_k f_k = 0 \tag{B.3}$$

Multiplying Eq. B.3 by L^j ($j = 1, 2, ...$), and integrating over all L,

$$\frac{d(V\mu_j)}{dt} + V\int_0^\infty \frac{\partial(Gf)}{\partial L}L^j dL - VB^\circ L_0^j + \sum_k Q_k \int_0^\infty f_k L^j dL = 0 \tag{B.4}$$

where μ_j is the j^{th} moment of the distribution.
Using integrating by parts,

$$\int_0^\infty \frac{\partial(Gf)}{\partial L}L^j dL = -j\int_0^\infty GfL^{j-1}dL \tag{B.5}$$

Substituting this into Eq. B.4,

$$\frac{d(V\mu_j)}{dt} = jV\int_0^\infty GfL^{j-1}dL + VB^\circ L_0^j - \sum_k Q_k \int_0^\infty f_k L^j dL \tag{B.6}$$

Note that $\rho_c k_v \mu_3$ is the mass of crystals per slurry volume, where ρ_c is the crystal density and k_v is the crystal volume shape factor. Therefore, assuming ρ_c and k_v are constant and letting M denote the mass of crystals in the crystallizer, Eq. B.6 becomes

$$\frac{dM}{dt} = \rho_c k_v 3V \int_0^\infty G f L^2 dL + \rho_c k_v V B^\circ L_0^3 - \rho_c k_v \sum_k Q_k \int_0^\infty f_k L^2 dL \quad \text{(B.7)}$$

The first two terms of Eq. B.7 are related to mass transfer from solution to crystals; the last term is the net rate of *flow* of crystals into the crystallizer. Therefore,

$$R = 3\rho_c k_v V \int_0^\infty G f L^2 dL + \rho_c k_v V B^\circ L_0^3 \quad \text{(B.8)}$$

B.2 Energy Balance

The energy balance for a crystallizer is

$$\frac{d}{dt}(\mathrm{U} + \mathrm{KE} + \mathrm{PE}) = -\sum_k \rho_k Q_k (U_k^\star + \mathrm{KE}_k^\star + \mathrm{PE}_k^\star) - H_{\text{ext}} + W \quad \text{(B.9)}$$

where U is the internal energy; KE and PE are the kinetic and potential energies, respectively; Q_k and ρ_k are the volumetric flow rate and density of the k^{th} streams, respectively; H_{ext} is the net heat removal rate (incorporating effects of cooling system, evaporation, loss to surroundings and energy input from physical mixing); W is the net rate of work performed on the system to transport fluid; the superscript $\star$ denotes per-unit-mass basis. It should be noted that the KE and PE terms are insignificant when any temperature change occurs.
Enthalpy is defined as follows

$$H = U + PV \quad \text{(B.10)}$$

where P is pressure, and V is volume. On a per-unit-mass basis,

$$H^\star = U^\star + \frac{P}{\rho} \quad \text{(B.11)}$$

An expression for W is given below

$$W = \sum_k Q_k P_k \quad \text{(B.12)}$$

Substituting Eq. B.12 into Eq. B.9 and neglecting KE and PE,

$$\frac{dU}{dt} = -\sum_k \rho_k Q_k \left(U_k^\star + \frac{P_k}{\rho_k} \right) - H_{\text{ext}} \tag{B.13}$$

Substituting definitions for enthalpy and specific enthalpy,

$$\frac{dH}{dt} - \frac{d(PV)}{dt} = -\sum_k \rho_k Q_k H_k^\star(T_k) - H_{\text{ext}} \tag{B.14}$$

Note that the term $d(PV)/dt$ is negligible for cooling crystallization, because it is insignificant for liquid systems; however, to be sufficiently general to include evaporative crystallization, it is not dropped here.

To express the energy balance in terms of temperature, the following expression can be used to relate enthalpies to the initial temperature of the crystallizer:

$$H_k^\star(T_k) = H_k^\star(T_0) + \int_T^{T_k} c_{p_k} dT \tag{B.15}$$

where $H_k^\star(T_0)$ is the specific enthalpy of the k^{th} stream evaluated at the initial crystallizer temperature.

Taking c_{p_k} to be independent of temperature (a reasonable assumption over small temperature ranges), and substituting Eq. B.15 into Eq. B.14,

$$\frac{dH}{dt} = \frac{d(PV)}{dt} - \sum_k \rho_k Q_k c_{p_k} (T_k - T_0) - \sum_k \rho_k Q_k H_k^\star(T) - H_{\text{ext}} \tag{B.16}$$

Noting that H is a function of composition and temperature, and using the definition of heat capacity ($\rho V c_p = \partial H / \partial T$),

$$\frac{dH}{dt} = \rho V c_p \frac{dT}{dt} + \sum_i \tilde{H}_i \frac{dn_i}{dt} \tag{B.17}$$

where $\tilde{H}_i$ is the partial molar enthalpy of the i^{th} component in the crystallizer and n_i is the number of moles of the i^{th} component.

Using the mass balance to cast n_i in terms of concentrations, substituting Eq. B.17 into Eq. B.16, and simplifying, one obtains

$$\rho V c_p \frac{dT}{dt} = \frac{d(PV)}{dt} - \sum_k \rho_k Q_k c_{p_k} (T_k - T_0) - \Delta H_c R - H_{\text{ext}} \tag{B.18}$$

where R is the rate of crystallization and ΔH_c is the enthalpy change of crystallization (heat of crystallization); ΔH_c is negative for exothermic crystallization. This expression also requires the assumption that the contribution

related to the difference between partial molar enthalpy of a given species at a given temperature in two different mixtures is negligible with respect to the other terms.
From Section B.1, the rate of crystallization is

$$R = 3\rho_c k_v V \int_0^\infty GfL^2 dL + \rho_c k_v V B^\circ L_0^3$$

B.3 Simplification of Population Balance

The population balance for a crystallizer is

$$\frac{\partial(fV)}{\partial t} + V\frac{\partial(Gf)}{\partial L} = VB^\circ\delta(L - L_0) - \sum_k Q_k f_k \tag{B.19}$$

Because the term involving B° acts only at $L = L_0$, this can be written as

$$\frac{\partial(fV)}{\partial t} + V\frac{\partial(Gf)}{\partial L} = -\sum_k Q_k f_k \tag{B.20}$$

with an appropriate boundary condition. The procedure for determining the boundary condition simply involves the integration of Eq. B.19 over L from L_0^- to L_0^+ (just below to just above L_0).
Clearly,

$$\int_{L_0^-}^{L_0^+} B^\circ\delta(L - L_0)dL = B^\circ$$

It is also obvious that

$$\int_{L_0^-}^{L_0^+} \frac{\partial(fV)}{\partial t}dL = 0 \qquad \text{and} \qquad \int_{L_0^-}^{L_0^+} Q_k f_k dL = 0$$

Therefore, the result of the integration of Eq. B.19 is

$$\int_{L_0^-}^{L_0^+} \frac{\partial(Gf)}{\partial L}dL = B^\circ \tag{B.21}$$

There is a jump discontinuity in Gf: at L_0^-, $Gf = 0$; at L_0^+, $Gf = G|_{L_0} f(L_0, t)$. Therefore, the derivative of Gf with respect to L is a delta function with "strength" $G|_{L_0} f(L_0, t)$. Using this fact with Eq. B.21 leads to the desired boundary condition:

$$f(L_0, t) = \frac{B^\circ}{G|_{L=L_0}} \tag{B.22}$$

Appendix C

Physical Properties for Potassium Nitrate–Water System

The solubility of KNO_3 in H_2O is given by

$$\hat{C}_{\text{sat}} = 0.1286 + 0.00588T + 0.0001721T^2 \quad (\text{g KNO}_3/\text{g H}_2\text{O})$$

where T is in °C. This is a fit to solubility data in the 20–40°C temperature range [115].

The heat of crystallization of KNO_3 from a solution of KNO_3 and H_2O is a function of the solution concentration; this dependence can be characterized by the following fit to data [9]:

$$\Delta H_c = -85.75 + 92.82\hat{C} - 99.97\hat{C}^2 \quad (\text{cal/g})$$

The heat capacity of a solution of KNO_3 and H_2O depends on the concentration and temperature of the solution, but is not a strong function of temperature. The relationship between c_p and concentration is well characterized [168] and can be expressed as

$$c_p = 0.9971 - 1.06\left(\frac{\hat{C}}{1+\hat{C}}\right) + 1.007\left(\frac{\hat{C}}{1+\hat{C}}\right)^2 \quad (\text{cal/g}^\circ\text{C})$$

It is assumed that the heat capacity of a slurry is equal to that of a solution of the concentration of the continuous phase of the slurry.
The density of KNO_3 crystals is

$$\rho_c = 2.11 \text{ g/cm}^3$$

After microscopic analysis, the shape factors were taken to be:

$$k_v = 1 \qquad k_a = 6$$

Step tests of the jacket cooling water temperature were performed to characterize the heat transfer of the crystallizer vessel used in this study. It was found that

$$UA = 216 \frac{\text{cal}}{\text{min}^\circ\text{C}}$$

where U and A are the heat transfer coefficient and area, respectively.

Bibliography

[1] Abegg, C. F., J. D. Stevens, and M. A. Larson. Crystal size distributions in continuous crystallizers when growth rate is size dependent. *AIChE J.*, 14(1):118–122, January 1968.

[2] Ajinkya, M. B. and W. H. Ray. On the optimal operation of crystallization processes. *Chem. Eng. Commun.*, 1:181–186, 1974.

[3] Alper, J. S. and R. I. Gelb. Standard errors and confidence intervals in nonlinear regression: Comparison of Monte Carlo and parametric statistics. *J. Phys. Chem.*, 94:4747–4751, 1990.

[4] Bard, Y. *Nonlinear Parameter Estimation.* Academic Press, New York, 1974.

[5] Beckman, J. R. and A. D. Randolph. Crystal size distribution dynamics in a classified crystallizer: Part II. Simulated control of crystal size distribution. *AIChE J.*, 23(4):510–520, July 1977.

[6] Behnken, D., J. Horowitz, and S. Katz. Particle growth processes. *Ind. Eng. Chem. Fundam.*, 2(3):212–216, August 1963.

[7] Berglund, K. A. and M. A. Larson. Modeling of growth rate dispersion of citric acid monohydrate in continuous crystallizers. *AIChE J.*, 30:280–287, 1984.

[8] Bhat, H. L., J. N. Sherwood, and T. Shripathi. The influence of stress, strain and fracture of crystals on the crystal growth process. *Chem. Eng. Sci.*, 42(4):609–618, 1987.

[9] Bichowsky, F. R. and F. D. Rossini, editors. *The Thermochemistry of the Chemical Substances.* Reinhold Publishing, 1936.

[10] Biegler, L. T., J. J. Damiano, and G. E. Blau. Nonlinear parameter estimation: a case study comparison. *AIChE J.*, 32(1):29–45, 1986.

[11] Bohlin, M. and Å. C. Rasmuson. Application of controlled cooling and seeding in batch crystallization. *Can. J. Chem. Eng.*, 70:120–126, 1992.

[12] Botsaris, G. D. Secondary nucleation—a review. In Mullin, J. W., editor, *Industrial Crystallization*, New York, 1976. Plenum Press.

[13] Boxman, A. *Particle Size Measurement for Control of Industrial Crystallizers.* PhD thesis, Delft University of Technology, 1992.

[14] Brook, R. J. and G. C. Arnold. *Applied Regression Analysis and Experimental Design.* Marcel Dekker, Inc., New York, 1985.

[15] Brown, D. J. and P. G. Felton. Direct measurement of concentration and size for particles of different shapes using laser light diffraction. *Chem. Eng. Res. Des.*, 63:125–132, 1985.

[16] Brown, D. J., T. Gregory, and E. J. Weatherby. The development of online measurement of crystal growth by laser diffraction. In *Control and Instrumentation—The Changing Scene, Proceedings of The Institute of Measurement and Control Conference*, Harrogate, November 1985.

[17] Bryson, A. E. and Y. Ho. *Applied Optimal Control.* Hemisphere Publishing, New York, 1975.

[18] Budz, J., A. G. Jones, and J. W. Mullin. On the shape–size dependence of potassium sulfate crystals. *Ind. Eng. Chem. Res.*, 26:820–824, 1987.

[19] Budz, J. A. Kinetic measurements in crystallizing systems. Seminar presented at Tennessee Eastman Co., Kingsport, Tennessee, August 1987.

[20] Bunville, L. G. Commercial instrumentation for particle size analysis. In Barth, H. G., editor, *Modern Methods of Particle Size Analysis*, chapter 1, pages 1–42. John Wiley & Sons, 1984.

[21] Burton, W. K., N. Cabrera, and F. C. Frank. The growth of crystals and the equilibrium structure of their surfaces. *Phil. Trans. Roy. Soc.*, 243:299–358, June 1951.

[22] Canning, T. F. and A. D. Randolph. Some aspects of crystallization theory: Systems that violate McCabe's delta L law. *AIChE J.*, 13(1):5–10, 1967.

[23] Caracotsios, M. and W. E. Stewart. Sensitivity analysis of initial value problems with mixed ODEs and algebraic equations. *Comput. Chem. Eng.*, 9(4):359–365, 1985.

[24] Chang, C. and M. A. Epstein. Identification of batch crystallization control strategies using characteristic curves. *AIChE Symp. Ser.*, 78(215):68–75, 1982.

[25] Chang, C. and M. A. F. Epstein. Simulation studies of a feedback control strategy for batch crystallizers. *AIChE Symp. Ser.*, 83(253):110–119, 1987.

[26] Chen, M. and M. A. Larson. Crystallization kinetics of calcium nitrate tetrahydrate from MSMPR crystallizer. *Chem. Eng. Sci.*, 40(7):1287–1294, 1985.

[27] Chianese, A., S. D. Cave, and B. Mazzarotta. Investigation on some operating factors influencing batch cooling crystallization. In Jančić, S. J. and E. J. de Jong, editors, *Industrial Crystallization 84*, pages 443–446. Elsevier Science, 1984.

[28] Chow, L. and C. Tien. Inversion techniques for determining the droplet size distribution in clouds: Numerical examination. *Applied Opt.*, 15(2):378–383, 1976.

[29] Clontz, N. A. and W. L. McCabe. Contact nucleation of magnesium sulfate heptahydrate. *AIChE Symp. Ser.*, 67(110):6–17, 1971.

[30] Clydesdale, G., R. Docherty, and K. J. Roberts. HABIT—a program for predicting the morphology of molecular crystals. *Comput. Phys. Commun.*, 64:311–328, 1991.

[31] Crump, J. G. and J. H. Seinfeld. A new algorithm for inversion of aerosol size distribution data. *Aerosol Science and Technology*, 1:15–34, 1982.

[32] Curl, R. Dispersed phase mixing: I. Theory and effect in simple reactors. *AIChE J.*, 9:175, March 1963.

[33] Dave, J. V. Coefficients of the Legendre and Fourier series for the scattering functions of spherical particles. *Applied Opt.*, 9(8):1888–1896, August 1970.

[34] deBoer, G. B. J., C. deWeerd, D. Thoenes, and H. W. J. Goossens. Laser diffraction spectrometry: Fraunhofer diffraction versus Mie scattering. *Part. Charact.*, 4:14–19, 1987.

[35] Delves, L. M. and J. L. Mohamed. *Computational Methods for Integral Equations*. Cambridge University Press, Cambridge, Massachusetts, 1985.

[36] Denn, M. M. *Process Modeling*. Longman, White Plains, NY, 1986.

[37] Docherty, R., G. Clydesdale, K. J. Roberts, and P. Bennema. Application of bravis-friedel-donnay-harker, attachment energy and ising models to predicting and understanding the morphology of molecular crystals. *J. Phys. D: Appl. Phys.*, 24:89–99, 1991.

[38] Docherty, R., K. J. Roberts, and E. Dowty. MORANG—a computer program designed to aid in the determinations of crystal morphology. *Comput. Phys. Commun.*, 51:423–430, 1988.

[39] Dodge, L. G. Change of calibration of diffraction-based particle sizers in dense sprays. *Optical Eng.*, 23(5):626–630, September 1984.

[40] Donaldson, J. R. and R. B. Schnabel. Computational experience with confidence regions and confidence intervals for nonlinear least squares. *Technometrics*, 29(1):67–82, 1987.

[41] Dongarra, J. J., C. B. Moler, J. R. Bunch, and G. W. Stewart. *LINPACK User's Guide*. SIAM, Philadelphia, 1979.

[42] E. Dan Hirleman, V. Oechsle, N. A. C. Response characteristics of laser diffraction particle size analyzers: Optical sample volume extent and lens effects. *Optical Eng.*, 23(5):610–619, September 1984.

[43] Eakman, J. M., A. G. Fredrickson, and H. M. Tsuchiya. Statistics and dynamics of microbial cell populations. *Chem. Eng. Progr. Symp. Ser.*, 62:37–49, 1966.

[44] Eaton, J. W. and J. B. Rawlings. Feedback control of chemical processes using on-line optimization techniques. *Comput. Chem. Eng.*, 14(4/5):469–479, 1990.

[45] Eaton, J. W. and J. B. Rawlings. Model-predictive control of chemical processes. *Chem. Eng. Sci.*, 47(4):705–720, 1992.

[46] Eaton, J. W., J. B. Rawlings, and T. F. Edgar. Model-predictive control and sensitivity analysis for constrained nonlinear processes. In McAvoy, T. J., Y. Arkun, and E. Zafiriou, editors, *Proceedings of the 1988 IFAC Workshop on Model Based Process Control*, pages 129–135, Oxford, 1989. Pergamon Press.

[47] Estrin, J. Precipitation processes. In Myerson, A. S., editor, *Industrial Crystallization—Theory and Practice*, pages 131–149. Butterworths, 1992.

[48] Fan, L. T., S. T. Chou, and J. P. Hsu. Transient analysis of crystallization: Effect of the size-dependent residence time of classified product removal. *AIChE Symp. Ser.*, 83(253):120–129, 1987.

[49] Fantini, E., L. Tognotti, and A. Tonazzini. Drop size distribution in sprays by image processing. *Comput. Chem. Eng.*, 14(11):1201–1211, 1990.

[50] Felton, P. G. and D. J. Brown. Measurement of crystal growth by laser light diffraction. *I. Chem. E. Symp. Series*, 59:7:1/1–7:1/9, 1980.

[51] Friedlander, S. K. *Smoke, Dust, and Haze: Fundamentals of Aerosol Behavior*. Wiley, New York, 1977.

[52] Fymat, A. L. and K. D. Mease. Mie forward scattering: Improved semiempirical approximation with application to particle size distribution inversion. *Appl. Opt.*, 20:194–198, 1981.

[53] García, C. E. and A. M. Morshedi. Quadratic programming solution of dynamic matrix control (QDMC). *Chem. Eng. Commun.*, 46:73–87, 1986.

[54] Garside, J. Industrial crystallization from solution. *Chem. Eng. Sci.*, 40(1):3–26, 1985.

[55] Garside, J. and R. Davey. Secondary contact nucleation: Kinetics, growth and scale-up. *Chem. Eng. Commun.*, 4:393–424, 1980.

[56] Garside, J. and J. W. Mullin. Continuous measurement of solution concentration in a crystalliser. *Chem. and Ind.*, pages 2007–2008, November 1966.

[57] Garside, J., G. Webster, R. J. Davey, and A. J. Ruddick. The influence of stress, strain and fracture of crystals on the crystal growth process. In Jančić, S. J. and E. J. de Jong, editors, *Industrial Crystallization 84*, pages 459–462, Amsterdam, 1984. Elsevier Science Publishers.

[58] Garside, J. Advances in the characterisation of crystal growth. *AIChE Symp. Ser.*, 80(240):23–38, 1984.

[59] Garside, J., L. G. Gibilaro, and N. S. Tavare. Evaluation of crystal growth kinetics from desupersaturation curve using initial time derivatives. *Chem. Eng. Sci.*, 37:1625–1628, 1982.

[60] Garside, J., V. R. Phillips, and M. B. Shah. On size-dependent crystal growth. *Ind. Eng. Chem. Fundam.*, 15(3):230–233, 1976.

[61] Garside, J. and M. B. Shah. Crystallization kinetics from MSMPR crystallizers. *Ind. Eng. Chem. Proc. Des. Dev.*, 19:509–514, 1980.

[62] Gill, P. E., W. Murray, M. A. Saunders, and M. H. Wright. User's guide for SOL/NPSOL (Version 4.0): A Fortran package for nonlinear programming, technical report SOL 86-2. Technical report, Systems Optimization Laboratory, Department of Operations Research, Stanford University, 1986.

[63] Girolami, M. W. and R. W. Rousseau. Size-dependent crystal growth—a manifestation of growth rate dispersion in the potassium alum-water system. *AIChE J.*, 31(11):1821–1828, 1985.

[64] Green, D. A., 1988. November/December Du Pont Magazine.

[65] Griffiths, H. Mechanical crystallisation. *Journal of The Society of Chemical Industry Transactions*, 44:7T–18T, 1925.

[66] Grootscholten, P. A. M., B. G. M. de Leer, E. J. de Jong, and C. Asselbergs. Factors affecting secondary nucleation rate of sodium choride in an evaporative crystallizer. *AIChE J.*, 28:728–737, 1982.

[67] Gupta, G. and D. C. Timm. Predictive/corrective control for continuous crystallization. *Chem. Eng. Progr. Symp. Ser.*, 67(110):121–128, 1971.

[68] Han, C. D. A control study on isothermal mixed crystallizers. *Ind. Eng. Chem. Proc. Des. Dev.*, 8(2):150–158, April 1969.

[69] Hanzevack, E. L., S. R. McNeill, C. B. Bowers, and C. H. Ju. An inexpensive experimental system for study of two phase flow by laser image processing. *Chem. Eng. Commun.*, 65:161–167, 1988.

[70] Hartel, R. W., K. A. Berglund, S. M. Gwynn, P. M. Schierholz, and V. G. Murphy. Crystallization kinetics for the sucrose–water system. *AIChE Symp. Ser.*, 76(193):65–72, 1980.

[71] Helt, J. E. and M. A. Larson. Effect of temperature on the crystallization of potassium nitrate by direct measurement of supersaturation. *AIChE J.*, 23(6):822–830, 1977.

[72] Hidy, G. *Aerosols: An Industrial and Environmental Science*. Pergamon, Orlando, 1984.

[73] Hidy, G. N. and J. R. Brock. *The Dynamics of Aerocolloidal Systems.* Pergamon, New York, 1970.

[74] Hirleman, E. D. Modeling of multiple scattering effects in Fraunhofer diffraction particle size analysis. *Part. Charact.*, 5:57–65, 1988.

[75] Hoerl, A. E. and R. W. Kennard. Ridge regression–1980: Advances, algorithms, and applications. *Am. J. Math. Man.. Sci.*, 1:5–83, 1981.

[76] Hsu, J. and L. Fan. Transient analysis of crystallization: Effect of the size dependent growth rate. *Chem. Eng. Commun.*, 56:19–40, 1987.

[77] Hsu, J. P., L. T. Fan, and S. T. Chou. Transient analysis of crystallization: Effect of the initial size distribution. *Chem. Eng. Commun.*, 69:95–114, 1988.

[78] Hulburt, H. M. and S. Katz. Some problems in particle technology: A statistical mechanical formulation. *Chem. Eng. Sci.*, 19:555–574, 1964.

[79] Jager, J., S. de Wolf, W. Klapwijk, and E. J. de Jong. A new design for on-line product-slurry measurements. In Nývlt, J. and S. Žáček, editors, *Industrial Crystallization 87*, pages 415–418, Bechyně, Czechoslovakia, 1987. Elsevier Science Publishers.

[80] Jager, J., H. J. M. Kramer, E. J. de Jong, S. de Wolf, O. H. Bosgra, A. Boxman, H. G. Merkus, and B. Scarlett. Control of industrial crystallizers. *Powder Tech.*, 69(1):11–20, January 1992.

[81] Jančić, S. and J. Garside. A new technique for accurate crystal size distribution analysis in an MSMPR crystallizer. In Mullin, J. W., editor, *Industrial Crystallization*, New York, 1976. Plenum Press.

[82] Jang, S.-S., B. Joseph, and H. Mukai. Comparison of two approaches to on-line parameter and state estimation of nonlinear systems. *Ind. Eng. Chem. Proc. Des. Dev.*, 25:809–814, 1986.

[83] Janse, A. H. and E. J. de Jong. The occurence of growth dispersion and its consequences. In Mullin, J. W., editor, *Industrial Crystallization*, New York, 1976. Plenum Press.

[84] Johansen, T. A. and B. A. Foss. Representing and learning unmodelled dynamics with neural network memories. In *Proceedings of the 1992 American Control Conference*, pages 3037–3043, 1992.

[85] Johnson, R. T., R. W. Rousseau, and W. L. McCabe. Factors affecting contact nucleation. *AIChE Symp. Ser.*, 68(121):31–41, 1972.

[86] Jones, A. G. Optimal operation of a batch cooling crystallizer. *Chem. Eng. Sci.*, 29:1075–1087, 1974.

[87] Jones, A. G. Design and performance of batch crystallizers. In *Institution of Chemical Engineers: North Western Branch Papers No. 2*, pages 4.1–4.11, 1982.

[88] Jones, A. G., J. Budz, and J. W. Mullin. Crystallization kinetics of potassium sulfate in an MSMPR agitated vessel. *AIChE J.*, 32(12):2002–2008, 1986.

[89] Jones, A. G., A. Chianese, and J. W. Mullin. Effect of fines destruction on batch cooling crystallization of potassium sulphate solutions. In Jančić, S. J. and E. J. de Jong, editors, *Industrial Crystallization 84*, pages 191–195, Amsterdam, 1984. Elsevier Science Publishers.

[90] Jones, A. G. and J. W. Mullin. Programmed cooling crystallization of potassium sulphate solutions. *Chem. Eng. Sci.*, 29:105–118, 1974.

[91] Jones, A. R. Error contour charts relevant to particle sizing by forward-scattered lobe methods. *J. Phys. D: Appl. Phys.*, 10:L163–L165, 1977.

[92] Kane, S. G., T. W. Evans, P. L. T. Brian, and A. F. Sarofim. Determination of the kinetics of secondary nucleation in batch crystallizers. *AIChE J.*, 20(5):855–862, 1974.

[93] Karpinski, P., J. Budz, and Z. Naruc. Effect of seeding moment on quality of CSD from batch cooling crystallizer. In Belina, D., editor, *Science Papers of the Institute of Chemical Engineering and Heat Systems*, pages 172–179, Book No. 38, Symposium No. 5, Wroclaw, Poland, March 21–25 1980. Technical University of Wroclaw, Wroclaw.

[94] Karpinski, P. H. Crystallization as a mass transfer phenomenon. *Chem. Eng. Sci.*, 35:2321–2324, 1980.

[95] Kramer, M. A., M. L. Thompson, and P. M. Bhagat. Embedding theoretical models in neural networks. In *Proceedings of the 1992 American Control Conference*, pages 475–479, 1992.

[96] Kwakernaak, H. and R. Sivan. *Linear Optimal Control Systems*. John Wiley and Sons, New York, 1972.

[97] Landau, L. D. and E. M. Lifshitz. *Fluid Mechanics*. Pergamon Press, New York, 1959.

[98] Larson, M. A. Advances in the characterization of crystal nucleation. *AIChE Symp. Ser.*, 80(240):39–44, 1984.

[99] Lieberman, A. On-line particle counting for crystallizer operation control. *AIChE Symp. Ser.*, 78(215):76–80, 1982.

[100] Liebman, M., T. Edgar, and L. Lasdon. Efficient data reconciliation and estimation for dynamic processes using nonlinear programming techniques. *Comput. Chem. Eng.*, 16(10/11):963–986, 1992.

[101] Meenan, P., K. J. Roberts, J. N. Sherwood, and K. R. Yuregir. Understanding and controlling the crystal morphology of some ionic crystals. *Powder Tech.*, 65(1-3):219–225, 1991.

[102] Meyer, P. and N. Chigier. Dropsize measurements using a malvern 2200 particle sizer. *Atomis. Spray Tech.*, 2:261–298, 1986.

[103] Mie, G. Beitrage zur Optik über Medien speziell kolloidaler Metallösungen. *Ann. Phys.*, 25:377–445, 1908.

[104] Morari, M. Some comments on the optimal operation of batch crystallizers. *Chem. Eng. Commun.*, 4:167–171, 1980.

[105] Mullin, J. W. and C. J. Leci. Desupersaturation of seeded citric acid solutions in a stirred vessel. *AIChE Symp. Ser.*, 68(121):8–20, 1972.

[106] Mullin, J. W. and J. Nývlt. Programmed cooling of batch crystallizers. *Chem. Eng. Sci.*, 26:369–377, 1971.

[107] Myerson, A. S. Crystallization research in the 1990s: An overview. In Myerson, A. S. and K. Toyokura, editors, *Crystallization as a Separations Process*, pages 1–15. American Chemical Society, 1990.

[108] Myerson, A. S. and R. Ginde. Crystals, crystal growth, and nucleation. In Myerson, A. S., editor, *Industrial Crystallization—Theory and Practice*. Butterworths, 1992.

[109] Myerson, A. S. and M. Saska. Calculation of crystal habit and solvent-accessible areas of sucrose and adipic acid crystals. In Myerson, A. S. and K. Toyokura, editors, *Crystallization as a Separations Process*, pages 55–71. American Chemical Society, 1990.

[110] Nývlt, J. and M. Broul. Kinetic exponents in crystallization and the accuracy of their determination. *International Chem. Eng.*, 22:543–548, 1982.

[111] Nývlt, J. and S. Žáček. Possible inaccuracies involved in the crystal population balance method and their elimination. *Cryst. Res. Tech.*, 16(7):807–814, 1981.

[112] Ou, S. and J. Seader. Contribution of multiple scattering to light transmittance by a collimated beam. *Comput. Chem. Eng.*, 11(6):757–761, 1987.

[113] Palwe, B., M. Chivate, and N. Tavare. Growth kinetics of ammonium nitrate crystals in a draft tube baffled batch crystallizer. *Ind. Eng. Chem. Proc. Des. Dev.*, 24:914–919, 1985.

[114] Patwardhan, A. A., J. B. Rawlings, and T. F. Edgar. Nonlinear model predictive control. *Chem. Eng. Commun.*, 87:123–141, 1990.

[115] Perry, R. H., D. W. Green, and J. O. Maloney, editors. *Perry's Chemical Engineer's Handbook*. McGraw-Hill Book Company, New York, 6th edition, 1984.

[116] Petzold, L. R. A description of DASSL: A differential-algebraic system solver. In Stepleman, R. S., editor, *Scientific Computing*, pages 65–68, Amsterdam, 1983. North-Holland.

[117] Phillips, D. L. A technique for the numerical solution of certain integral equations of the first kind. *J. Assoc. Comp. Mach.*, 9:84–97, 1962.

[118] Psichogios, D. C. and L. H. Ungar. A hybrid neural network-first principles approach to process modeling. *AIChE J.*, 38(10):1499–1511, 1992.

[119] Qian, R.-Y., Z. Chen, H. Ni, Z. Fan, and F. Cai. Crystallization kinetics of potassium chloride from brine and scale-up criterion. *AIChE J.*, 33(10):1690–1697, 1987.

[120] Qiu, Y. and Å. C. Rasmuson. Nucleation and growth of succinic acid in a batch cooling crystallizer. *AIChE J.*, 37(9):1293–1304, 1991.

[121] Ramkrishna, D. Solution of population balance equations. *Chem. Eng. Sci.*, 26:1136–1139, 1971.

[122] Ramkrishna, D. On problem-specific polynomials. *Chem. Eng. Sci.*, 28:1362–1365, 1973.

[123] Ramkrishna, D. Statistical models of cell populations. In Ghose, T. K., A. Fiechter, and N. Blakebrough, editors, *Advances in Biochemical Engineering*, volume 11, page 1, 1979.

[124] Ramkrishna, D. The status of population balances. *Reviews in Chemical Engineering*, 3(1):49–95, 1985.

[125] Randolph, A. D. and M. A. Larson. Transient and steady-state size distributions in continuous mixed suspension crystallizers. *AIChE J.*, 8(5):639–645, 1962.

[126] Randolph, A. D. and E. T. White. Modeling size dispersion in the prediction of crystal-size distribution. *Chem. Eng. Sci.*, 32:1067–1076, 1977.

[127] Randolph, A. D. CSD dynamics, stability, and control (a review paper). *AIChE Symp. Ser.*, 76(193):1–5, 1980.

[128] Randolph, A. D., L. Chen, and A. Tavana. Feedback control of CSD in a KCl crystallizer with fines dissolving. AIChE 1989 Spring Annual Meeting, New Orleans, LA, April 1986.

[129] Randolph, A. D. and M. A. Larson. *Theory of Particulate Processes.* Academic Press, San Diego, second edition, 1988.

[130] Randolph, A. D. and C. C. D. Low. Some attempts at CSD control utilizing on-line measurement of nucleation rate. In Jančić, S. J. and E. J. de Jong, editors, *Industrial Crystallization 81*, pages 29–34, Amsterdam, 1981. North-Holland Publishing Company.

[131] Randolph, A. D., E. T. White, and C.-C. D. Low. On-line measurement of fine-crystal response to crystallizer disturbances. *Ind. Eng. Chem. Proc. Des. Dev.*, 20:496–503, 1981.

[132] Rawlings, J. B., S. M. Miller, and W. R. Witkowski. Model identification and control of solution crystallization processes: A review. *Ind. Eng. Chem. Res.*, 32(7):1275–1296, July 1993.

[133] Rawlings, J. B. and W. H. Ray. Stability of continuous emulsion polymerization reactors: a detailed model analysis. *Chem. Eng. Sci.*, 42(11):2767–2777, 1987.

[134] Rawlings, J. B. and W. H. Ray. The modelling of batch and continuous emulsion polymerization reactors. Part I: Model formulation and sensitivity to parameters. *Polymer Eng. & Sci.*, 28:237–256, 1988.

[135] Rawlings, J. B. and W. H. Ray. The modelling of batch and continuous emulsion polymerization reactors. Part II: Comparison with experimental data from continuous stirred tank reactors. *Polymer Eng. & Sci.*, 28:257–273, 1988.

[136] Rawlings, J. B. and W. H. Ray. Emulsion polymerization reactor stability: Simplified model analysis. *AIChE J.*, 33(10):1663–1677, October 1987.

[137] Riebel, U., V. Kofler, and F. Löffler. Control of supersaturation in instationary suspension crystallization. In Mersmann, A., editor, *Industrial Crystallization 90*, pages 595–599, Amsterdam, 1990.

[138] Ring, T. A. Kinetic effects on particle morphology and size distribution during batch precipitation. *Powder Tech.*, 65:195–206, 1991.

[139] Rippin, D. W. T. Statistical methods for experimental planning in chemical engineering. *Comput. Chem. Eng.*, 12:109–116, 1988.

[140] Rohani, S. and K. Paine. Measurement of solids concentration of a soluble compound in a saturated slurry. *Can. J. Chem. Eng.*, 65:163–165, 1987.

[141] Rohani, S. and J. R. Bourne. Self-tuning control of crystal size distribution in a cooling batch crystallizer. *Chem. Eng. Sci.*, 45(12):3457–3466, 1990.

[142] Rohani, S., N. S. Tavare, and J. Garside. Control of crystal size distribution in a batch cooling crystallizer. *Can. J. Chem. Eng.*, 68:260–267, April 1990.

[143] Rudd, D. F. A generalization of the residence time concept. *Can. J. Chem. Eng.*, pages 197–202, 1962.

[144] Russell, R. D. and J. Christiansen. Adaptive mesh selection strategies for solving boundary value problems. *SIAM J. Numer. Anal.*, 15(1):59–80, February 1978.

[145] Sargent, R. W. H. and G. R. Sullivan. The development of an efficient optimal control package. In Stoer, J., editor, *Lecture Notes in Control and Information Sciences 7*, pages 158–168, Berlin, 1978. 8th IFIP Conference on Optimization Techniques, Springer-Verlag.

[146] Schulz, V. J., K. H. Baumann, and S. Weiss. Kristallwachstum und Keimbildung bei der Kristallisation von Harnstoff und Kaliumsulfat. *Wissenschafliche Zeitschrift TH Leuna-Merseburg*, 24:500–515, 1982.

[147] Seinfeld, J. H. Identification of parameters in partial differential equations. *Chem. Eng. Sci.*, 24:65–74, 1969.

[148] Shaw, G. E. Inversion of optical scattering and spectral extinction measurements to recover aerosol size spectra. *Applied Opt.*, 18(7):988–993, April 1979.

[149] Sherwin, M. B., R. Shinnar, and S. Katz. Dynamic behavior of the well-mixed isothermal crystallizer. *AIChE J.*, 13:1141–1153, 1967.

[150] Sikdar, S. K. and A. D. Randolph. Secondary nucleation of two fast growth systems in a mixed suspension crystallizer: Magnesium sulfate and citric acid water systems. *AIChE J.*, 22(1):110–117, 1976.

[151] Sink, C. W. Eastman Chemicals Division, Tennessee Eastman Co.; Personal Communication, 1987.

[152] Strickland-Constable, R. F. The breeding of crystal nuclei—a review of the subject. *AIChE Symp. Ser.*, 68(121):1–7, 1972.

[153] Swithenbank, J., J. M. Beer, D. S. Taylor, D. Abbot, and G. C. McCreath. A laser diagnostic technique for the measurement of droplet and particle size distribution. In Zinn, B. T., editor, *Experimental Diagnostics in Gas Phase Combustion Systems*, pages 421–447. Progress in Astronautics and Aeronautics, AIAA, 1976.

[154] Tanaka, H., T. Hayashi, and T. Nishi. Application of digital image analysis to pattern formation in polymer systems. *J. Appl. Phys.*, 59(11):3627–3643, 1986.

[155] Tavare, N. S. Growth kinetics of ammonium sulfate in a batch cooling crystallizer using initial derivatives. *AIChE J.*, 31(10):1733–1735, October 1985.

[156] Tavare, N. S. Crystallization kinetics from transients of an MSMPR crystallizer. *Can. J. Chem. Eng.*, 64:752–758, 1986.

[157] Tavare, N. S. Batch crystallizers: A review. *Chem. Eng. Commun.*, 61:259–318, 1987.

[158] Timm, D. C. and M. A. Larson. Effect of nucleation kinetics on the dynamic behavior of a continuous crystallizer. *AIChE J.*, 14:452–457, 1968.

[159] Tsuchiya, H. M., A. G. Fredrickson, and R. Aris. Dynamics of microbial cell populations. *Adv. Chem. Eng.*, 6:125–206, 1966.

[160] Twomey, S. On the numerical solution of Fredholm integral equations of the first kind by the inversion of the linear system produced by quadrature. *J. Assoc. Comp. Mach.*, 10:97–101, 1963.

[161] Ulrich, J. and M. Stepanski. Use of the laser diffraction technique for particle size measurement at high suspension densities. *Part. Part. Syst. Charact.*, 7:25–29, 1990.

[162] Ulrich, M. Optimization of batch solution crystallization. *Ger. Chem. Eng.*, 4:195–200, 1979.

[163] van de Hulst, H. *Light Scattering by Small Particles.* Dover Publications, New York, 1981.

[164] Villadsen, J. and M. L. Michelsen. *Solution of Differential Equation Models by Polynomial Approximation.* Prentice-Hall, Englewood Cliffs New Jersey, 1978.

[165] Virtanen, J. Microcomputer control of sugar crystallization. *Sugar J.*, pages 8–9, 1986.

[166] Wakao, H., H. Hiraguchi, and T. Ishii. A simulation of crystallization from aqueous supersaturated solutions in a batch isothermal stirred tank. *Chem. Eng. J.*, 35(7):169–178, 1987.

[167] Walton, A. G. Nucleation in liquids and solutions. In Zettlemoyer, A. C., editor, *Nucleation*, New York, 1969. Marcel Dekker.

[168] Washburn, E. W., editor. *International Critical Tables of Numerical Data, Physics, Chemistry, and Technology*, volume 5. National Research Council, 1929.

[169] White, E. T. and P. G. Wright. Magnitude of size dispersion effects in crystallization. *Chem. Eng. Progr. Symp. Ser.*, 67(110):81–87, 1971.

[170] Wing, G. M. Integral equations of the first kind. Technical Report LA-UR-84-1234, Los Alamos National Laboratory, April 1984.

[171] Winter, B. Modell zur diskontinuierlichen Massenkristallisation und dessen Anwendung bei der Masstabsübertragung. *Chem. Techn.*, 36(9):375–378, 1984.

[172] Wiscombe, W. J. Improved Mie scattering algorithms. *Applied Opt.*, 19(9):1505–1509, May 1980.

[173] Witkowski, W. R. *Model Identification and Parameter Estimation of Crystallization Processes.* PhD thesis, The University of Texas at Austin, 1990.

[174] Witkowski, W. R., S. M. Miller, and J. B. Rawlings. Light scattering measurements to estimate kinetic parameters of crystallization. In Myerson, A. S. and K. Toyokura, editors, *Crystallization as a Separations Process*, pages 102–114, Washington, DC, 1990. American Chemical Society.

[175] Zumstein, R. C. and R. W. Rousseau. Growth rate dispersion by inital growth rate distributions and growth rate fluctuations. *AIChE J.*, 33(1):121–129, 1987.

[176] Zumstein, R. C. and R. W. Rousseau. Utilization of industrial data in the development of a model for crystallizer simulation. *AIChE Symp. Ser.*, 83(253):130–139, 1987.

Vita

Stephen Michael Miller, the son of Michael Jones and Carole Ann Miller, was born in Bristol, Tennessee on October 15, 1965. Farming was his primary occupation during childhood and adolescence; it was a period that assuaged fear of hard work and was a fertile time for collecting stories. He graduated from Sullivan East High School, Bluff City, Tennessee in 1983 and entered The University of Tennessee at Knoxville in September of that year. During the summers of 1985 and 1986 he worked at Eastman Chemical Company in Kingsport, Tennessee. He received the degree of Bachelor of Science in Chemical Engineering in June 1987 from The University of Tennessee. He began his graduate studies in the Chemical Engineering Department at The University of Texas at Austin in August of 1987 and received a Masters of Science degree in Chemical Engineering in May of 1991.

Permanent address: 1074 Silver Grove Rd.
Bluff City, TN 37618

This dissertation was typeset by the author using the LaTeX document preparation system.